THE UNIVERSITY *of* EDINBURGH

From Inauguration to Upgrade: Studying Charmless Beauty at LHCb

Mary Richardson-Slipper

Doctor of Philosophy
The University of Edinburgh
February 2025

Abstract

The LHCb experiment at CERN is designed for the study of b-hadrons as a laboratory to test the Standard Model of particle physics. Studies of charmless B-decays are an avenue for such studies. The $B^0 \to \phi\phi$ decay is a highly suppressed process that is allowed by the Standard Model that is not yet observed at LHCb using data collected in the period 2011 - 2016 inclusive. The rare nature of this mode makes it sensitive to beyond Standard Model physics which can manifest itself in the form of an enhanced branching fraction. This thesis presents a dedicated search for this decay mode in the full LHCb dataset, collected in the period 2011 - 2018 inclusive. No significant signal is observed and a new limit is set on the branching fraction at 1.3×10^{-8} at 90% confidence level.

The topologically identical and much more abundant decays of $B_s^0 \to \phi\phi$ are also studied as a probe of beyond Standard Model physics in CP violation. The $B_s^0 \to \phi\phi$ mode occurs via loop-level penguin processes and give access to the CP-violating phase, $\phi_s^{s\bar{s}s}$. The $B_s^0 \to \phi\phi$ decays in particular are sensitive to any beyond Standard Model physics that may manifest in the loop contributions. This thesis presents the expected sensitivity to $\phi_s^{s\bar{s}s}$ with $B_s^0 \to \phi\phi$ decays that may be achieved in the Upgrade I phase of LHCb, assuming 25 fb^{-1} of data are collected in Run 3.

Looking beyond Upgrade I and into the future, the LHCb experiment will begin Upgrade II; research and development is ongoing with a target to begin installation in 2033. Studies of the acceptance of the LHCb detector are presented; this informs the development of the Upgrade II subdetectors by setting a common working point. The effect of reducing acceptance is presented for three modes of complimentary topology. In addition, momentum parameterisation in fast simulation is used to give preliminary sensitivities to flagship measurements like the search for $B^0 \to \phi\phi$ in the Upgrade II era of the experiment.

Lay summary

One of the most precisely tested scientific theories is the Standard Model of particle physics. The Standard Model seeks to describe the behaviour of all the particles that exist in the Universe and how they interact with one another. Whilst the Standard Model is capable of making extremely precise predictions of observable physical processes, it has some shortcomings. One of the main shortcomings is the inability of the Standard Model to explain the fact that the Universe is dominated by matter rather than antimatter. The Universe is made almost entirely of matter, with no antimatter to be seen. The Standard Model is currently incapable of describing the mechanism by which this difference appears.

The Large Hadron Collider at CERN, 27 km in circumference, is a machine designed to collide protons at incredibly high energies. These collisions provide the perfect environment to test the most fundamental properties of particles. The LHCb experiment is one of four detectors situated on the ring of the Large Hadron Collider. LHCb records the properties of the particles that are produced in these collisions and it is specifically designed to study particles containing *beauty* quarks, also known as b-quarks.

This thesis presents a study of a particular subset of b-quark decays known as *charmless b-decays*. These processes have the potential to highlight discrepancies between the Standard Model and reality. Precisely studying these modes brings us closer to understanding the Universe more completely by setting constraints on possible new models.

Declaration

I declare that this thesis was composed by myself, that the work contained herein is my own except where explicitly stated otherwise in the text, and that this work has not been submitted for any other degree or professional qualification except as specified.

(*Mary Richardson-Slipper, February 2025*)

In loving memory of my Father,
Desmond Ronald Slipper
(1965 - 2002)

Acknowledgements

This thesis is the culmination of very many years of hard work and determination, but it would not exist but for the support of very many wonderful people. This document may only have my name on the cover, but I could never have achieved this alone.

Firstly, I must thank my supervisor, Prof. Matthew Needham. Matt, I am very fortunate indeed to have been working with you for the last few years. You have been patient and steadfast and have found time for me whenever I have needed it. I have learnt an incredible amount from you and could not have asked for a more knowledgeable supervisor to shadow. Secondly, thanks to Dr. Ozlem Ozcelik. I am so grateful of the help you have provided me all these years, and for your commitment to our projects and the Charmless working group.

Matthew Needham and Ozlem Ozcelik provided specific contributions to the search for $B^0 \to \phi\phi$. Thank you to Matt for providing the D_s tagger used to train the MVA for combinatorial background and for modelling and estimating the yields of the Λ_b^0, Ξ_b and partially constructed backgrounds. Thank you to Ozlem for providing the kinematic and PID reweighting and for training the XGBoost classifier for the combinatorial background MVA. Many thanks also to Ozlem for also developing the trigger line for the study of $B_s^0 \to \phi\phi$ in Run 3. Thank you to Prof. Pete Clarke and Dr. Rob Currie for their support using the RapidFit framework to perform the Run 3 sensitivity studies.

Matthew Needham and Renato Quagliani provided specific contributions to the studies of LHCb Upgrade II acceptance. Thank you to Matt for providing the single-kick model of the LHCb magnet. Thank you to Renato for providing the model to produce the RapidSim smearing models for various Upgrade II conditions.

The Edinburgh LHCb group has been a lovely community of people to work with. They welcomed me with open arms, and I have enjoyed every moment of my time here. To Prof. Franz Muheim, thank you for your support and encouragement, and for leading the group with such kindness. To Dr. Mark Williams, thank you for supporting me with the application for the Bell Burnell Graduate Scholarship which, without your guidance, I may never have applied for. To Dr. William Barter, thank you for your unwavering kindness in the most trivial of matters.

Thank you to Dr. Silvia Gambetta, for your support while I was based at CERN (and especially during my first conference). To Gary and Ryun, thank you for always lending a hand and teaching me the unspoken tips and tricks I needed to navigate this world. The broader PPE group at Edinburgh has also been a delightful group to be a part of. I must thank Prof. Sinead Farrington and Prof. Christos Leonidopoulos for the thought-provoking discussions in my annual assessments. To Prof. Andrzej Szelc, thank you for pointing out my misspelling of 'Cherenkov' in a graphic I had used in posters and talks for 6 months. To Dr. Cheryl Patrick, thank you for always lending a sympathetic ear and listening to my ramblings. To Dr. Ben Wynne, thank you for providing the figure of the LHC coordinate system. From the wider LHCb community, I extend my thanks to Dr. Yasmine Amhis and Dr. Nicole Skidmore for their support and encouragement.

To my dear friends Luke, Adam, Jenny and Amy, thank you all for your friendship. Thanks in particular to Jen and Amy for forgiving me for moving further north and allowing me to infiltrate your home whenever I might be in London. My move to Edinburgh brought new friends in Elise and Holly. Elise, thank you for our weekly wine-fuelled bake-off craft night extravaganzas. Holly, thank you for keeping our office so vibrant with your light and inspiring me with your creative mind. While on attachment at CERN I made life-long friends in Richard, Jon and Elliot. Thank you for making it such an adventure. Especially to dear Richard, who deserves a medal for the number of times I wandered into his office with yet another curiosity that I knew he would happily discuss with me.

I also thank Prof. Dame Jocelyn Bell Burnell, not only for being such an inspirational figure for women like me, but also for generously setting up the IOP Bell Burnell Graduate Scholarship fund which funded this PhD. To be an ambassador of the Bell Burnell scheme has been an honour and a privilege.

Finally, thank you to my family and Fred. To Oliver, who understands my brain better than anyone else. To Dave, for being such a strong and supportive parent. To Fred, for providing such security, joy and comic relief on this journey we have embarked upon together. Finally, to my simply wonderful mother Jacqueline. While you may not have directly contributed to what is in this document, it is your perseverance, collected nature, unparalleled work ethic and unwavering strength that has taught me what I needed to get here. I would not have done any of this without you.

Contents

List of Figures

List of Tables

Glossary

ALICE A Large Ion Collider Experiment. 25

ATLAS A Toroidal LHC Apparatus. 25

BDTG Gradient-boosted Boosted Decision Tree. 64

BNL Brookhaven National Laboratory. 5

BSM Beyond the Standard Model. 6

CERN European Centre for Nuclear Research. 25

CKM Cabibbo-Kobayashi-Maskawa. 5

CMS Compact Muon Solenoid. 25

DIRA Direction angle. 103

DOCA Distance of closest approach. 43

ECAL Electronagnetic calorimeter. 38

FCNC Flavour changing neutral current. 8

FTDR Framework Technical Design Report. 115

GIM Glashow-Iliopoulos-Maiani. 5

HL-LHC High luminosity Large Hadron Collider. 111

HLT High-level trigger. 41

HPDs Hybrid photon detectors. 37

IP Impact parameter. 31

IT Inner Tracker. 34

KS Kolmogorov-Smirnov. 77

L0 Level-0 trigger. 41

LHC Large Hadron Collider. 25

MaPMTs Multi-anode photomultiplier tubes. 38

MC Monte Carlo. 52

MLP Multilayer perceptron. 74

MSSM Minimal supersymetric Standard Model. 20

OT Outer Tracker. 34

PID Particle identification. 29

PQCD Perturbative Quantum Chromodynamics. 19

PS Preshower detector. 38

QCDF Quantum Chromodynamics factorisation. 19

RF Radio frequency. 25, 30

RICH Ring Imaging Cherenkov detector. 29

SLAC Stanford Linear Accelerator Center. 5

SM Standard Model. 3

SPD Scintillating Pad Detector. 38

ST Silicon Tracker. 34

TIS Triggered independently of signal. 71

TOS Triggered on signal. 70

TPA Triple product asymmetry. 16

TT Tracker Turicensis. 34

VELO Vertex Lcator. 27

WLS Wavelength-shifting. 38

Chapter 1

Introduction

During the Big Bang at the beginning of the Universe, it is believed that matter and antimatter were created in equal quantities [2]. It is now the case, confirmed by astronomical observations, that the Universe is matter dominated with no evidence of antimatter found [2]. One of the most important questions in physics is how is this asymmetry generated? Three conditions are necessary to generate a matter-antimatter asymmetry [3], they are the Sakharov conditions [4]: baryon number violation; the Universe moving away from thermal equilibrium; and violation of C and CP symmetries. Though the Standard Model of particle physics [5] fulfils all three conditions it is not able to generate observed asymmetry. It is this third condition that is the focus of the research presented in this thesis.

The LHCb experiment [6] is designed specifically for the study of b-hadrons. The nature of b-hadrons and their decays allow precise studies of CP violation in the Standard Model. The research presented in this thesis focusses on the study of purely hadronic charmless b-decays, so named due to the lack of c-quarks in the initial or final states. In particular, the study of $B_s^0 \to \phi\phi$ decays provides access to CP violation present in decays dominated by penguin contributions. The study of $B^0 \to \phi\phi$ decays is complimentary to the study of $B_s^0 \to \phi\phi$ as it is a pure penguin annihilation process that can provide further information about the sub-leading contributions to $B_s^0 \to \phi\phi$. Measurement of the branching fraction of this decay mode also provides a test of one of the rarest Standard Model processes. The presented studies can provide the information required to place bounds on models of new physics that may enhance these processes.

Chapter 2 describes the theoretical background that motivates the study of

$B_s^0 \to \phi\phi$ and $B^0 \to \phi\phi$. Chapter 3 describes the LHCb experiment in detail. Both the original detector, in operation from 2011 to 2018, and the upgraded detector, operational at the time of writing, are described. In addition to the detector hardware, the triggering system, simulation, track reconstruction procedure and flavour tagging procedure are also detailed.

The analysis to search for the $B^0 \to \phi\phi$ decay mode is described in Chapters 4, 5, 6, 7 and 8. The author of this thesis developed the multivariate analysis techniques to target background from kaon interactions and from D_s^+ meson decays. The author developed the models of the contributions to the invariant mass spectrum, performed the fit to the data and calculated the limit set by the analysis. This analysis is currently in collaboration review. The study of $B_s^0 \to \phi\phi$ with the Upgraded LHCb detector are described in Chapter 9. This chapter details the first study of this mode with Run 3 data and shows a study of the projected sensitivity to CP violation with this phase of LHCb. In the 2030s, LHCb will be upgraded again for the high-luminosity phase of the LHC. Chapter 10 describes studies of the expected performance of the detector in several scenarios. The presented work was used to inform the decisions made on the acceptance that LHCb Upgrade II is to cover and is included in the LHCb Upgrade II Scoping Document. The contributions of others to these analyses are acknowledged on page v.

Finally, Chapter 11 summarises the findings of these analyses, discusses the implications of these studies and outlines the future prospects for the studies of these modes.

Chapter 2

Theory

2.1 The Standard Model

The Standard Model (SM) of particle physics is a highly successful mathematical framework that describes matter and its interactions at a fundamental level [5]. It describes the twelve known fermions: the quarks — up, down, charm, strange, top and bottom; the leptons — the electron, muon, tau and the three neutrinos; and their antimatter counterparts. The particles of the SM are summarised in Figure 2.1. The SM has internal symmetry described by the $SU(2)_L \times U(1)_Y \times SU(3)$ symmetries. It describes three of the four fundamental forces; electromagnetic force, the weak force and the strong force. The SM does not include a quantum description of gravity.

The electromagnetic force, mediated by the massless photon (γ), couples to particles with electric charge. The weak force, responsible for nuclear decays, is mediated by the massive Z^0, W^+ and W^- bosons, first directly observed in 1983 at CERN [8, 9]. The weak force couples to all left-handed fermions and right-handed antifermions, where 'handedness' refers to the chirality of the particle. It is the only interaction that can change particle flavour.

In 1961, the electromagnetic and weak forces were unified into the electroweak force [10]. The electroweak force has $SU(2)_L \times U(1)_Y$ symmetries, where subscript L refers to the chiral nature of the weak interaction and the subscript Y refers to hypercharge as the associated charge of the $U(1)$ isospin symmetry. The $SU(2)_L$ symmetry introduces the $W^{(1)}$, $W^{(2)}$ and $W^{(3)}$ gauge fields, and the

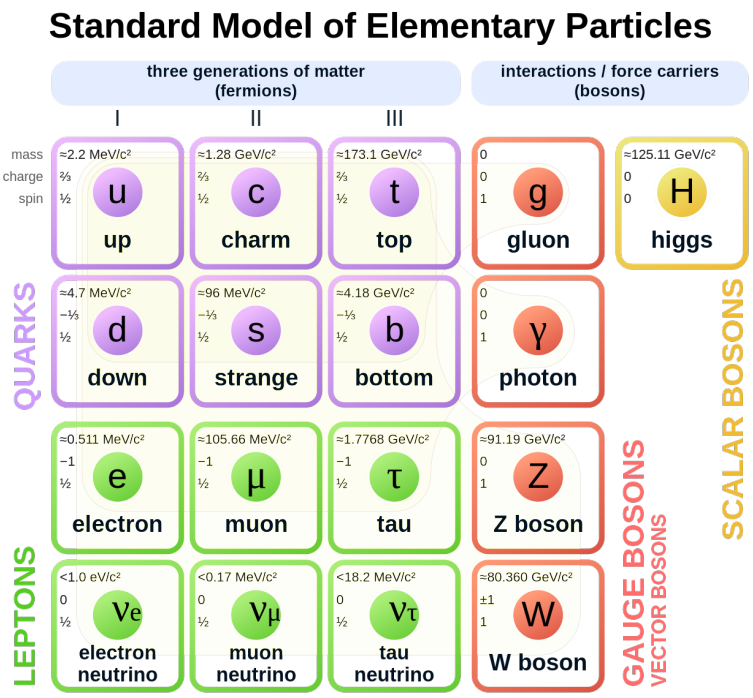

Figure 2.1 *The Standard Model of particle physics [7].*

$U(1)_Y$ symmetry introduces the gauge field denoted by B. When the Higgs mechanism [11] is added to the SM [12, 13], the non-zero vacuum expectation value of the Higgs potential breaks the $SU(2)_L \times U(1)_Y$ symmetry, and leaves only the $U(1)_{\text{em}}$ symmetry describing the electromagnetic interaction. This spontaneous symmetry breaking gives mass to the physical $W^{\pm}$ and Z^0 bosons. The four physical bosons, $W^{\pm}$, Z^0 and γ can be written as linear combinations of the fields of the $SU(2)_L \times U(1)$ symmetries,

$$W^+ = \frac{1}{\sqrt{2}}(W^{(1)} - iW^{(2)}) \tag{2.1}$$

$$W^- = \frac{1}{\sqrt{2}}(W^{(1)} + iW^{(2)}) \tag{2.2}$$

$$Z^0 = -B\sin\theta_{\text{W}} + W^{(3)}\cos\theta_{\text{W}} \tag{2.3}$$

$$\gamma = B\cos\theta_{\text{W}} + W^{(3)}\sin\theta_{\text{W}} \tag{2.4}$$

where the photon remains massless due to an unbroken $U(1)_{\text{em}}$ symmetry that remains after spontaneous symmetry breaking, and θ_{W} is the Weinberg or weak mixing angle [12].

The strong force is responsible for the binding of quarks into hadrons [14]. It has $SU(3)$ symmetry and is mediated by eight gluons and couples to the colour

charge of the quarks. The gluons themselves carry a colour charge and the various combinations of the red, green and blue charges yield the eight possible gluons. As the gluons themselves carry a colour charge, they can self-interact. This self-interaction produces a force that is so strong that individual quarks cannot be pulled apart, known as colour confinement. No particles carrying colour exist freely, and are found in overall colourless bound states, for example, $q\bar{q}$, qqq or $\bar{q}\bar{q}\bar{q}$. Another feature of the strong force is asymptotic freedom, where the strength of the coupling gets weaker at small length scales [15, 16].

The quark model, first introduced in 1964 by Gell-Mann and Zweig, originally introduces the up (u), down (d), and strange (s), quarks [17]. Measurements of deep-inelastic scattering at the Stanford Linear Accelerator Center (SLAC) demonstrated the composite nature of the proton and thus provided evidence of the quark model [18]. In 1970, the Glashow-Iliopoulos-Maiani (GIM) mechanism [19] was suggested as a means to explain the small rate of flavour-changing neutral currents by adding a fourth quark, the charm quark (c) as a partner to the strange quark. The quark model was extended in 1973 to contain three quark generations, with weak interaction described by the Cabibbo-Kobayashi-Maskawa (CKM) matrix [20]. This description was introduced as it was realised that the 3×3 unitary mixing matrix would allow for CP violation, which is not permitted in a four-quark model. The charm quark was discovered in 1974 by SLAC [21] and the Brookhaven National Laboratory (BNL) [22], followed by the bottom (or beauty) quark in 1977 at Fermilab [23] and the final quark, the top quark, was observed for the first time in 1995 by the CDF [24] and D0 [25] collaborations.

The Higgs boson was the final piece missing from the SM until its discovery in 2012 by the ATLAS and CMS experiments at CERN [26, 27]. The predictions from the SM have been tested to unprecedented precision at experiments around the world and it stands the test of time. However, the SM cannot be the end of the story here. There are several unexplained phenomena that exist beyond the SM. For example: the motivation for work in this thesis, the size of the matter-antimatter asymmetry of the Universe; and the nature of neutrinos, whether they are Dirac or Majorana fermions [28], or the origin of their masses. The absolute values of neutrino masses, at the time of writing, has still not been measured and a limit is currently set at < 0.45 eV/c^2 at 90% confidence level by the KATRIN experiment [29].

Flavour physics is the study of quark and lepton flavour in the SM, in particular

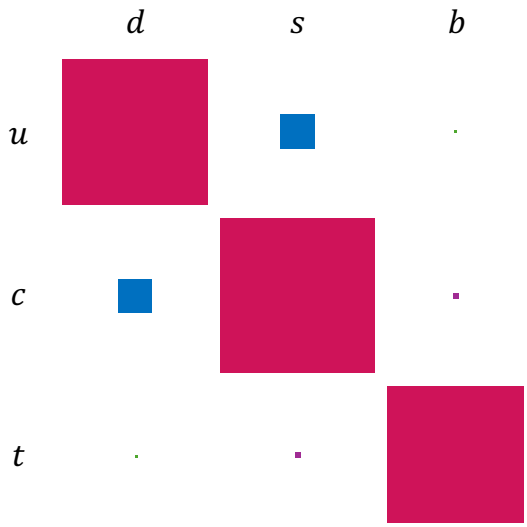

Figure 2.2 *The relative sizes of the CKM elements, where the area of the square represents the square of the CKM element. Adapted from [30].*

the way particle flavours change and mix. The flavour sector of the SM has two main puzzles; the Standard Model flavour puzzle and the new physics flavour puzzle [31]. The SM flavour puzzle is that the matrix which describes the mixing of quark flavours, the CKM matrix [20, 32], has an unexplained hierarchy which hints at a deeper structure in the SM, as shown in Figure 2.2. The new physics flavour puzzle refers to the idea that the SM is only an effective field theory valid at the current probed energies. If this is the case, it is expected we would see more deviation from SM predictions in suppressed processes involving flavour such as meson mixing. We have not seen any such deviations in the flavour observables such as meson mixing parameters which can probe new physics up to TeV-scale [33]. The continued study of flavour physics at current and future experiments hopes to provide some direction for development of the theory. By making high-precision measurements and putting the SM predictions to the test, beyond Standard Model physics (BSM) may be realised.

2.2 Mixing of neutral mesons

A detailed discussion of the following sections on meson mixing and CP violation can be found in [3] and [34]. In the SM, the mechanism for flavour mixing is

governed by the CKM matrix [20],

$$\begin{pmatrix} d' \\ s' \\ b' \end{pmatrix} = \begin{pmatrix} V_{ud} & V_{us} & V_{ub} \\ V_{cd} & V_{cs} & V_{cb} \\ V_{td} & V_{ts} & V_{tb} \end{pmatrix} \begin{pmatrix} d \\ s \\ b \end{pmatrix}, \tag{2.5}$$

where the primed states represent the weak eigenstates, the unprimed states represent mass eigenstates and V_{ij} are the CKM elements. Mesons are bosons consisting of a quark and antiquark ($q\bar{q}$). The physical meson states are the Hamiltonian eigenstates, $|M_1\rangle$ and $|M_2\rangle$, which propagate as superpositions of the flavour eigenstates, $|M^0\rangle$ and $|\overline{M^0}\rangle$,

$$|M_{1,2}\rangle = p_{1,2}|M^0\rangle \pm q_{1,2}|\overline{M^0}\rangle, \tag{2.6}$$

these satisfy an eigenvalue equation with the Hamiltonian operator, $\mathcal{H}$,

$$\mathcal{H}|M_{1,2}\rangle = \lambda_{1,2}|M_{1,2}\rangle, \tag{2.7}$$

with eigenvalues λ_1 and λ_2. Equation 2.6 can be rearranged to also find expressions for the flavour states in terms of the Hamiltonian states,

$$|M^0\rangle = \frac{1}{2p}\big(|M_1\rangle + |M_2\rangle\big), \tag{2.8}$$

$$|\overline{M^0}\rangle = \frac{1}{2q}\big(|M_1\rangle - |M_2\rangle\big), \tag{2.9}$$

where the CPT theorem [35] is used to fix $p_1 = p_2 = p$ and $q_1 = q_2 = q$ [34]. The flavour eigenstates are defined at production and decay, but the meson propagates as the Hamiltonian eigenstate with defined lifetime. The way the neutral meson state changes with time can be derived. Since $|M_1\rangle$ and $|M_2\rangle$ are eigenstates of the Hamiltonian,

$$i\hbar\frac{\mathrm{d}}{\mathrm{d}t}|M_{1,2}\rangle = \lambda_{1,2}|M_{1,2}\rangle \quad \text{with} \quad \lambda_{1,2} = m_{1,2} - \frac{i}{2}\Gamma_{1,2}, \tag{2.10}$$

where $m_{1,2}$ and $\Gamma_{1,2}$ are the masses and widths of the Hamiltonian eigenstates, then,

$$|M_{1,2}(t)\rangle = \exp\left(-i\lambda_{1,2}t\right)|M_{1,2}(0)\rangle \tag{2.11}$$

which can then be used to describe the time evolution of the flavour state. Considering $|M^0(t)\rangle$,

$$|M^0(t)\rangle = \frac{1}{2p}\big(|M_1(t)\rangle + |M_2(t)\rangle\big), \tag{2.12}$$

and the time evolution of $|M_1\rangle$ and $|M_2\rangle$, one can obtain the time evolution of this flavour state. Eq. 2.11 can be used to find,

$$|M^0(t)\rangle = \frac{1}{2p}\Big[\exp\left(-i\lambda_1 t\right)|M_1(0)\rangle + \exp\left(-i\lambda_2 t\right)|M_2(0)\rangle\Big]. \tag{2.13}$$

Eq. 2.6 can be used to rewrite $|M_1(0)\rangle$ and $|M_2(0)\rangle$. After manipulation, the following expression is obtained for the time evolution of $|M^0\rangle$,

$$|M^0(t)\rangle = \frac{1}{2}\Big[f_+(t)|M^0\rangle + \frac{q}{p}f_-|\overline{M^0}\rangle\Big], \tag{2.14}$$

where $f_\pm(t)$ represent the time-dependent probabilities of the meson evolving to stay in its current state or oscillate into the conjugate state. These are defined as follows,

$$f_\pm(t) = \exp\Big(-im_1 t - \Gamma_1\frac{t}{2}\Big) \pm \exp\Big(-im_2 t - \Gamma_2\frac{t}{2}\Big). \tag{2.15}$$

Following the same derivation, one can also arrive at the following,

$$|\overline{M^0}(t)\rangle = \Big[\frac{p}{q}f_-(t)|M^0\rangle + f_+(t)|\overline{M^0}\rangle\Big] \tag{2.16}$$

which gives the time evolution of a $|\overline{M^0}\rangle$ state. Mixing is an example of a flavour changing neutral current (FCNC) process, which means it is suppressed in the SM. Due to this, mixing processes are particularly susceptible to new physics contributions that involve massive new particles. Constraints from current experiments still allow new physics contributions in mixing at the level of 20% relative to the SM [36]. By measuring the parameters of the CKM matrix and performing global analyses, new physics may be constrained. The Feynman diagram of $B_s^0 - \overline{B_s^0}$ mixing is shown in Fig. 2.3.

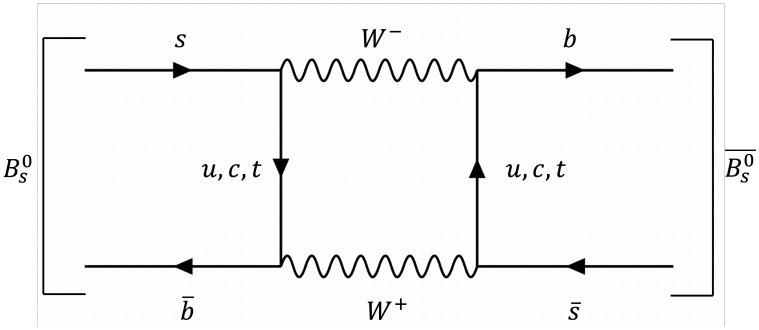

Figure 2.3 *Mixing box diagram showing* $B_s^0 \to \overline{B_s^0}$.

2.3 CP violation

CP violation is the violation of symmetry under the combined action of charge conjugation (C) and parity (P) transformations. Charge conjugation changes particles to anti-particles (and vice-versa). The parity transformation swaps the directions of polar vectors. These transformations are shown pictorially in Fig. 2.4. There is also the discrete transformation of time-reversal (T), which reverses the order in which events happen. The CPT theorem states that the combination of C, P and T transformations is a valid symmetry [3]. If CPT symmetry is broken then Lorentz invariance is also broken. There is no such requirement for CP symmetry breaking. Violation of CP symmetry is one of the necessary Sakharov conditions required for our Universe to have evolved to be what it is today [4].

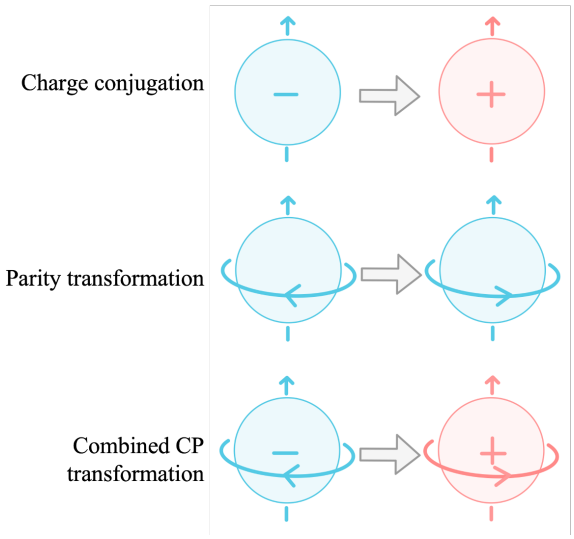

Figure 2.4 *The action of* C, P *and* CP *transformations on a particle.*

2.3.1 Types of CP Violation

In the SM, CP violation is allowed and manifests in the CKM matrix (Section 2.2). CP violation can arise when a process and the CP conjugate process have different decay amplitudes. This is known as direct CP violation [3]. CP violation also arises in neutral meson mixing, known as indirect CP violation, and in the interference of mixing and decay. Each of these types of CP violation is described in turn. The $B_s^0 \to \phi\phi$ decay is one which can exhibit CP violation in the interference between mixing and decay, as the final state of two ϕ mesons is accessible to both B_s^0 and $\overline{B_s^0}$.

CP violation in decay

For CP violation in decay, one must have a difference in the amplitudes of the process and its CP conjugate,

$$|A_f| \neq |\bar{A}_{\bar{f}}|, \tag{2.17}$$

where f represents the final state, and $\bar{f}$ is the CP conjugate of the final state. For this to occur, it is necessary for the process to have at least two contributing amplitudes and both the strong (CP-even) and weak (CP-odd) phases to differ between the contributing amplitudes. This can be seen by considering a state i decaying to a state f. If there is a single contributing amplitude, then

$$\langle f|T|i\rangle = Ae^{i(\delta+\phi)}, \tag{2.18}$$
$$\langle \bar{f}|T|\bar{i}\rangle = Ae^{i(\delta-\phi)}, \tag{2.19}$$

where T is the transition operator, δ is the strong phase and ϕ is the weak phase. It is clear that, in this case,

$$|\langle f|T|i\rangle| = |\langle \bar{f}|T|\bar{i}\rangle| = A \tag{2.20}$$

and therefore there is no CP violation. If there are two contributing amplitudes,

$$\langle f|T|i\rangle = A_1e^{i(\delta_1+\phi_1)} + A_2e^{i(\delta_2+\phi_2)}, \tag{2.21}$$
$$\langle \bar{f}|T|\bar{i}\rangle = A_1e^{i(\delta_1-\phi_1)} + A_2e^{i(\delta_2-\phi_2)}, \tag{2.22}$$

which can be used to show (see for example [34, Ch. 5.3]) that

$$|\langle f|T|i\rangle|^2 - |\langle \bar{f}|T|\bar{i}\rangle|^2 = -4A_1A_2\sin(\delta_1-\delta_2)\sin(\phi_1-\phi_2). \tag{2.23}$$

This shows that CP violation can occur here, but only if $\delta_1 \neq \delta_2$ and $\phi_1 \neq \phi_2$.

CP violation in mixing

CP violation in mixing can occur when the physical states are not eigenstates of CP. Eigenstates of CP satisfy the equation

$$CP|M_\pm\rangle = \pm|M_\pm\rangle. \tag{2.24}$$

The CP eigenstates can be constructed as combinations of the flavour eigenstates,

$$|M_\pm\rangle = \frac{1}{\sqrt{2}}\Big[|M^0\rangle \pm |\overline{M^0}\rangle\Big]. \tag{2.25}$$

Comparing these CP eigenstates to the Hamiltonian states in Eq. 2.6, it can be seen that these are the same if the condition,

$$\left|\frac{p}{q}\right| = 1, \tag{2.26}$$

is satisfied. If this condition is not satisfied, then the transition probabilities of $|M^0\rangle \to |\overline{M^0}\rangle$ and $|\overline{M^0}\rangle \to |M^0\rangle$ are not equal. This is shown using Eq. 2.14 and Eq. 2.16,

$$\langle \overline{M^0}|M^0(t)\rangle = \frac{q}{p}f_-(t), \tag{2.27}$$

$$\langle M^0|\overline{M^0}(t)\rangle = \frac{p}{q}f_-(t), \tag{2.28}$$

and therefore CP symmetry is violated in mixing if the condition is not met and these transition probabilities differ.

CP violation in the interference of mixing and decay

This type of CP violation can only occur if the final state, f, is accessible to both M^0 and $\overline{M^0}$. CP symmetry is violated if

$$\Gamma(\overline{M^0} \to (\to M^0) \to f) \neq \Gamma(M^0(\to \overline{M^0}) \to f). \tag{2.29}$$

CP violation in the interference of mixing and decay can still be present in the absence of CP violation in both decay and mixing, where $|p| = |q|$ and $|A_f| = |\bar{A}_{\bar{f}}|$. For this discussion the parameter, λ_f, is introduced,

$$\lambda_f \equiv \frac{q}{p}\frac{\bar{A}_f}{A_f}, \tag{2.30}$$

and CP symmetry requires

$$\lambda_f = \frac{1}{\lambda_{\bar{f}}} \tag{2.31}$$

where $\lambda_{\bar{f}}$ is defined as in Eq. 2.30 replacing $f \to \bar{f}$. If there is no CP violation in mixing or decay, then it follows that $|\lambda_f| = |\lambda_{\bar{f}}|^{-1}$. CP violation in this interference can still arise due to a relative weak phase between q/p and $\bar{A}_f/A_f$, where

$$\arg(\lambda_f) + \arg(\lambda_{\bar{f}}) \neq 0. \tag{2.32}$$

This is further simplified if the final state, f, is a CP eigenstate ($f = \bar{f}$), and the condition for CP violation becomes

$$2\arg(\lambda_f) \neq 0. \tag{2.33}$$

2.4 Charmless B decays

A particularly attractive area of flavour physics for probing the SM is the study of b-hadron[1] decays to a charmless final state. They are purely hadronic modes occurring via $b \to s$ transitions. Alongside measurements of CP violation, the angular analyses of key charmless modes highlight an interesting question known as the polarisation puzzle, which is described in Section 2.4.1. Study of CP violation in the mode $B_s^0 \to \phi\phi$ is introduced in Sections 2.4.2 and 2.4.3. The

[1]Hadrons containing b- or $\bar{b}$-quarks.

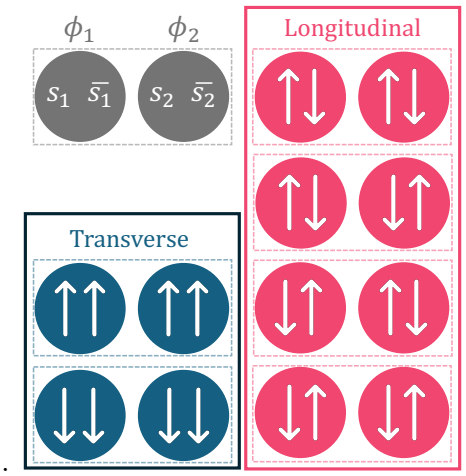

Figure 2.5 *Possible combinations of helicities forming allowed VV polarisaritons in $B_s^0 \to \phi\phi$ decays. The pair of ϕ mesons is represented by two circles, with the helicities of the quarks represented by pointed arrows.*

search for rare charmless modes such as $B^0 \to \phi\phi$, described in Section 2.6, may provide an avenue to understand the polarisation puzzle.

2.4.1 The polarisation puzzle

The nature of the weak interaction means that it only couples to left-handed fermions and right-handed anitfermions. Hence, outgoing quarks from weak interactions mostly have negative helicity, and outgoing antiquarks have positive helicities. A quark coming from a weak vertex in B-decays can undergo a helicity flip, which is suppressed by a factor of $\approx m_q/m_b$. Of the possible combinations for the VV polarisation, it is only the longitudinal polarisation that can occur without a helicity flip occurring. This means the longitudinal polarisation should dominate.

For modes occurring at tree level, for example $B^0 \to \rho^+\rho^-$, it is observed to be the case that the longitudinal polarisation dominates [37]. For modes that are expected to have a sizeable penguin contribution, for example $B^0 \to \phi K^*(892)$, a large transverse polarisation is observed which suggests further understanding of penguin modes is needed [38]. This is the polarisation puzzle [39].

In $B_s^0 \to \phi\phi$ decays, the first polarisation measurement was by the CDF collaboration in 2011, who measured the fraction of longitudinal contributions to be $0.348 \pm 0.041 \pm 0.021$ [40]. Using data from 2011, LHCb published a measurement of the

polarisation amplitudes and found $|A_0|^2 = 0.365 \pm 0.022\,(\text{stat}) \pm 0.012\,(\text{syst})$ [41]. In the latest measurement from LHCb, this fraction is measured to be $0.384 \pm 0.007\,(\text{stat}) \pm 0.003\,(\text{syst})$ [42]

The larger contributions from the transverse polarisation can be explained in several ways, namely pure penguin annihilation contributions [43], rescattering processes [44] or BSM physics [45].

2.4.2 CP violation in $B_s^0 \to \phi\phi$

The $B_s^0 \to \phi\phi$ decay is an example of a decay which can exhibit CP violation in interference with a final state, $\phi\phi$, which is a CP eigenstate. The decay amplitudes introduce a weak phase, ϕ_f, and the mixing introduces a weak phase, ϕ_M. The size of the CP violation in $B_s^0 - \overline{B_s^0}$ mixing is expected to be small in the SM [3, p. 407] and so it can be written

$$\left|\frac{q}{p}\right| \approx 1 \implies \frac{q}{p} = e^{-i\phi_M}. \tag{2.34}$$

The amplitudes A_f and $\bar{A}_f$ introduce phases also. Using the λ_f parameter introduced in Sec. 2.3.1, the strong phase δ_f cancels but the weak phase ϕ_f survives. This leads to an observable CP-violating phase,

$$\phi_s^{s\bar{s}s} = \arg(\lambda_f) = \phi_M - 2\phi_f, \tag{2.35}$$

$$= \phi_M - \phi_D, \tag{2.36}$$

where ϕ_D is the weak phase contribution from the decay amplitudes. For $B_s^0 \to \phi\phi$, $\phi_s^{s\bar{s}s}$ is expected to be ≈ 0 in the SM. This can be seen by considering the CKM elements that contribute to the Feynman diagrams of the mixing and decay processes, assuming loop contributions are dominated by top-quark loops. These are both shown in Fig. 2.6. By considering the CKM elements contributing to the mixing amplitude, it can be seen that the mixing phase is given by the following,

$$\phi_M = 2\arg(V_{ts}V_{tb}^*), \tag{2.37}$$

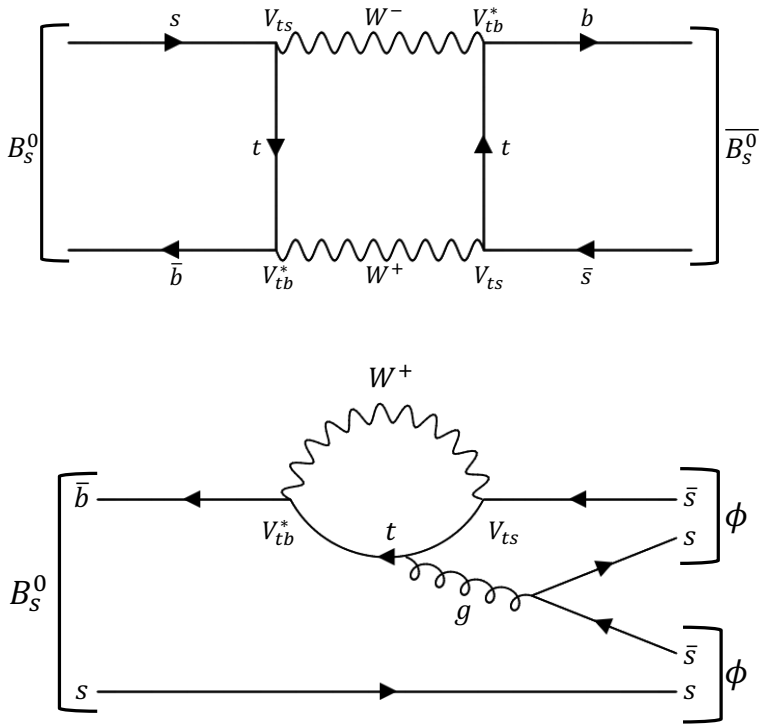

Figure 2.6 *CKM elements corresponding to the interaction vertices in $B_s^0 - \overline{B_s^0}$ mixing (top) and the $B_s^0 \to \phi\phi$ decay (bottom).*

and from the decay diagram it can be seen that the amplitude is proportional to $V_{ts}V_{tb}^*$. From the decay amplitude the overall decay phase, ϕ_D, is found as follows,

$$\phi_D = \arg\left(\frac{V_{ts}V_{tb}^*}{V_{tb}V_{ts}^*}\right), \tag{2.38}$$

$$= 2\arg(V_{ts}V_{tb}^*), \tag{2.39}$$

and thus $\phi_s^{s\bar{s}s} = \phi_M - \phi_D \approx 0$. If $\phi_s^{s\bar{s}s}$ deviates significantly from zero, this would indicate new physics is at play in the $B_s^0 \to \phi\phi$ decay.

2.4.3 Experimental determination of the CP violating weak phase

The $B_s^0 \to \phi\phi$ decay is a $P \to VV$ decay. The B_s^0 meson is a pseudoscalar: a meson with a total spin of 0 and odd parity. The ϕ meson is a vector meson: a meson with total spin of 1 and odd parity. The ϕ mesons can satisfy angular momentum conservation in three helicity states; parallel, transverse and longitudinal, with corresponding helicity amplitudes $A_\parallel$, $A_\perp$ and A_0. The

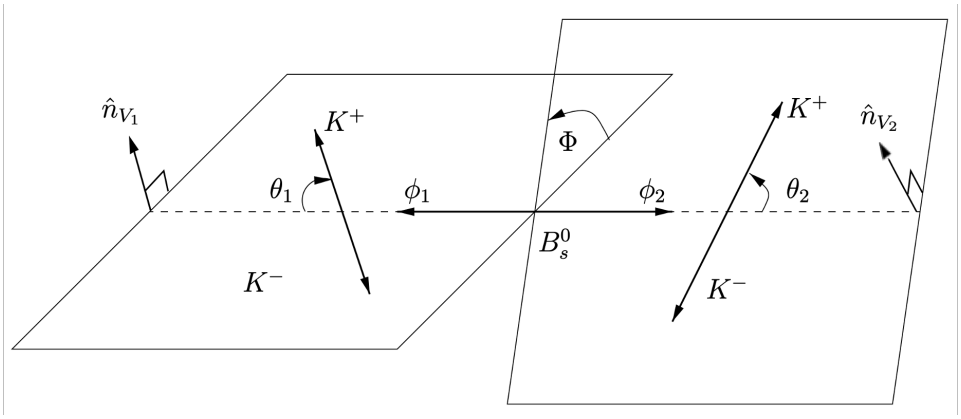

Figure 2.7 *Angular variables in the $B_s^0 \to \phi\phi$ decay in the rest frame of the B_s^0 meson [1].*

amplitudes $A_\parallel$ and $A_\perp$ linear combinations of the amplitudes of defined helicity,

$$A_\parallel \equiv \frac{1}{\sqrt{2}}(A_+ + A_-), \tag{2.40}$$

$$A_\perp \equiv \frac{1}{\sqrt{2}}(A_+ - A_-), \tag{2.41}$$

where A_+ and A_- are the amplitudes corresponding to final states with overall helicities of $+1$ and -1 respectively. The amplitudes A_0 and $A_\parallel$ are even under CP while amplitude $A_\perp$ is odd under CP, and hence this decay mode contains an admixture of CP states. Thus the fraction of each of these helicity states that contribute to the final state is required to determine $\phi_s^{s\bar{s}s}$. Each of these helicity states has a different angular distribution. The angular variables are defined according to Fig. 2.7. The angles $\theta_{1,2}$ are the angles between the K^+ meson momentum in the rest frame of $\phi_{1,2}$ and the $\phi_{1,2}$ momentum in the rest frame of the B_s^0. The angle Φ here is the angle between the two ϕ decay planes [1]. The choice of which ϕ meson is labelled with 1 or 2 is random. The CP-violating phase, $\phi_s^{s\bar{s}s}$, is extracted from a time dependent angular analysis to disentangle the helicity amplitudes.

The CP-violating phase $\phi_s^{s\bar{s}s}$ was first measured by the LHCb collaboration using 1 fb^{-1} of data collected in 2011. This analysis restricted the value of $\phi_s^{s\bar{s}s}$ to the range $[-2.46, -0.76]$ rad [46]. With the full Run 1 sample of 3 fb^{-1}, $\phi_s^{s\bar{s}s}$ was measured to be $-0.17 \pm 0.15\,(\text{stat}) \pm 0.03\,(\text{syst})$ rad [47]. In 2020, LHCb published an enhanced measurement including further data from 2015 and 2016. Now with a total 5 fb^{-1} of data, the measurement of $\phi_s^{s\bar{s}s}$ was $\phi_s = -0.073 \pm 0.115\,(\text{stat}) \pm 0.027\,(\text{syst})$ rad [1]. In 2023, the LHCb experiment

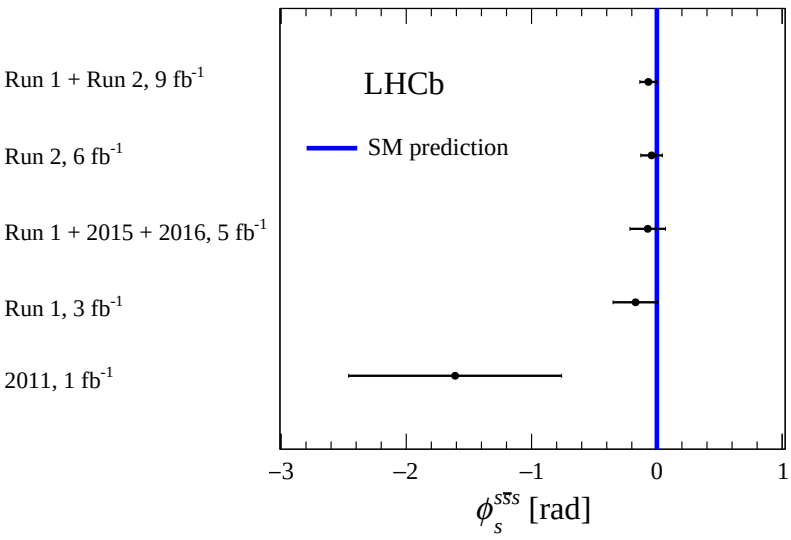

Figure 2.8 *The current experimental status of the value of $\phi_s^{s\bar{s}s}$ measured in $B_s^0 \to \phi\phi$ decays. Source: LHCb Collaboration [42].*

published the result from 2017 and 2018 data, corresponding to 6 fb^{-1} and the combination of Run 1 + Run 2 [42] which gives $\phi_s = -0.074 \pm 0.069$ rad, which is consistent with zero. These measurements are summarised in Figure 2.8.

2.5 Triple product asymmetries

Another probe of CP violation in $B_s^0 \to \phi\phi$ decays is the study of Triple Product Asymmetries (TPAs) [48]. TPAs are constructed as the scalar triple product of the momenta and polarisations of particles in the final state and are odd under time reversal.

In decays to a four-particle final state, there are three independent momenta from which a triple product can be formed. A T-odd quantity can be formed,

$$A = \overrightarrow{p_1} \times \overrightarrow{p_2} \cdot \overrightarrow{p_3}, \tag{2.42}$$

where the subscripts refer to different final state particles. An asymmetry in the distribution of a T-odd triple product suggests CP violation beyond the Standard Model. In the case of $B_s^0 \to \phi\phi$, referring back to the helicity angles defined in 2.4.2, one can construct combinations of the decay plane unit vectors,

$n_{\hat{V}_{1,2}}$ and the line defined as the intersection of the two planes, $\hat{z}$,

$$n_{\hat{V}_1} \cdot n_{\hat{V}_2} = \cos\Phi, \tag{2.43}$$

$$n_{\hat{V}_1} \times n_{\hat{V}_2} = \sin\Phi\hat{z}, \tag{2.44}$$

which can then be combined to find scalar triple products,

$$(n_{\hat{V}_1} \times n_{\hat{V}_2}) \cdot \hat{z} = \sin\Phi, \tag{2.45}$$

$$(n_{\hat{V}_1} \times n_{\hat{V}_2}) \cdot (n_{\hat{V}_1} \cdot n_{\hat{V}_2}) = \cos\Phi\sin\Phi. \tag{2.46}$$

These define the triple product variables [49]

$$U \equiv \sin\Phi\cos\Phi, \tag{2.47}$$

$$V \equiv \sin\pm\Phi \text{ with positive taken if } \cos\theta_1\cos\theta_2 \geq 0, \tag{2.48}$$

which can then be used to define the TPAs,

$$A_U = \frac{\Gamma(U>0) - \Gamma(U<0)}{\Gamma(U>0) + \Gamma(U<0)} \text{ and } A_V = \frac{\Gamma(V>0) - \Gamma(V<0)}{\Gamma(V>0) + \Gamma(V<0)}. \tag{2.49}$$

A non-zero TPA is a clear signature of new physics beyond the SM. By measuring these asymmetries, CP violation can be probed in a time-independent analysis without the need to know the flavour of the B_s^0 meson.

TPAs were first measured in $B_s^0 \to \phi\phi$ by the CDF collaboration at Fermilab [40]. They were later measured by the LHCb experiment using data collected in 2011 [41], corresponding to 1 fb^{-1} and then again with data collected in 2011, 2012, 2015 and 2016 corresponding to 5 fb^{-1} [1]. The results of each of these studies is summarised in Table 2.1. The measurements of TPAs in $B_s^0 \to \phi\phi$ show no sign of CP violation. The results are still statistically limited, and further measurements with more precision may highlight any small effects.

Source	A_U	A_V
CDF [40]	$-0.007 \pm 0.064 \pm 0.018$	$-0.120 \pm 0.064 \pm 0.016$
LHCb 2011 [41]	$-0.055 \pm 0.036 \pm 0.018$	$0.010 \pm 0.036 \pm 0.018$
LHCb 2011-2016 [1]	$-0.003 \pm 0.011 \pm 0.004$	$-0.014 \pm 0.011 \pm 0.004$

Table 2.1 *Summary of measurements of TPAs A_U and A_V in $B_s^0 \to \phi\phi$ decays. The first uncertainties are statistical, and the second systematic.*

2.6 The $B^0 \to \phi\phi$ decay

The $B^0 \to \phi\phi$ decay is an example of a $\bar{b}d \to s\bar{s}$ penguin annihilation. It is highly suppressed in the SM by multiple quantum loops, Cabibbo suppression [32] and the OZI rule[50, 51]. The latter of these states that if the Feynman diagram of a process may be separated into two disconnected diagrams by cutting the gluon lines then this process is suppressed. For these reasons, the $B^0 \to \phi\phi$ decay is predicted to have a very small branching fraction. A summary of theoretical predictions for the $B^0 \to \phi\phi$ branching fraction is given in Table 2.2. The table also shows the calculation used to arrive at the prediction, either perturbative QCD (PQCD) or QCD factorisation (QCDF). An example Feynman diagram for this process is shown in Figure 2.9.

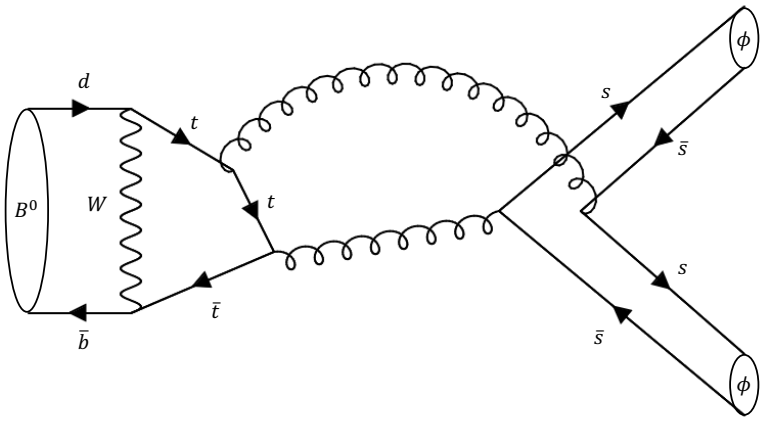

Figure 2.9 *An example Feynman diagram for the penguin annihilation process that describes the decay $B^0 \to \phi\phi$.*

These predictions vary by more than an order of magnitude and have large

BF ($\times 10^{-8}$)	Scheme	Reference
1.2 ± 0.6	PQCD	[52]
2.9 ± 0.6	PQCD	[53]
1.6 ± 0.4	PQCD	[54]
1.2 ± 0.3	QCDF	[55]
$4.4^{+0.9}_{-0.8}$	PQCD	[56]
1.9 ± 0.3	PQCD	[57]
< 3	QCDF	[45]
$0.21^{+0.16}_{-0.3}$	QCDF	[58]

Table 2.2 *Theory predictions for the $B^0 \to \phi\phi$ branching fraction, and the calculation used.*

associated uncertainties. In models of $\omega - \phi$ mixing and rescattering processes the branching fraction of $B^0 \to \phi\phi$ decays may be enhanced [58, 59].

In the decay of B_s^0 mesons, decays to ω mesons are OZI suppressed, while decays to ϕ mesons are OZI allowed [60]. For decays of B^0 mesons, the opposite is true. The ω and ϕ mesons can be written as [61]

$$\phi(1020) = \psi_8 \cos\theta_V - \psi_1 \sin\theta_V \tag{2.50}$$

$$\omega(782) = \psi_8 \sin\theta_V + \psi_1 \cos\theta_V, \tag{2.51}$$

where θ_V is the vector mixing angle and $\psi_1, 8$ are $SU(3)$ wavefunctions. Since

$$\psi_1 = \frac{1}{\sqrt{3}}(u\bar{u} + d\bar{d} + s\bar{s}), \tag{2.52}$$

$$\psi_8 = \frac{1}{\sqrt{6}}(u\bar{u} + d\bar{d} - 2s\bar{s}), \tag{2.53}$$

and the value of θ_V is found to be 34.6° [61], the ϕ meson is almost purely composed of $s\bar{s}$. If the ω and ϕ meson can mix, it is possible that the ω mesons from an OZI-allowed B^0 decay could undergo mixing to give ϕ mesons in the final state.

Models of rescattering can enhance the branching fraction of rare B-decays [59]. Rescattering is a process by which the intermediate states of a favoured decay can scatter from one another to give a different final state. It is then possible that rescattering models could allow a B^0 meson to decay to some intermediate state where rescattering then produces the two ϕ mesons.

A particularly popular BSM theory is supersymmetry, which is introduced as a means to explain the apparent small Higgs mass, which could have very large contributions from loop corrections with heavy particles. In introducing a symmetry between bosons and fermions, these higher order corrections to the Higgs mass cancel. In the minimal supersymmetric SM (MSSM) each of the SM particles has a supersymmetric partner. For example, the partners to the quarks are the so-called *squarks* which are bosons, not fermions. When deriving models of supersymmetry, it is useful to introduce an object called a superpotential, W, which is a function of the scalar fields as complex variables,

$$W = \frac{1}{2}M^{ij}\phi_i\phi_j + \frac{1}{6}y^{ijk}\phi_i\phi_j\phi_k, \tag{2.54}$$

where M^{ij} is the mass matrix of the fermion fields, $\phi_{i,j,k}$ are scalar fields and y^{ijk} represents the Yukawa coupling of a scalar ϕ_k to two fermions ψ_i and ψ_j [62]. For a MSSM, some of the terms in the superpotential lead to baryon and lepton number violating processes which have never been observed experimentally. These terms are

$$W_{\Delta L=1} = \frac{1}{2}\lambda^{ijk} L_i L_j \bar{e}_k + \lambda'^{ijk} L_i Q_j \bar{d}_k + \mu'^{i} L_i H_u \text{ and} \tag{2.55}$$

$$W_{\Delta B=1} = \frac{1}{2}\lambda''^{ijk} \bar{u}_i \bar{d}_j \bar{d}_k, \tag{2.56}$$

where the couplings λ, λ', λ'' and μ' parameterise the strength of the interactions. The terms containing λ' and λ'' would lead to a short proton lifetime if unsuppressed [62]. These baryon and lepton number violating contributions can be eliminated if a new symmetry is introduced, R-parity symmetry. R-parity, P_R is defined as

$$P_R = (-1)^{3(B-L)+2s} \tag{2.57}$$

where s is the spin of the particle. The value of P_R is +1 for SM particles, and -1 for the SUSY partners of SM particles. If R-parity were violated, the values of the couplings λ' and λ'' would need to be small. It is possible to develop models of SUSY where R-parity is violated if an alternative discrete symmetry is used, or if the symmetry is spontaneously broken by the vacuum expectation value of a scalar with $P_R = -1$, for example a MSSM neutrino [62]. Using the limits on the $B^{0,\pm} \to \phi\pi^{0,\pm}$ branching fraction from BABAR, limits have been set on the values of these couplings which sets the maximum enhancement of the branching fraction of $B^0 \to \phi\phi$ at the 10^{-7} level [58]. With further information about the branching fraction of $B^0 \to \phi\phi$ and more up-to-date limits from Belle [63], more stringent limits can be placed on these couplings.

The branching fraction can also be modified in extensions to the SM that introduce a new symmetry, $U(1)'$, which gives a new Z' boson [56]. In these models, the Z' can have *family non-universality*, meaning it couples differently to the different fermion families. These models can allow tree-level FCNC interactions and enhance modes such as $B^0 \to \phi\phi$, and penguin annihilation topologies more generally [64].

In practice, due to large QCD uncertainties, it would be impossible to resolve the cause of an enlargement from a measurement of the branching fraction if the decay were observed. However, if no signal is observed at the 10^{-7} level, strict bounds may be placed on the couplings of R-parity-violating supersymmetry. The

study of $B^0 \to \phi\phi$ also provides a test of the theory calculations used to predict observables such as branching fractions. Since the non-factorizable contributions to $B^0 \to \phi\phi$, shown in Figure 2.10 [58], are also higher order contributions to the $B_s^0 \to \phi\phi$ decay, the study of $B^0 \to \phi\phi$ can shed light on these higher order contributions to more abundant modes.

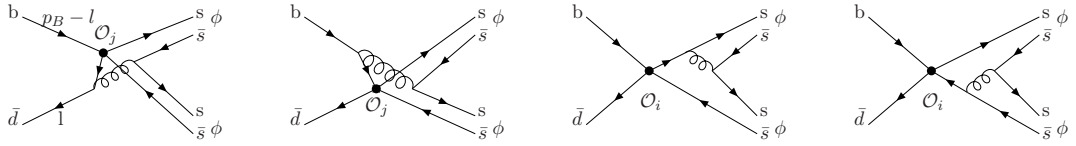

Figure 2.10 *Contributions to the $B^0 \to \phi\phi$ amplitude. The two right diagrams are factorizable and the two left diagrams are non-factorizable.*

The first searches for this mode was made by the CLEO experiment setting the first limits on the branching fraction at the level of 10^{-5} [65, 66]. Following this, the BaBar experiment set a tighter limit at $2.0{\times}10^{-7}$ [67]. LHCb have previously performed two searches for this mode. The first measurement was done with data from LHCb Run 1, corresponding to 3 fb^{-1} of data. The most recent measurement was done with 2011, 2012, 2015 and 2016 data corresponding to 5 fb^{-1} which set a limit on the branching fraction at $< 2.7 \times 10^{-8}$ at 90% confidence level [1]. These previous searches at LHCb were made alongside measurements of CP violation in $B_s^0 \to \phi\phi$ decays. The previous limit set and the existing branching fraction predictions are summarised in Figure 2.11. This thesis outlines the first dedicated search for this mode at LHCb.

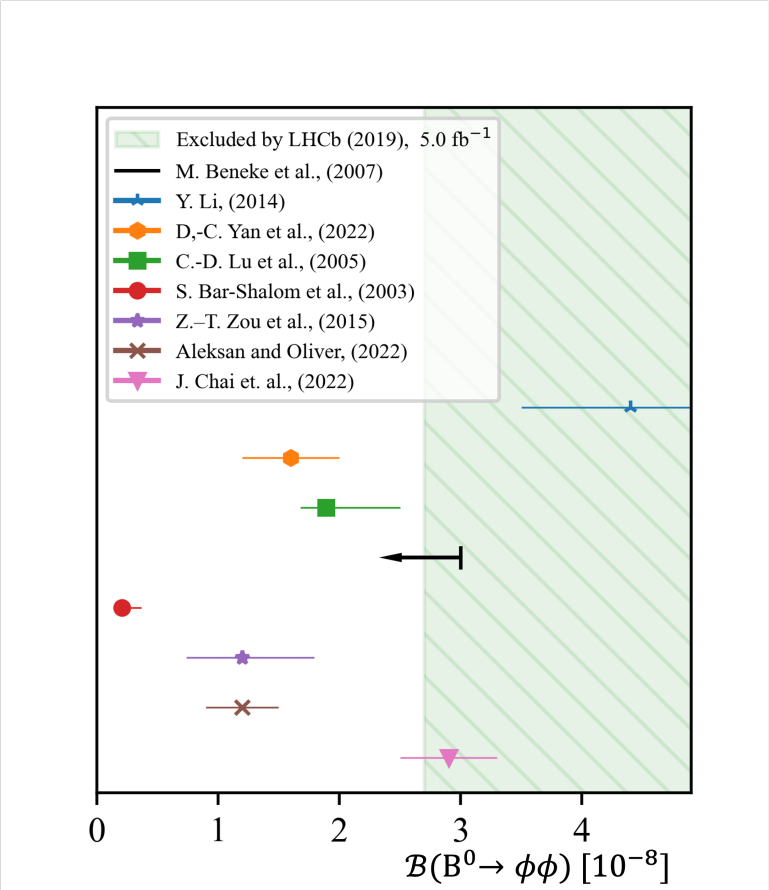

Figure 2.11 *Summary of $B^0 \to \phi\phi$ branching fractions and LHCb limit from 2019.*

Chapter 3

The LHCb Experiment

The LHCb experiment [6] is designed to study the properties of b-hadrons and is one of four main collider experiments at the Large Hadron Collider. Since LHCb started operating in 2009, it has been responsible for many discoveries in flavour physics. To highlight a few; the first observation of CP violation in the charm sector [68], precisely measuring b-hadron oscillation parameter, Δm_s [69], and strides have been made in studies of exotic pentaquarks and tetraquarks [70]. Of the 72 new hadrons discovered by experiments at the LHC, LHCb is responsible for 64 of them at the time of writing [71]. The original LHCb detector was operational from 2009 to 2018. The experiment was then upgraded, with LHCb Upgrade I operating since 2022 and still operational at the time of writing [72, 73].

In Section 3.1, the Large Hadron Collider and the four main collider experiments are introduced. Then the anatomy of the LHCb detector is described in Section 3.2, and the individual subdetectors introduced. For the original detector, each of these subdetectors is described in detail in the further sections of this Chapter, roughly grouped into tracking, Sections 3.3, 3.4 and 3.5, and particle identification, Sections 3.6, 3.7 and 3.8. The triggering of events is described in Section 3.9. The chapter closes with Section 3.10 in which the updated technology used for Upgrade I of LHCb is discussed. For the original LHCb detector, the technology is largely described in the past tense since much of the original experiment has been dismantled. For those subdetectors that are unchanged, and for the Upgrade I which is operational at the time of writing, they are described in the present tense. The proposed LHCb Upgrade II, currently due for installation in 2033, is discussed in Chapter 10.

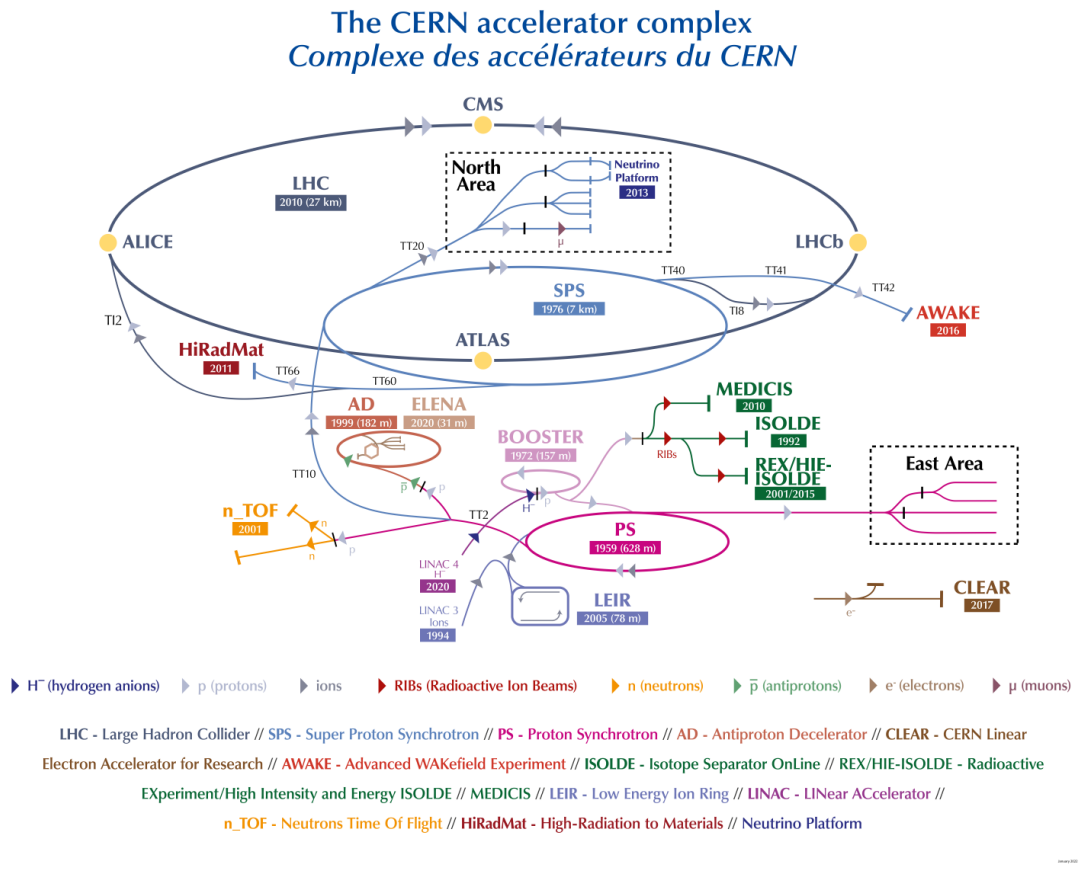

Figure 3.1 *The CERN accelerator complex. Source: CERN.*

3.1 The Large Hadron Collider

The Large Hadron Collider (LHC) is a synchrotron particle accelerator complex at the European Centre for Nuclear Research (CERN) [74]. The LHC is able to collide beams of protons or ions, such as lead, at fixed interaction points around a 27 km ring, with collisions every 25 ns. Particles are accelerated using radio frequency (RF) cavities, with quadrupole and dipole magnets forming particle bunches and directing them around the ring. As of 2022, the LHC reaches a proton-proton centre-of-mass energy of 13.6 TeV. A schematic of the accelerator complex at CERN is shown in Figure 3.1.

Each interaction point hosts an experiment collecting data from the collisions. There are four main experiments: ATLAS (A Toroidal LHC Apparatus) [75], CMS (Compact Muon Solenoid) [76], ALICE (A Large Ion Collider Experiment) [77] and LHCb [6]. The ATLAS and CMS experiments are general purpose detectors and, most notably, discovered the Higgs boson in 2012 [26, 27].

The ALICE experiment utilises lead-ion collisions to study the quark-gluon plasma [78], the state of matter shortly after the Big Bang. Heavy ions collisions at ALICE provide an avenue to study the conception of our Universe. The LHCb experiment is a single-arm forward spectrometer [6], built with the intention of reconstructing b-quark events. Despite this specific purpose, the LHCb experiment is considered a general-purpose detector with a broad physics programme. LHCb has excellent capability for electroweak studies, has a heavy-ion and fixed-target programme and has recently demonstrated ability to reconstruct helium nuclei, which has implications for understanding astrophysical processes [79].

3.2 The anatomy of the LHCb detector

The LHCb experiment is very distinguishable from a usual collider physics experiment due to its unusual forward arm design. While ATLAS and CMS are 4π detectors covering central rapidities, the LHCb detector acceptance covers the forward region $2 < \eta < 5$ where η is the pseudorapidity of a particle trajectory,

$$\eta = -\ln(\tan(\theta/2)), \tag{3.1}$$

and θ is the angle between the trajectory and the beam axis as defined in Figure 3.4. This is motivated by the fact that most b-hadron decays happen in this range, as can be seen in Figure 3.2.

The schematic of the original LHCb experiment is shown in Figure 3.3. The LHCb experiment coordinate system is right-handed, defined such that the z-axis runs parallel to the beamline. The z-axis is shown in Figure 3.3 as running from left to right. The x-y (or transverse) plane is defined such that the y-axis points upwards, and the x-axis points out of the plane of Figure 3.3. The coordinate system is further summarised in Figure 3.4.

The original detector operated from 2009 to 2018 and the Upgrade I phase detector is currently operational at the time of writing. Despite major upgrades to the majority of the subdetectors, the general anatomy of the experiment has remained similar. The timeline of the original LHCb detector is shown in Figure 3.5.

Due to the large mass of the top quark and the fact that $V_{tb} \approx 1$, the b-quark

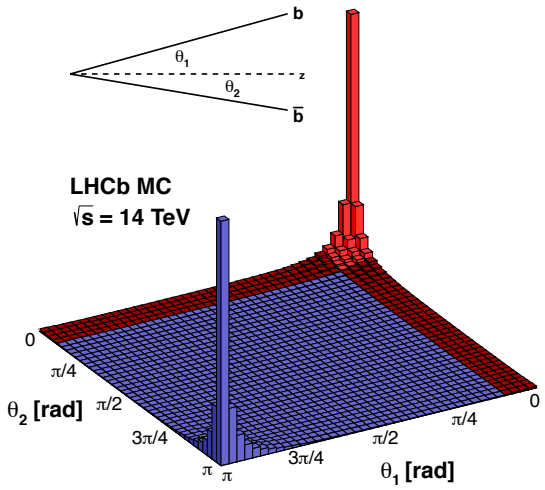

Figure 3.2 *The 3D plot shows the distribution of $b\bar{b}$ pairs production angles with respect to the z-axis (the beamline). The definition of the angles is seen in the top left. In the histogram, the red regions represent the acceptance of the LHCb experiment. This plot is made using simulated pp collisions in* PYTHIA8 *[80]. Source: Christian Elsasser, LHCb Collaboration [81].*

has a relatively long lifetime of around 1.5 ps. The b-quark cannot decay to top quarks due to its high mass and the other CKM elements, V_{cb} and V_{ub}, are very small which suppresses decays to the other quarks. Consequently, a hadron containing a b-quark will travel several millimetres from the primary vertex, where it is created in pp collisions, to the secondary vertex, where it decays. These displaced secondary vertices distinguish b-hadron decays from those of lighter quarks. Since LHCb is designed with b-hadrons in mind, it is clear that a precise determination of the primary and secondary vertices is crucial to the performance of LHCb. The Vertex Locator (VELO) subdetector is a tracking detector surrounding the collision point, responsible for reconstructing interaction vertices. This information is used to trigger events and reconstruct tracks.

To measure particle momenta, the trajectories of the particles through a magnetic field need to be reconstructed. The magnetic field is provided by a large dipole magnet [83]. To map out the paths, hits from the VELO and each of the four tracking stations are used. A tracking station (TT) is placed upstream of the magnet, following RICH 1 [84]. Three further stations, the T-stations, are placed downstream of the magnet, before RICH 2 [84, 85].

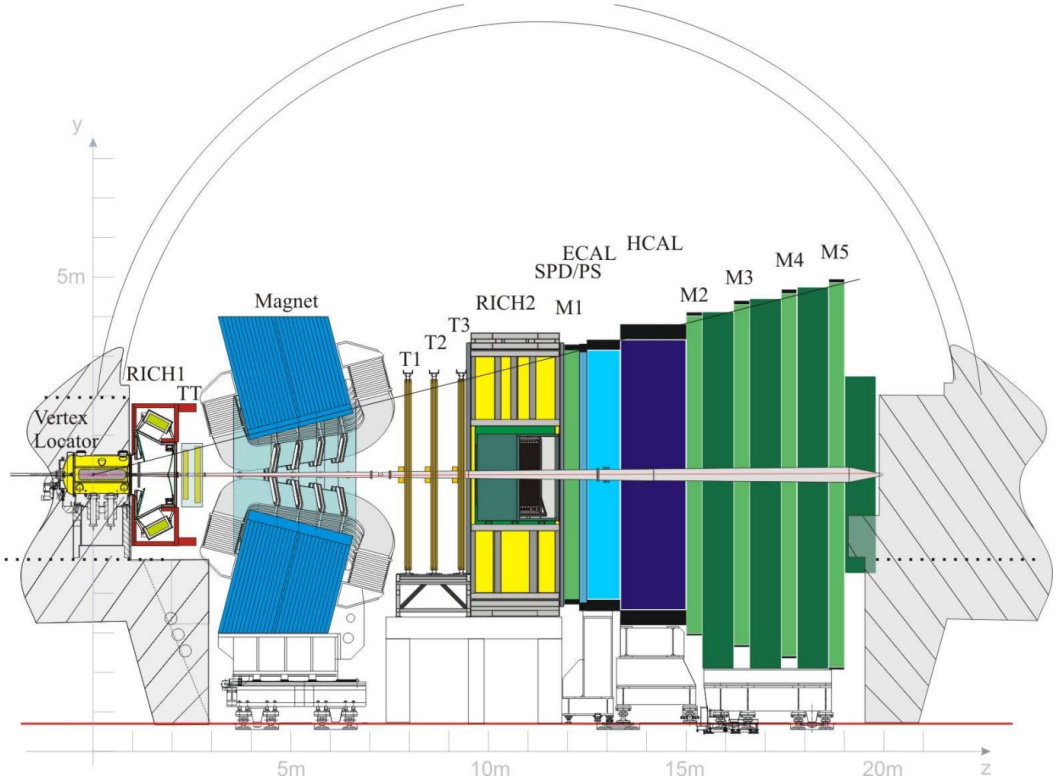

Figure 3.3 *The LHCb detector is shown in the Run 1 and Run 2 era of the experiment. Each subdetector is labelled, and the z-positions of the detectors can be seen from the scale along the bottom of the figure. Source: the LHCb Collaboration [6]..*

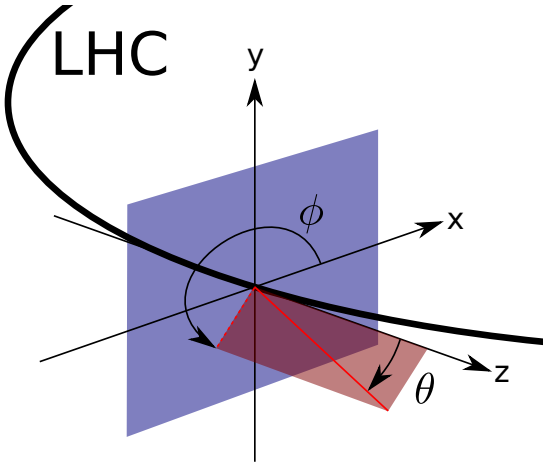

Figure 3.4 *The right-handed LHC coordinate system. Source: used with permission from Benjamin Wynne [82].*

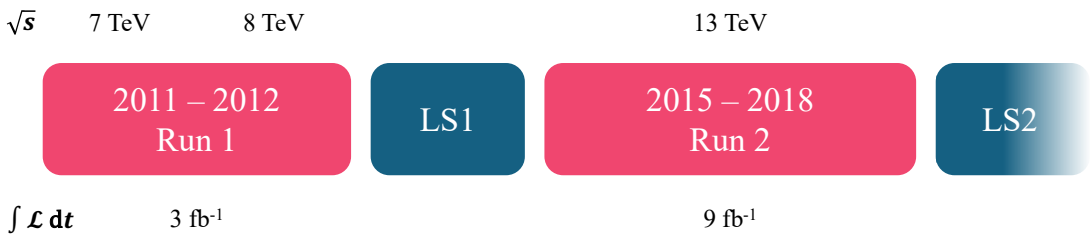

Figure 3.5 *Timeline of the the original LHCb detector, showing the centre-of-mass energies and integrated luminosities of the run periods.*

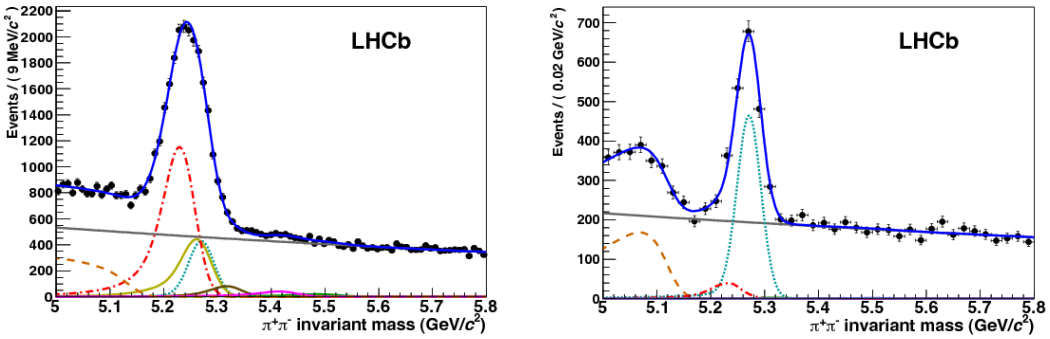

Figure 3.6 *These plots shown the $\pi^+\pi^-$ invariant mass distribution from selected $B \to hh$ decays before applying RICH PID (left) and after applying RICH PID (right) [86]. The turquoise dotted line represents the true $B \to hh$ decays to be studied, the solid grey line is combinatorial background and all other lines represent some background from misidentification.*

Another key ingredient of event reconstruction is particle identification (PID) which is required for flavour tagging, triggering and reduction of combinatorial background [86]. At LHCb, information to identify charged hadrons (pions, kaons and protons) is provided by the Ring Imaging Cherenkov (RICH) detectors. The RICH detectors work on the principle of Cherenkov radiation [87]. The material inside the RICH detectors is chosen such that speed of the charged particles will exceed the speed of light. This leads to cones of Cherenkov light being produced. These cones are detected as a ring of photons that are characteristic of the particle traversing these detectors. The size and other features of the produced ring allows the particle to be identified. There are two RICH detectors, one each side of the magnet. The power of the RICH detectors is demonstrated in Figure 3.6, which shows the dipion invariant mass distribution for selected $B \to hh$ decays, where h represents any hadron, before and after applying RICH PID. The reconstructed tracks are then combined with the particle identification information to provide a mass hypothesis to understand the four-momentum of the particles.

For most of the decay products in an event the final measurements are taken in the calorimeter system, beyond the tracking stations. Stable hadrons such as kaons and pions will typically shower in the hadronic calorimeter, while electrons and photons will shower in the electromagnetic calorimeter. Each of these provides a measure of the energy of the particles that shower within them and further particle identification.

At the rear of the LHCb experiment is where the muon stations are located. Muons are the only reconstructable particles that are able to pass through the calorimeters unscathed, and have a lifetime long enough to make it all the way to the very edge. These stations provide muon track trajectories to provide muon identification.

Both the original and upgraded detector use this structure for the subdetectors. The motivation for LHCb Upgrade I is to remove the low-level hardware trigger that cuts harshly on track p_T. By removing this trigger, the detector can be read out at the bunch crossing rate of 40 MHz. The trigger then becomes flexible and improves efficiencies for modes such as $B_s^0 \to \phi\phi$ by a factor of two [72]. The instantaneous luminosity delivered to LHCb is increased from 4×10^{32} cm^{-2}s^{-1} to 2×10^{33} cm^{-2}s^{-1}.

3.3 Vertex Locator

The VELO detector [88] is formed of two halves on each side of the beam pipe. Each half hosts a series of tracking layers for primary and secondary vertex reconstruction. The halves are housed in an RF foil which protects the detector modules from harmful beam effects and separates the VELO vacuum from that of the beam. When beam is injected, the beams are broad and get narrowed during the ramp up to collision energy. Because of this, the VELO halves are mechanically retracted to protect the detector. When the beam becomes stable and narrow, the halves are closed together.

The original VELO that operated during Run 1 and Run 2 of the LHC used r and φ silicon microstrip detectors to reconstruct the tracks of the primary vertices [88]. Silicon detectors are made of semiconductors, where charged tracks liberate electron and hole pairs which generates a current. During data taking, the modules were positioned 7 mm from the LHC beam, with the active silicon 8.2 mm

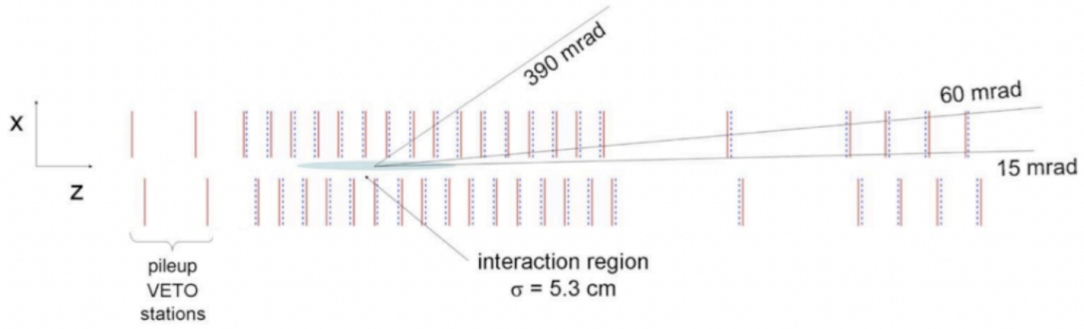

Figure 3.7 *The positions of the VELO modules are shown. The interaction region is represented by a light blue oval. The r sensors are represented by solid red lines and the φ sensors are represented by dotted blue lines [6].*

away [89]. There were 21 pairs of modules, 42 modules in total. The module pairs surrounded the interaction region, with modules upstream and downstream of the region. The positions of the modules can be seen in Figure 3.7. The modules were formed of r and φ sensors, shown in Figure 3.8. The φ sensors had strips that extended from the centre of the module radially towards the outer edge, giving a measurement of the azimuthal angle of the track position. The r sensors had strips in concentric semi-circles around the centres giving the radial distance of the track from the beam. The combination of r and φ information allow for the reconstruction of a 3D space point. In addition to the full modules, 4 r sensors, 2 per half, were included upstream of the collision point to form the pile-up system [90]. For vertices with 25 tracks, the primary vertex resolution was 13 µm in the transverse plane and 71 µm along the beam axis [89]. An important quantity in the VELO is the impact parameter (IP) of a track. The IP of a track is the distance of closest approach of the track to the position of the primary vertex. The VELO is able to reconstruct the primary vertex position within 35 µm for tracks with a momentum greater than 1 GeV/c [89]. Since the tracks in the VELO are far from the magnetic field, they are straight and therefore used to initiate the track reconstruction as discussed further in Section 3.11.

3.4 The LHCb magnet

A large warm dipole magnet is used to deflect charged particle tracks [83]. This allows LHCb to measure the momentum of charged particles within the acceptance of 300 mrad horizontally and 200 mrad vertically. The polarity of the

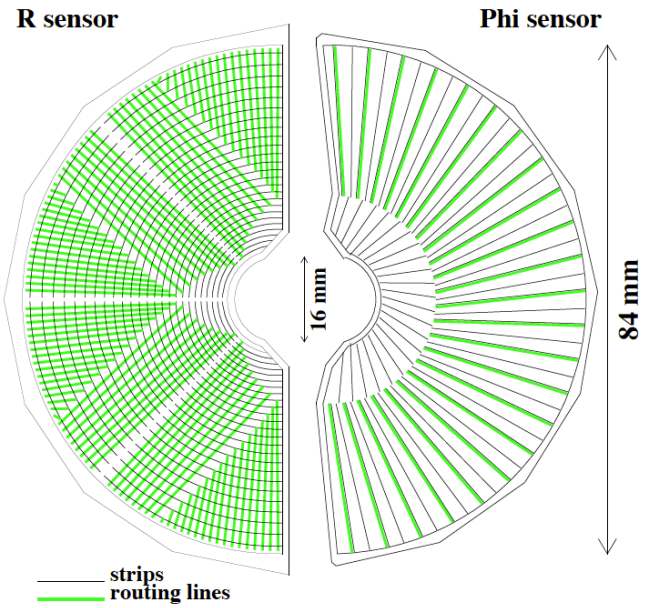

Figure 3.8 *The r (left) and φ (right) sensors that formed the modules of the original Vertex Locator. The silicon strips are represented by the black lines. [89]*

magnet can be swapped so that the field can point up and down. The design of LHCb requires that a track of 10 m should be subject to an integrated magnetic field of 4 Tm. However, there is a constraint from the RICH systems that require the field to stay below 2 mT in the region of the RICH detectors. The magnet has saddle-shaped coils, with a 'window-frame' iron yoke as shown in Figure 3.9.

The yoke is formed of laminated low-carbon steel plates. These are each 100 mm thick with a maximum weight of 25 tons each. The magnet coils are each formed of pure Al-99.7[1] 'pancakes', which are arranged into 5 sets of triplets per magnet coil. The total mass of the coils and iron yoke is 1600 tons.

A precise knowledge of the magnetic field is crucial to achieve the required momentum resolution. To achieve this, it is necessary to understand the integrated magnetic field to a precision of 0.01%, and the position of the peak magnetic field to a few millimetres [6]. Using an array of Hall probes, the magnetic field is mapped along the z-axis and shown in Figure 3.10. Using this method, the relative precision of the field map is found to be 4×10^{-4} in the tracking volume [6].

[1]Aluminium with a purity of at least 99.7%.

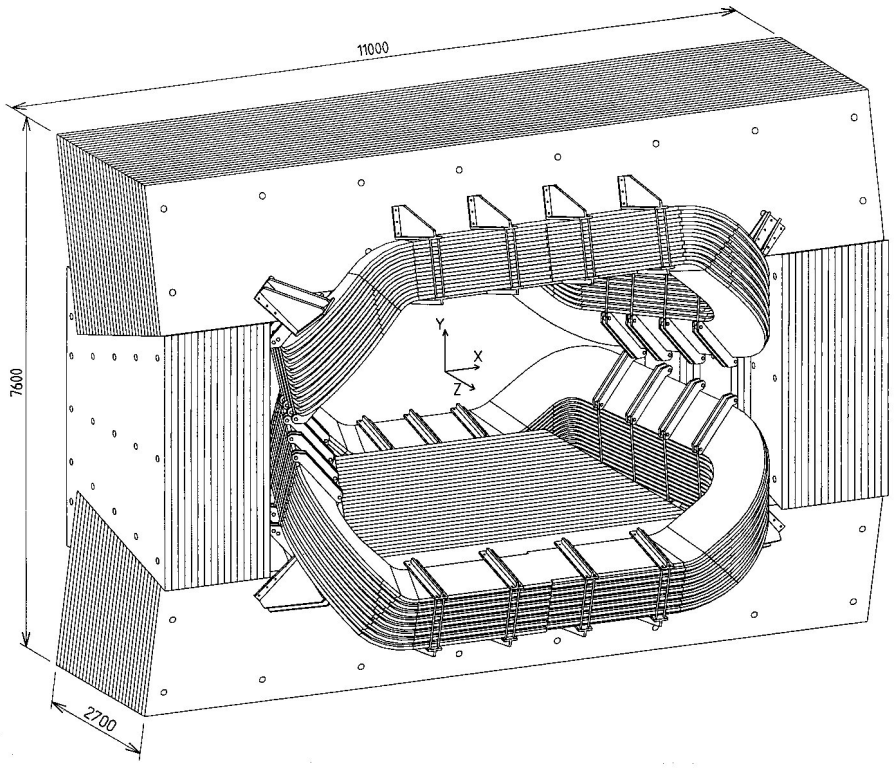

Figure 3.9 *The LHCb dipole magnet, formed of saddle-shaped coils surrounded by a 'window-frame' iron yoke. Scale values in millimetres [6].*

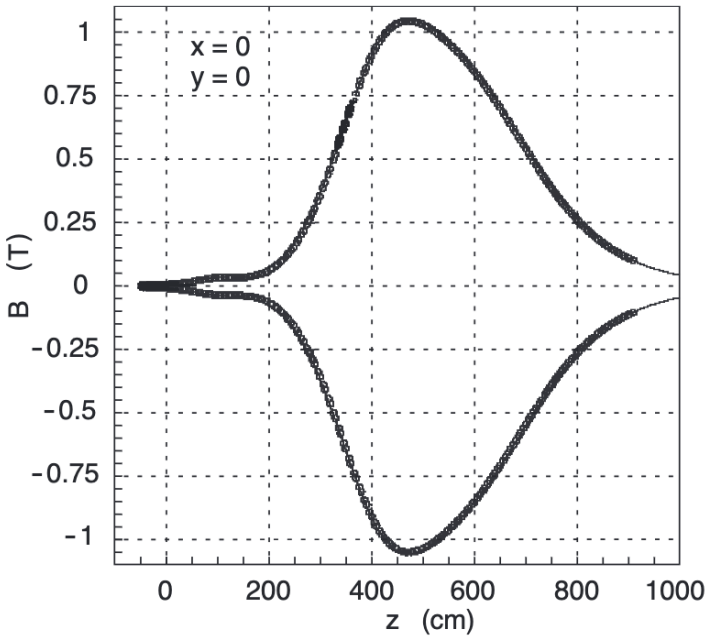

Figure 3.10 *The magnetic field strength of the LHCb dipole magnet along the beampipe direction, z. Measurements of the field strength inside LHCb were mapped using an array of Hall probes [6].*

3.5 Tracking stations

The momenta of charged particle tracks, and their trajectories, are determined using the tracking detectors and the VELO. The trackers are formed of many stations, each consisting of several layers, to provide multiple particle hit positions for reconstructing the track. During the Run 1 and Run 2 era, the tracking detectors consisted of the Silicon Tracker (ST) [84], utilising silicon microstrip technology, and the Outer Tracker (OT) [85], which consisted of straw tubes.

The ST comprised the Tracker Turicensis[2] (TT), positioned upstream of the magnet, and three Inner Tracker (IT) stations downstream of the magnet. The Outer Tracker comprised three stations. The IT and OT stations are paired into the T-stations, referred to as T1, T2 and T3.

Tracker Turicensis

The TT station, shown on the left of Figure 3.11, was formed of four layers of silicon microstrip sensors with a strip pitch of 183 µm [91]. The layers were arranged in a (x, u, v, x) geometry. This pertains to the angle between the strips and the vertical axis. In the first and last layers the strips were vertical, while in the second and third layers the modules are rotated such that the strips formed an angle of -5° and $+5^\circ$ respectively to allow 3D reconstruction. The TT covered the full LHCb acceptance with a width of 150 cm and a height of 150 cm. The TT achieved a hit resolution of 59 µm and a hit efficiency greater that 99% [92].

The tracks between the VELO and the TT experience the fringe field from the magnet, and hits from the VELO and TT could be quickly combined to give a rough estimation of the track momentum. The TT was also used for measuring longer lived particles, such as the K_S^0, which decays after it leaves the VELO.

The Inner Tracker

The IT covered the inner acceptance of the T-stations using a cross shape, with a width of 120 cm and a height of 40 cm. An IT station is shown on the right

[2]Originally called the Trigger Tracker, the TT was renamed after tracking information was removed from the trigger. The renaming is an homage to the Zurich group that led the development, as the Latin name for Zurich is *Turicum*.

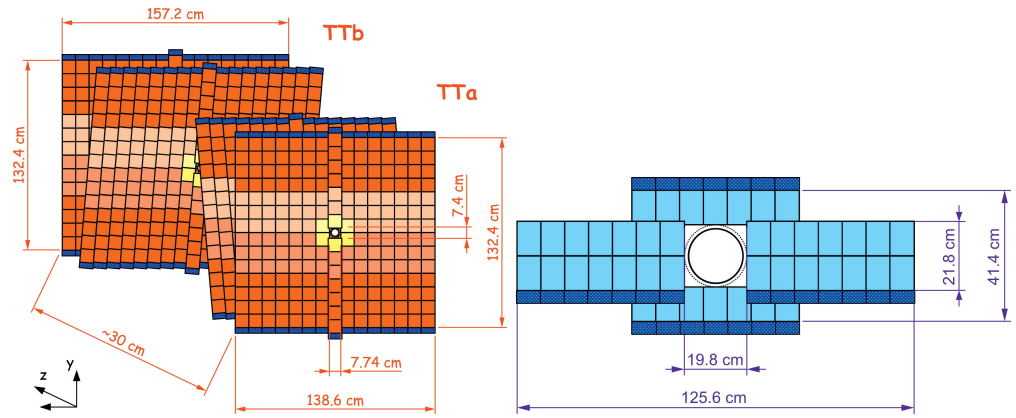

Figure 3.11 *On the left, the layers of the TT station are shown, clearly highlighting the (x, u, v, x) geometry. On the right, the arrangement of the silicon modules in the inner tracker stations is shown. [91].*

of Figure 3.11. As with the TT, silicon microstrip sensors were used with a pitch of 198 µm [91]. A hit resolution of 50 µm was achieved with a hit efficiency of greater than 98% [92].

The Outer Tracker

The OT provided complimentary acceptance to the IT at low pseudorapidity. In these regions, tracks are physically further apart and less granularity is required. The OT was a gaseous straw-tube drift time detector with a gas mixture of 70% Argon, 28.5% carbon dioxide and 1.5% oxygen, giving a drift time of less than 50 ns and a position resolution of around 200 µm [93]. The tubes consisted of a cylindrical outer cathode with a wire anode through the centre. When a charged particle passes through a tube, the gases ionise and the liberated electrons drift towards the anode and are collected. The distance of the track to the wire was inferred from the measured electron drift time. This is demonstrated schematically in Figure 3.12.

The OT consisted of 3 stations. Each station contained 4 sets of double layers in the same (x, u, v, x) geometry as the TT. These double layers were two staggered monolayers of straw tubes and a schematic of this is shown in Figure 3.13. A double-layer in the station was formed of 22 modules. These were arranged with 14 long modules out to either side, each with 256 tubes, and 8 short modules above and below the beampipe, with 128 tubes each. Each station therefore had 88 modules total, giving 264 modules and more than 55,000 straw tubes in the full OT [6].

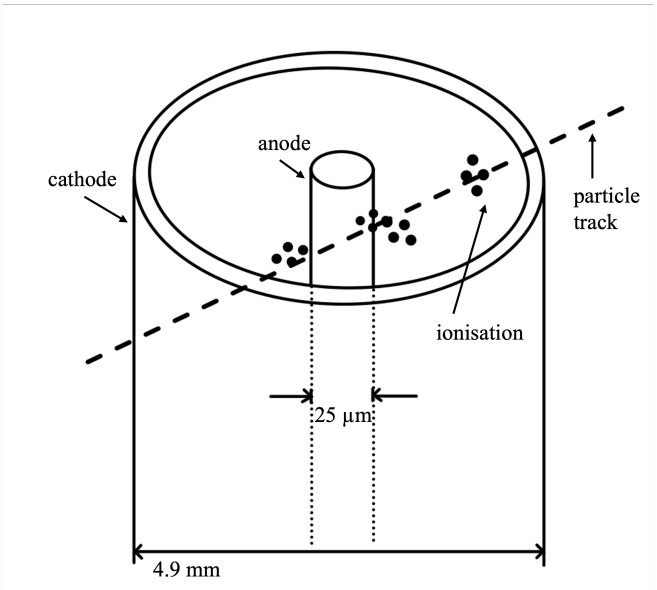

Figure 3.12 *Illustration showing the structure of a straw tube. Electrons from the ionisation clusters drift to the anode to produce signal. Not to scale.*

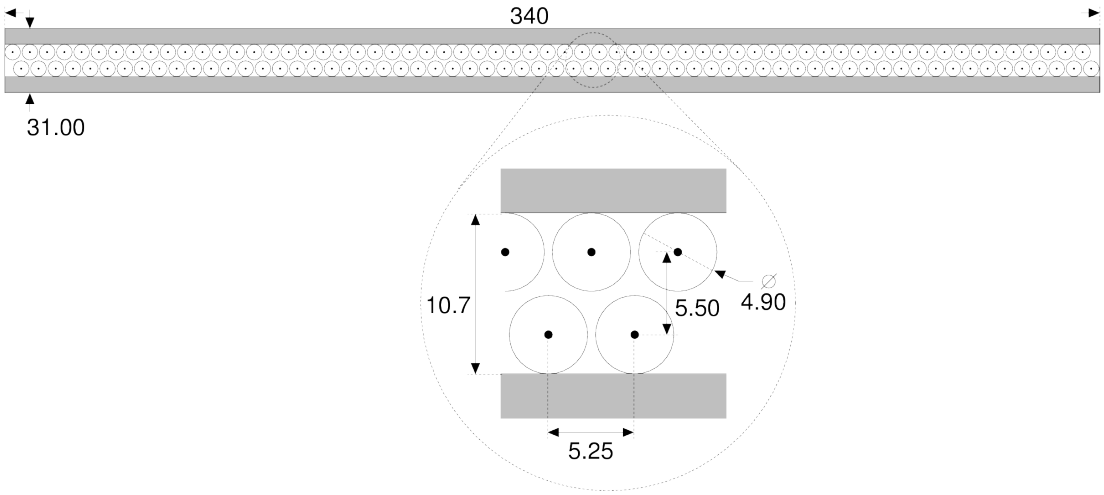

Figure 3.13 *Schematic showing how the double layers were constructed of two monolayers of straw tubes. Four of these double layers constituted one station of the outer tracker [93].*

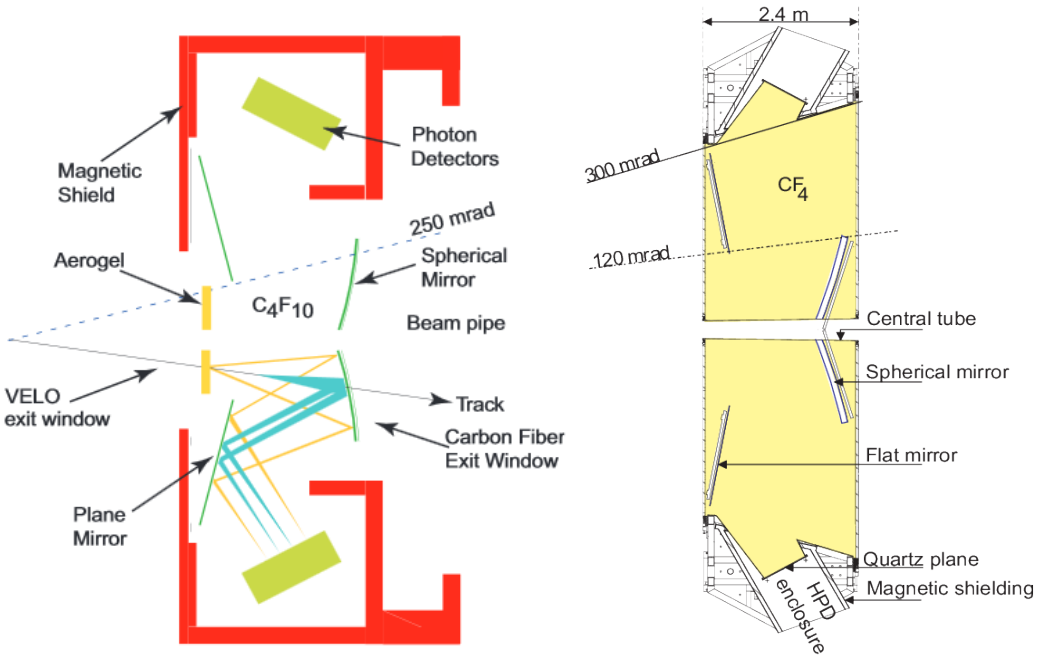

Figure 3.14 *The RICH detectors in LHCb. RICH 1, shown on the left, is positioned upstream of the magnet. RICH 2, shown on the right, is positioned downstream of the magnet. The mirrors from which the Cherenkov light is reflected are labelled, along with the photon detectors used to collect the light [95].*

3.6 Ring Imaging Cherenkov detectors

The RICH system [94] is split into two detectors; RICH 1 upstream of the LHCb magnet, and RICH 2 downstream of the magnet. Each RICH detector is split into two halves, with the RICH 1 detector being split above and below the beampipe, and the RICH 2 detector being split to the left and right. The RICH 1 detector targets low and intermediate momentum tracks between 2 and 40 GeV/c, and RICH 2 targets the high momentum range from 15 to 100 GeV/c [86]. Each RICH detector is filled with a flourocarbon gases as Cherenkov radiators; C_4F_{10} is used in RICH 1 and CF_4 in RICH 2. In Run 1, there was an additional aerogel radiator in RICH 1 to aid proton-kaon discrimination that was later removed [86]. When charged particles pass through the RICH detectors, the Cherenkov radiation emitted is reflected into photon detectors using a primary circular mirror and secondary flat mirror, shown in Figure 3.14.

Hybrid photon detectors (HPDs) were used during Run 1 and 2 to collect the Cherenkov photons. These consisted of vacuum tubes with a quartz window and multialkali photocathode, with photons focussed onto silicon pixel arrays [86].

RICH 1 contained 196 such tubes and RICH 2 contained 288. For the C_4F_{10} radiator in RICH 1, a Cherenkov angle resolution of 1.688 $\pm$ 0.002 mrad was achieved, whilst for the CF_4 gas in RICH 2 the resolution was 0.68 $\pm$ 0.02 mrad [86]. In terms of efficiency, this translated to a kaon efficiency of 95% with a 10% pion misidentification rate, or 85% kaon efficiency for 3% pion misidentification rate, over the full momentum range accessible to the RICH.

3.7 Calorimeters

The original LHCb experiment deployed a four-piece calorimeter system [96] to provide particle identification and a measure of energy of electrons, photons and hadrons. The four sub-detetctors were; the Scintillating Pad Detector (SPD), the preshower (PS), the electromagnetic calorimeter (ECAL) and the hadronic calorimeter (HCAL). The detector layout is shown in Figure 3.15. The SPD and PS systems were each formed of a single layer of scintillating pads, separated from one another by a layer of lead. A wavelength-shifting (WLS) fibre was coiled inside each cell of the scintillating pads, and the photons from these fibres were collected with multi-anode photomultiplier tubes (MaPMTs). The purpose of the SPD was to separate neutral particles from charged particles, and the PS provided electron and photon PID for the low level hardware trigger. These were removed for Upgrade I.

The ECAL, still in operation, uses alternating scintillating planes and lead plates to detect electrons and photons. There are 67 scintillator planes and 66 lead planes, each separated from one another by 120 µm-thick paper sheets. The scintillation photons are collected in WLS fibres that run parallel to the beampipe. The HCAL, still in operation, is formed of an iron-scintillator sampling structure that is arranged such that the layers are parallel to the beam pipe. Again, WLS fibres are used to read out the scintillation light.

3.8 Muon stations

The original LHCb muon system consisted of 5 stations, M1 - M5 [98]. Station M1 was located before the calorimeters for the purpose of improving the p_T measurements in the L0 trigger. Stations M2 - M5, still in operation, are

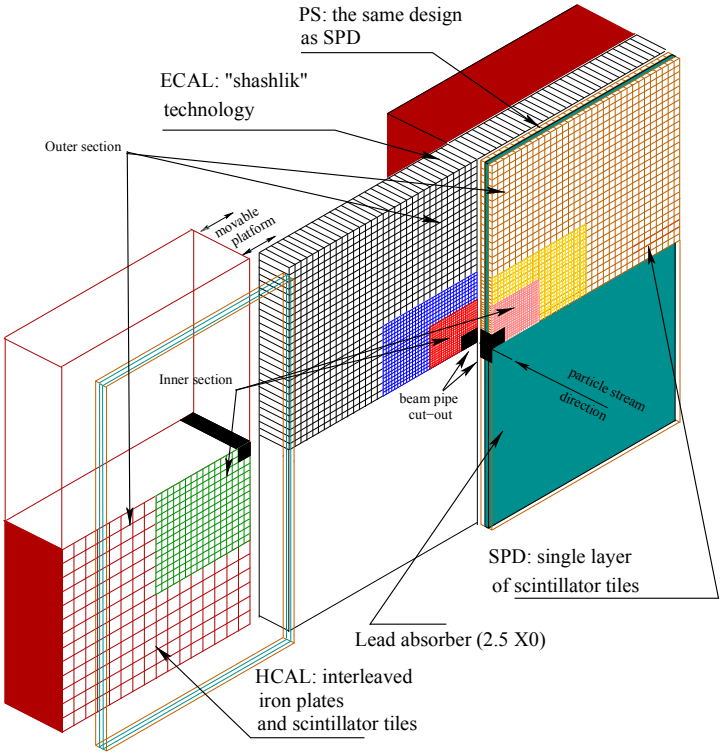

Figure 3.15 *The LHCb calorimeter system during Run 1 and Run 2. For Upgrade 1, the SPD and PS detectors have been removed [97].*

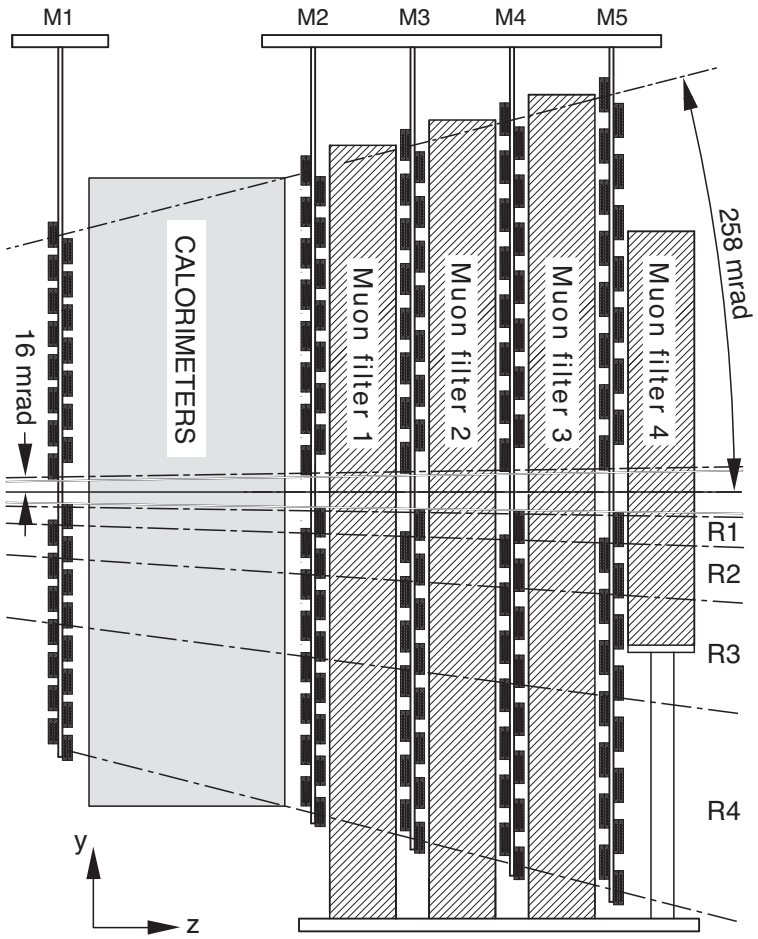

Figure 3.16 *The original LHCb muon system is shown. For Upgrade I, the M1 station upstream of the calorimeters has been removed [6].*

positioned after the calorimeters. The M2 - M5 stations are interleaved with 80 cm-thick iron absorbers. The muon system can be seen in Figure 3.16.

Stations M2 - M5 exclusively use multiwire proportional chambers (MWPCs) to detect muon tracks; M1 additionally used gas electron multipliers (GEMs) in the inner regions since it was subject to larger radiation doses [6]. In order to reach the performance needed, a gas mixture of 40% Ar, 55% CO_2 and 5% CF_4 is used in the MWPCs and 45% Ar, 15% CO_2 and 40% CF_4 was used in the GEMs [99].

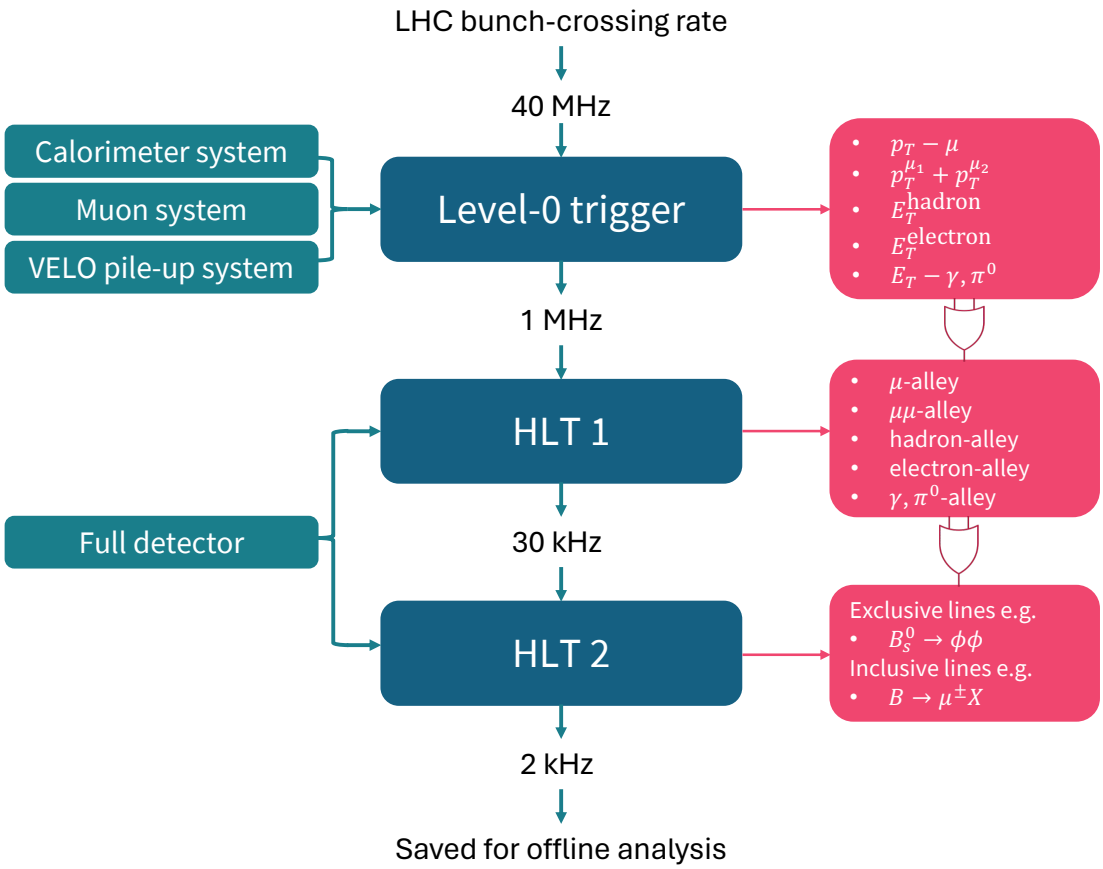

Figure 3.17 *The original LHCb trigger chain. The central column shows the trigger stages and the output rate of each. The left column shows the information that was used at each of the stages, and the right column gives the various categories that events are grouped by at each stage. Figure adapted from those in [6].*

3.9 Trigger

The LHCb trigger system [90] is used to select events of interest. The LHC bunch-crossing rate is 40 MHz and data cannot be saved at this rate. A series of triggers are utilised to study portions of the event and make a decision on whether or not it should be looked at further or saved. The original trigger system had two levels; the level-0 hardware trigger (L0) and the high-level software trigger (HLT). The L0 trigger used information from a subset of detectors to make an initial reduction in the rate from 40 MHz to 1 MHz. The HLT used information from the full detector to further reduce the event rate from L0 to 2 kHz which is the rate at which events can be saved. The HLT was subdivided into HLT1 and HLT2. The full chain is shown in Figure 3.17.

Level-0 trigger

The L0 trigger was employed to reduce the event rate from the bunch-crossing rate of 40 MHz to just 1 MHz. To do this, information was taken from the VELO pile-up system, Calorimeter system, and Muon system. The heavy mass of b-hadrons leads to high p_T and E_T decay products. To select these, the L0 trigger found the highest E_T hadron, photon and electron clusters and the two highest p_T muons from the muon systems [6]. The VELO pile-up system gave a measure of the charge multiplicity in the backward direction, predicting the number of pp interactions in the bunch crossing. The Calorimeter system looked for high E_T particles, and identified them using the SPD, PS, ECAL and HCAL information. The number of SPD cells with hits was also used to estimate charged track multiplicity [6]. The Muon system performed a muon track reconstruction, with a resolution on the p_T of around 20% [6]. Per quadrant, the two highest p_T muons were selected. This information was combined in the L0 Decision Unit (DU) to give a single L0 decision. For the selection of $B^0_{(s)} \to \phi\phi$ events, the Hadron L0 trigger is used. This trigger imposes a restriction on the minimum transverse energy, E_T, of a cluster at around 3.5 GeV [100].

HLT1

The first layer of the HLT, HLT1, took the rate from 1 MHz to 30 kHz by refining the L0 candidates. It can be seen in Figure 3.17 that the 'alleys' used in HLT1 were very closely aligned with the L0 decision parameters. For hadronic channels, this trigger strategy was susceptible to ghost tracks, tracks with hits from multiple particles [101]. To combat this, a single-track HLT1 trigger was developed [102]. The procedure for selection in this trigger is as follows. The VELO tracks first were assessed, without extrapolating them to the T-stations, to find those that are most likely to come from B-decays. This selection was based on the IP of the VELO track, the number of hits assigned to the track, and the expected number of hits on the track given the direction of the track and the first point on the track. Selected VELO tracks were then extrapolated to the T-stations to find those with a momentum greater than 8 GeV/c and a p_T greater than 800 MeV/c. The remaining tracks were fitted with a Kalman filter [103], and outliers removed based on track fit quality information.

For the analysis of $B^0_{(s)} \to \phi\phi$ events the HLT1 lines used are the `Hlt1TrackAllL0`

line in Run 1 and the `Hlt1TrackMVA` and `Hlt1TwoTrackMVA` lines in Run 2. The `Hlt1TrackAllL0` line selects displaced secondary vertices [104]. These lines both select good tracks that are not from the PV. The `Hlt1TrackMVA` line makes selection on the track p_T and displacement while the `Hlt1TwoTrackMVA` line uses a classifier trained on track fit and kinematic variables to select events [100].

HLT2

Following HLT1, the second layer, HLT2, now had a rate low enough to perform full pattern recognition on the events that survived HLT1. The HLT2 had two types of trigger lines, inclusive and exclusive. The inclusive lines, for example the $B \to \mu^{\pm} X$ line, only partially reconstructed the B decay. The exclusive lines, for example $B_s^0 \to \phi\phi$, fully reconstructed the decay. Additionally, there are topological trigger lines, which selected events based on track fit quality, IP and electron and muon content [104]. The topological triggers looked for 2-, 3- and 4-body candidates by considering the distance of closest approach, (DOCA), of the track objects. To select events, cuts were made on the sum of the p_T, the minimum p_T, mass, DOCA, IPχ^2, flight distance χ^2 and the corrected mass[3] [104].

3.10 Upgrade 1

As mentioned in Section 3.2, the LHCb experiment is currently in its Upgrade I phase. The detector is now read out fully at the nominal bunch-crossing rate of 40 MHz and the full luminosity of the LHC is delivered to the LHCb interaction point. The upgraded detector can be seen in Figure 3.18.

3.10.1 Vertex Locator

To meet the upgrade conditions of a readout rate of 40 MHz and higher instantaneous luminosity, the VELO is replaced with a new system utilising hybrid silicon pixel sensors [105]. On each side of a module there are two tiles of pixels, oriented perpendicular to one another in an 'L' shape. The schematic

[3]The corrected mass is calculated by taking into account any missing transverse momentum as defined by the PV and decay vertex.

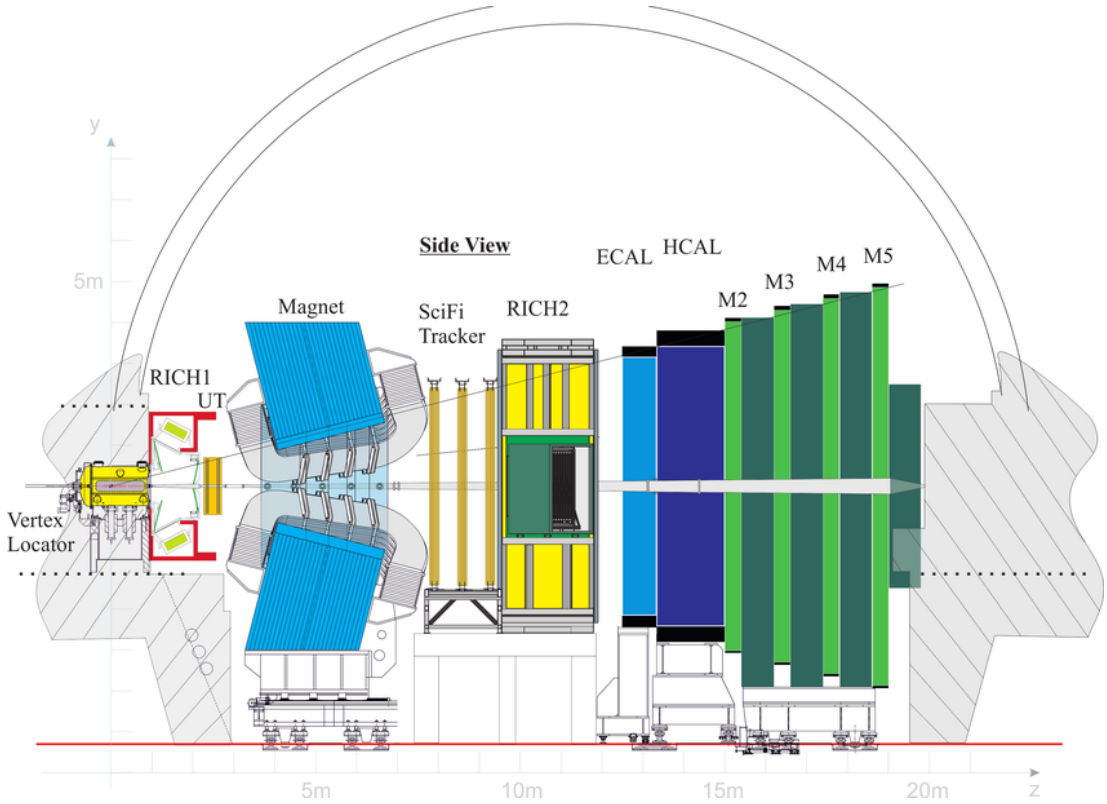

Figure 3.18 *The LHCb detector is shown in the Upgrade I era of the experiment. Each subdetector is labelled, and the z-positions of the detectors can be seen from the scale along the bottom of the figure. The most noteworthy changes from the original detector are; the shift from TT and T1-3 to the UT and SciFi, the removal of the M1 muon station and the removal of the SPD and PS in the calorimeter system. Source: the LHCb Collaboration [73].*

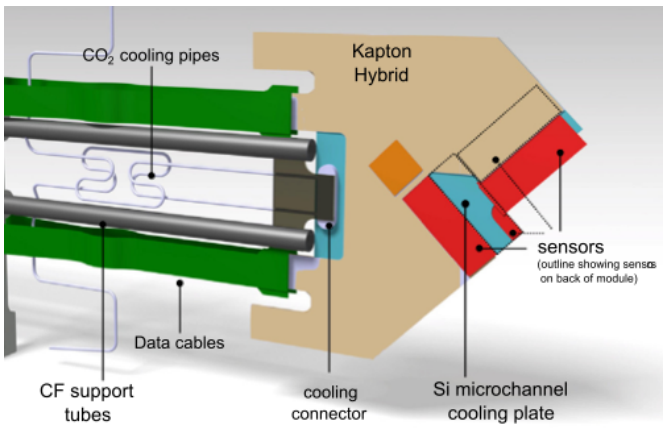

Figure 3.19 *A rendering of a module for use in the Upgrade I Vertex Locator. The sensitive silicone is shown by the outlined rectangles forming an 'L' shape at the edge of the Kapton Hybrid [106].*

shown in Figure 3.19 shows the layouts of the silicon sensors, with two tiles each bonded to the back and front side of the readout hybrid.

In order for the VELO detector to cover the full acceptance of LHCb, over $2 < \eta < 5$, a total of 52 modules, 26 per half, are required. This includes the modules upstream of the interaction point. The new VELO is able to go closer to the beam, with the inner radius of the RF foil reduced from 5.5 mm to 3.5 mm and the inner radius of the active silicon reduced from 8.2 mm to 5.1 mm [73].

3.10.2 Upstream tracker and SciFi system

The Upstream Tracker (UT) replaces the TT detector of the original LHCb. Similar to the TT (Figure 3.20), the UT is a silicon microstrip detector situated between RICH 1 and the magnet. Like the TT, the UT is formed of four layers of sensors in the (x, u, v, x) geometry. The modules that form the UT come in four types; A, B, C and D. The A-type modules are n-substrate sensors with 512 p-type strips, each with a pitch of 187.5 µm. Conversely, The B-, C- and D-type modules are p-substrate sensors with n-type strips. The pitch of the n-type strips is half that of the p-type strips at 97.5 µm and so each of the B-, C- and D-type modules has 1024 of these strips. The differences between the B-, C- and D-type modules relates to the lengths of the strips. B-type modules have the longest strips, with C-type and D-type having the shortest. D-type modules are also curved to fit tightly around the beampipe.

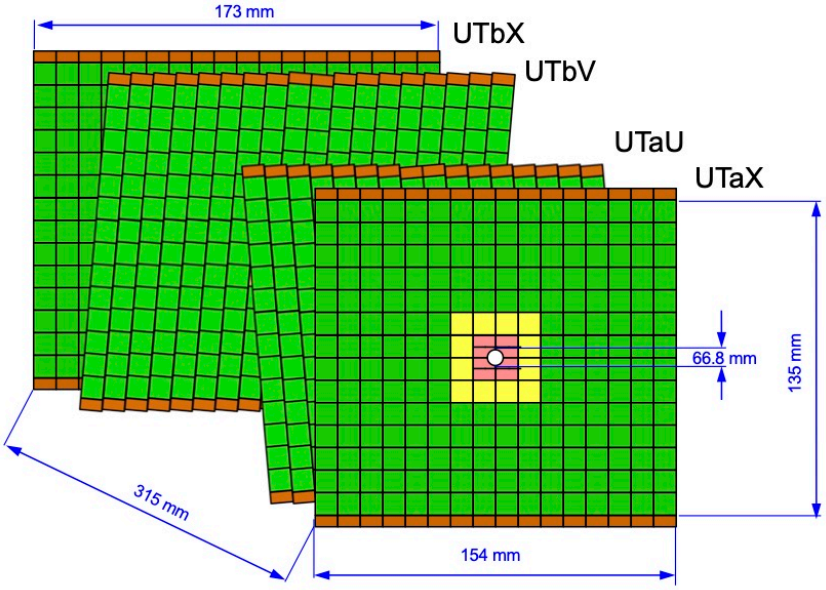

Figure 3.20 *The layers that form the upstream tracking station in LHCb Upgrade I. The individually coloured squares represent individual modules [73].*

The SciFi tracker [107] replaces the downstream IT and OT trackers of the original detector. As with the IT and OT, the SciFi tracker is composed of 3 stations, each with 4 tracking layers in the usual (x, u, v, x) layout. This gives 12 tracking layers in total. The principle of the SciFi tracker is that charged particles will create scintillation light when passing through the plastic fibres. This light will internally reflect and transmit along the fibres, to be captured by silicon photomultipliers. The simplest unit in the SciFi is the fibre itself. They are each 250 µm in diameter and are 2.4 m long, with the exception of those around the beam pipe. Fibres are combined to form fibre mats, consisting of 6 staggered layers of the fibres, as seen in Figure 3.21. Each mat is 13 cm wide and the full length of a fibre; 8 mats combined form a module. The mats in a module are combined in 4 columns and 2 rows, with the rows separated by a mirror. Each station has two halves, one to each the left and right of the beampipe. A schematic of the SciFi stations is shown in Figure 3.22. The SciFi modules [108] are capable of achieving at least 99% hit efficiency and have position resolution of 70 µm.

3.10.3 Ring Imaging Cherenkov detectors

Several updates to the RICH system have been made over Upgrade I [109]. The main challenge for RICH in Upgrade I is the increase in instantaneous luminosity

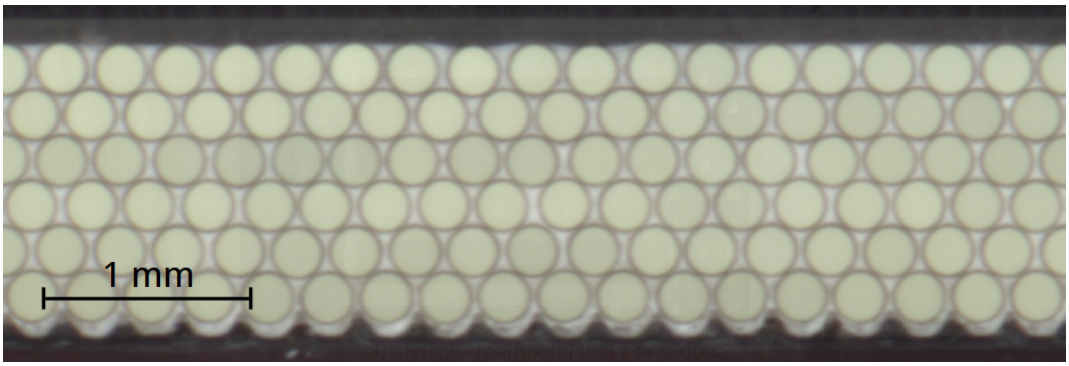

Figure 3.21 *The staggered fibres forming a SciFi mat are shown from a top-down view, looking down into the fibres. The 6 layers that form the mats can be seen [108].*

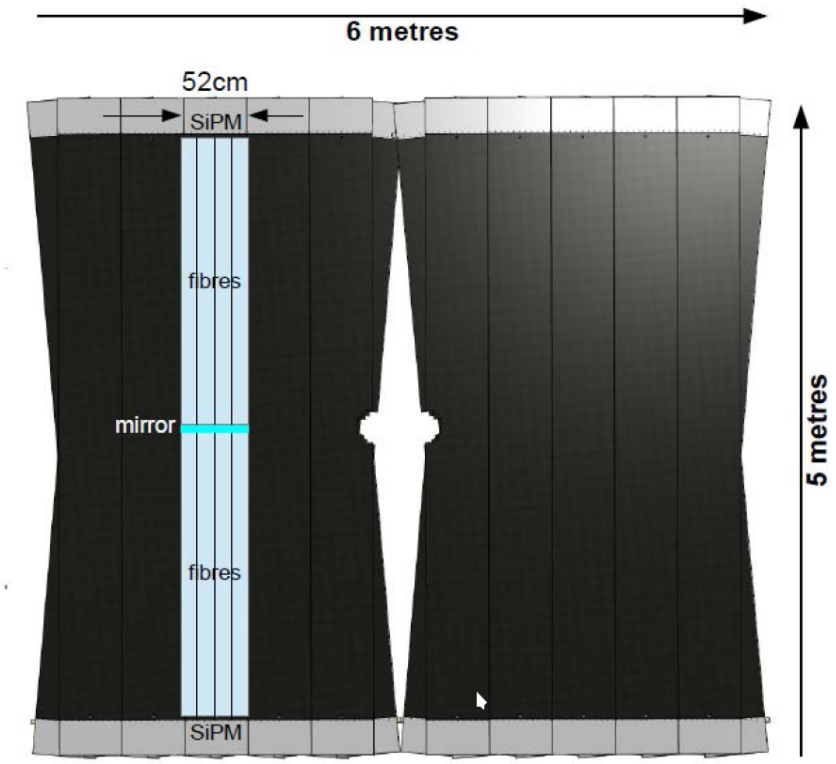

Figure 3.22 *The SciFi system is shown. The central module on the right is shown as its constituent parts, with the fibres, mirror and silicon photomultipliers labelled. It should be noted that this schematic shows the detector in an open position, and in operation they are not separated [108].*

and therefore larger event multiplicity. The optics of the RICH 1 subdetector are changed by enlarging the tilted spherical mirror from 2.7 m to 3.7 m, and by moving the focal plane. This increases the size of the Cherenkov rings, spreading the distribution of photons more evenly. This keeps the peak occupancy of the photon detectors below 30% [73].

The HPDs of the original LHCb detector were replaced with multi-anode photomultiplier tubes (MaPMTs). In RICH 1 and the central region of RICH 2, 1-inch MaPMTs are used. The outer regions of RICH 2 contain 2-inch MaPMTs. The resolution of the Cherenkov angle has improved to 0.81 mrad and 0.52 mrad for RICH 1 and RICH 2 respectively [73].

3.10.4 Calorimeters and muon stations

The calorimeter system is largely unchanged except for two adjustments; the replacement of the front-end electronics to read out at 40 MHz required for the new fully-software trigger, and the removal of SPD and PS layers since the removal of the L0 hardware trigger leaves these redundant. For the same reason the M1 muon station is also removed.

3.10.5 Trigger

The most ambitious challenge for the LHCb Upgrade I is the removal of the L0 hardware trigger and employing a fully-flexible and fully-software trigger system, intended to read out the full detector at the 40 MHz bunch crossing rate [110]. As in Run 1 and Run 2, the high-level trigger consists of two stages. Firstly, HLT1 uses a small number of inclusive lines to reduce the event rate to allow the full reconstruction required by the second stage, HLT2. At HLT2, there exist of the order of 1000 selection algorithms, each tuned for a particular channel or physics analysis. Alongside these selections, real-time alignment and calibration is being performed and fed back to the selection, and retained for offline analysis. The full trigger chain is shown in Figure 3.23.

To efficiently select physics channels of interest, the HLT1 is required to: reconstruct all tracks in the acceptance of the VELO to reconstruct primary vertices, identify tracks as muons or not, reconstruct momenta at the percent level, and provide accurate and a precise covariance matrix for the measured track

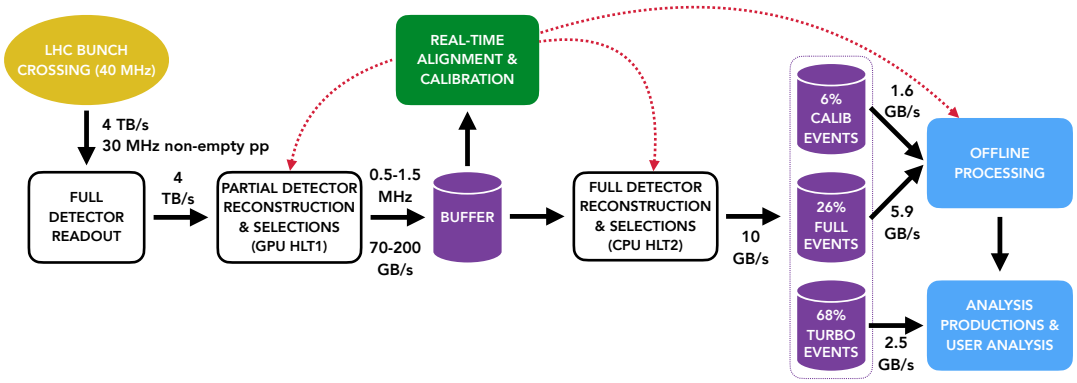

Figure 3.23 *The LHCb trigger chain in Upgrade I. This trigger is fully software. Each stage is shown with their respective data rate [111].*

close to the beamline [73]. This allows for the selection of long-lived particles and τ leptons, and leptons (displaced or not) for use in studies of exotics, hadron spectroscopy and electroweak physics [73].

In HLT2, an offline-quality reconstruction of the event is required, and the $\mathcal{O}(1000)$ selection algorithms decide whether the event should be kept, and importantly what features of the event should be stored. To do this, the HLT2 uses the real-time alignment and calibration information to perform reconstruction. The reconstruction uses four components; charged particle recognition, reconstruction of the calorimeters, particle identification and a Kalman fit of the tracks that have been reconstructed [73]. In the case where multiple HLT2 selection algorithms have chosen to retain an event, the superset of the requested information from each algorithm is recorded. Since only the necessary information is kept, the rate of recorded events can increase and the size of each event is reduced [73].

3.11 Track reconstruction

There are several categories of tracks in LHCb [112] which are shown in Figure 3.24;

- Long track: used for physics analysis, has hits in all tracking stations,
- Downstream track: used for physics analysis of long-lived particles (e.g. K_S^0), has hits in all trackers except the VELO,

- T track: formed from hits only in the T-stations,
- Upstream track: formed from hits in the VELO and TT from a low momentum particle,
- VELO track: formed of hits only in the VELO from a low momentum particle.

Tracks in the VELO are reconstructed first, and these tracks are then used by forward tracking and track matching algorithms to form long tracks [113, 114]. It is possible that a track can be formed of an unrelated collection of hits, known as a ghost track [115]. Ghost tracks typically arise due to a mismatch of VELO tracks and T-station hits. To extract a measurement of the track momentum and reject these fake tracks, reconstructed tracks are passed to a Kalman Filter [103].

The main components used to fit the track are the track state vector, the covariance matrix of the track state parameters, and the transport matrix defining how the track is expected to propagate through the material and interact with the magnetic field. The track state vector is given by

$$\overrightarrow{x} = \begin{pmatrix} x \\ y \\ t_x \\ t_y \\ q/p \end{pmatrix}, \tag{3.2}$$

where $t_{x,y}$ are the slopes of the track at the given z-position,

$$t_x = \frac{\partial x}{\partial z} = \frac{p_x}{p_z} \quad , \quad t_y = \frac{\partial y}{\partial z} = \frac{p_y}{p_z}. \tag{3.3}$$

The covariance matrix is a 5×5 matrix with a row and column for each of the track state parameters. The Kalman filter has two main stages, the prediction stage and the filtering stage. At the prediction stage, the track state k at z_k is used to estimate the track state $k-1$ at z_{k-1}. At the filtering stage, the weighted mean of the predicted and measured track state at z_{k-1} is calculated. Measurements of positions x and y are added sequentially to the fitter, and then the fitter is run in the reverse order to converge on the best track fit. Each track is assigned a value for the probability that the track is a ghost, since the ghost tracks typically have fewer hits and poorer track χ^2 as a result.

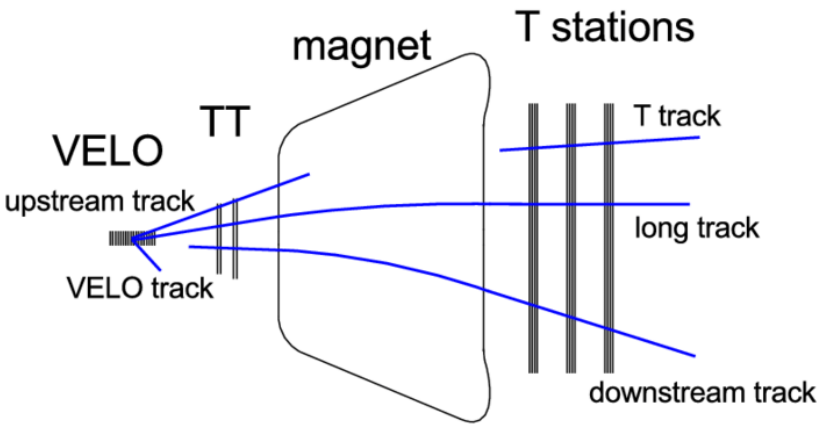

Figure 3.24 *Types of tracks in LHCb. Source: [112]*

3.12 Simulation

The majority of analyses of LHCb data require reliable simulation to model the kinematic properties of certain processes, model detector effects such as detector acceptances, and model specific background contributions. Simulation can be either full Monte Carlo (MC) simulation or fast simulation, for example from RapidSim [116]. The production of full MC begins with the Pythia8 MC generator which simulates the particles produced in the high-energy proton-proton collisions at the LHC [117]. In LHCb, the decays of b-hadrons are simulated using EvtGen [118]. EvtGen is responsible for reproducing the correct angular and decay-time distributions in b-decays, which is particularly crucial in CP-violation analyses. Finally, the particles are propagated through a model of the detector using Geant4 [119]. The momentum scale of the simulation is also calibrated [120]. RapidSim simulation is generated by only generating the decay of interest, with the kinematics of the generated particles obtained by sampling distributions from fixed-order next-to leading-log (FONLL) calculations [116, 121]. The momenta are smeared by user-defined smearing functions, where the model for LHCb defines a Gausssian resolution model with a momentum-dependent width [116], defined using studies of momentum calibration [122, 123].

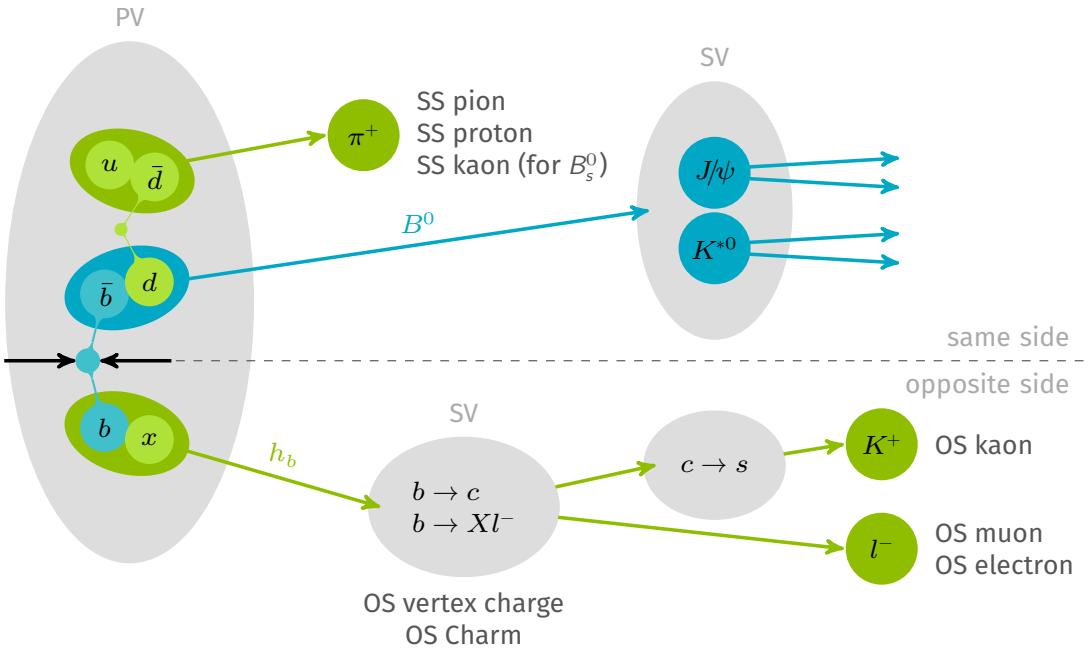

Figure 3.25 *This figure shows the same side (SS) and opposite side (OS) techniques used for flavour tagging. Shown in the context of a neutral B-meson [124].*

3.13 Flavour tagging

A crucial component of many flavour analyses is the ability to separate the neutral mesons into mesons or antimesons. To do this, algorithms are used to 'tag' the flavour of the quarks at the point of their production, known as flavour tagging. There is same side (SS) and opposite side (OS) tagging. The following explanation refers to Fig. 3.25. On the same side, we see a π^+. This consists of $u\bar{d}$. Since this d comes from a $d\bar{d}$ pair we know the B-meson has a d quark, and therefore a $\bar{b}$, so we know this is a B^0. On the opposite side, we see a K^+. Since this contains a s-quark, this could only have come from a down-type quark, in this case the b-quark of the $b\bar{b}$ pair. This shows that it is the $\bar{b}$ that forms the B^0 meson.

Chapter 4

The search for $B^0 \to \phi\phi$ decays

The decay of $B^0 \to \phi\phi$ is not yet observed. As described in Section 2.6, the value of the $B^0 \to \phi\phi$ branching fraction has implications for the underlying physics of the more abundant $B_s^0 \to \phi\phi$ decay, since the leading-order diagrams in $B^0 \to \phi\phi$ are related to the sub-leading contributions to $B_s^0 \to \phi\phi$. The following chapters discuss the analysis performed to search for this decay. This analysis makes use of data collected during Run 1 (2011-2012) and Run 2 (2015-2018) of the LHCb experiment, corresponding to 9 fb^{-1} of data. Both ϕ mesons are reconstructed from two oppositely charged kaons, giving a final state with four charged kaons. The $B^0 \to \phi\phi$ branching fraction is extracted from an extended likelihood fit to the four-kaon invariant mass distribution, where Run 1 and Run 2 data are fitted simultaneously.

The search for this decay is performed relative to the more abundant $B_s^0 \to \phi\phi$ decay mode. This is a convenient choice as the two modes have the same final state and topology, allowing many sources of systematic uncertainty to cancel and giving a ratio of selection efficiencies that is close to unity. The search involves fitting the invariant mass distribution of the selected candidates to the $B^0 \to \phi\phi$ signal shape, the $B_s^0 \to \phi\phi$ normalisation mode shape and the various background contributions. Using this fit to the invariant mass distribution, the limit on the $B^0 \to \phi\phi$ branching fraction is set using the CL$_s$ method [125, 126].

As highlighted in Table 2.2 in Section 2.6, the predicted branching fraction of the $B^0 \to \phi\phi$ decay is at the level of 10^{-8} which makes it more than a factor of 1000 smaller than the $B_s^0 \to \phi\phi$ decay mode. Accounting for the fragmentation ratio, f_s/f_d, which describes how often a B_s^0 is formed over a B^0, the yield of $B^0 \to \phi\phi$

Decay mode	Branching fraction (%)
$D_s^+ \to \phi\pi$	4.5 ± 0.4
$D_s^+ \to \phi\mu^+\nu$	1.9 ± 0.5
$D_s^+ \to \phi e^+\nu$	2.39 ± 0.16
$D_s^+ \to \phi\rho^+$	5.59 ± 0.34
$D_s^+ \to \phi 3\pi$	1.21 ± 0.16

Table 4.1 *Branching fractions for decays of D_s^+ mesons into ϕ mesons.*

to $B_s^0 \to \phi\phi$ events is more than a factor of 460 smaller. A branching fraction at the 10^{-8} level translates to just tens of events in the full Run 1 and Run 2 sample from LHCb. In order to have sensitivity to a possible signal, events need to be well reconstructed with good momentum resolution, and peaking background contributions that mimic $B_s^0 \to \phi\phi$ and $B^0 \to \phi\phi$ events should be removed, retaining as much signal efficiency as possible. Robust models of the four-kaon invariant mass distribution must be developed such that signal decays are not falsified nor incorrectly absorbed into the background models, yet retain enough flexibility to capture variations in the data.

To guard against bias, the $B^0 \to \phi\phi$ signal region, defined as the mass range 5240 MeV/c^2 < $M(K^+K^-K^+K^-)$ < 5320 MeV/c^2, is blinded. Any events with a four-kaon invariant mass in this range are temporarily removed from the data.

4.1 Backgrounds

Several sources of background can contaminate the four-kaon invariant mass spectrum when selecting $B^0_{(s)} \to \phi\phi$ decays. There are two broad categories of backgrounds; combinatorial background and peaking backgrounds. Combinatorial background comes from randomly combined tracks that still satisfy the selection criteria applied by the trigger. One particularly abundant source of combinatorial background comes from the combination of two real ϕ mesons from independent processes. Decays of b-hadrons in the LHC can produce copious numbers of D_s^+ mesons,[1] which have a relatively high branching fraction to the ϕ meson greater than 15% [127]. The branching fractions for the largest contributions of D_s^+ decays to ϕ mesons are shown in Table 4.1. It is possible to tag combinatorial events coming from D_s^+, so that the combinatorial background can be split into two categories: D_s^+-tagged and non-D_s^+-tagged. Once split into

[1]Charge conjugation implied.

these categories, they are treated with multivariate classifiers which are described further in Section 6.3.

An especially challenging background to control comes from the normalisation mode, $B_s^0 \to \phi\phi$. Given the identical final state and near-identical topology to $B^0 \to \phi\phi$, the efficiency of retaining $B_s^0 \to \phi\phi$ is expected to be the same as the $B^0 \to \phi\phi$ efficiency. However, the momentum resolution of LHCb is not perfect and so the $B_s^0 \to \phi\phi$ and $B^0 \to \phi\phi$ peaks have sizeable widths from this momentum resolution. The distributions therefore overlap, reducing sensitivity to $B^0 \to \phi\phi$ decays. Further sensitivity can be achieved by being selective with track quality. To do this, a novel multivariate classifier has been developed to separate $B_s^0 \to \phi\phi$ and $B^0 \to \phi\phi$ decays as much as possible without reducing signal selection efficiency dramatically. This classifier is described in Chapter 5.

After $B_s^0 \to \phi\phi$ events, the next two most prominent peaking backgrounds come from the $\Lambda_b^0 \to pK^-\phi$ decay (with the charge conjugated process implied) and the $B^0 \to \phi K^*(892)$ decay, where one of the final state particles is mis-identified as a kaon and had the incorrect mass associated to the track. In the case of $\Lambda_b^0 \to pK^-\phi$, it is the proton that is mistaken for a kaon. In the case of $B^0 \to \phi K^*(892)$, the $K^*(892)$ decays to a $K\pi$ final state and the pion is mistaken for a kaon. In each of these cases, the key to removing these backgrounds is the use of particle identification variables. For each case, a dedicated veto is developed and applied, with the remaining events modelled and the expected yields estimated. The vetoes are further discussed in Section 6.2, and modelling discussed in Section 7.2. There are also background events coming from partially reconstructed events with excited K^* states, where there are two final state pions – one misidentified and one missed in reconstruction. The background from these partially reconstructed decays is discussed further in Section 7.2.3.

A summary of the main backgrounds can be seen in Figure 4.1. A schematic showing the full workflow is shown in Figure 4.2.

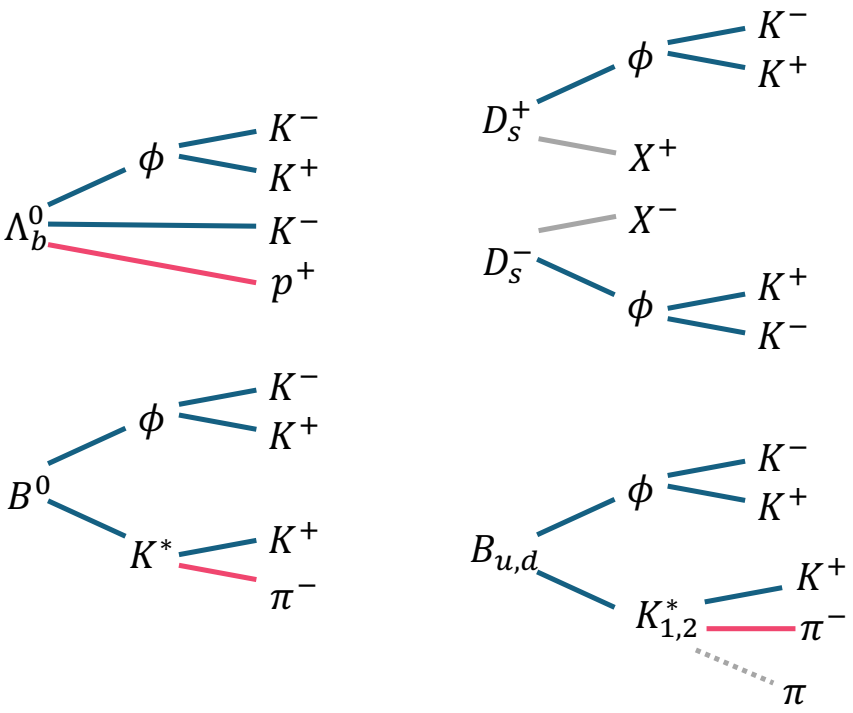

Figure 4.1 *A schematic showing several types of backgrounds that can mimic a $B^0_{(s)} \to \phi\phi$ signal. The solid lines represent reconstructed tracks, with mis-identified tracks shown in pink. The dotted grey line represents a missing track in the partially reconstructed excited K^* background. Solid grey lines in the D_s^+ decays represent tracks that are not used to reconstruct these decays as signal.*

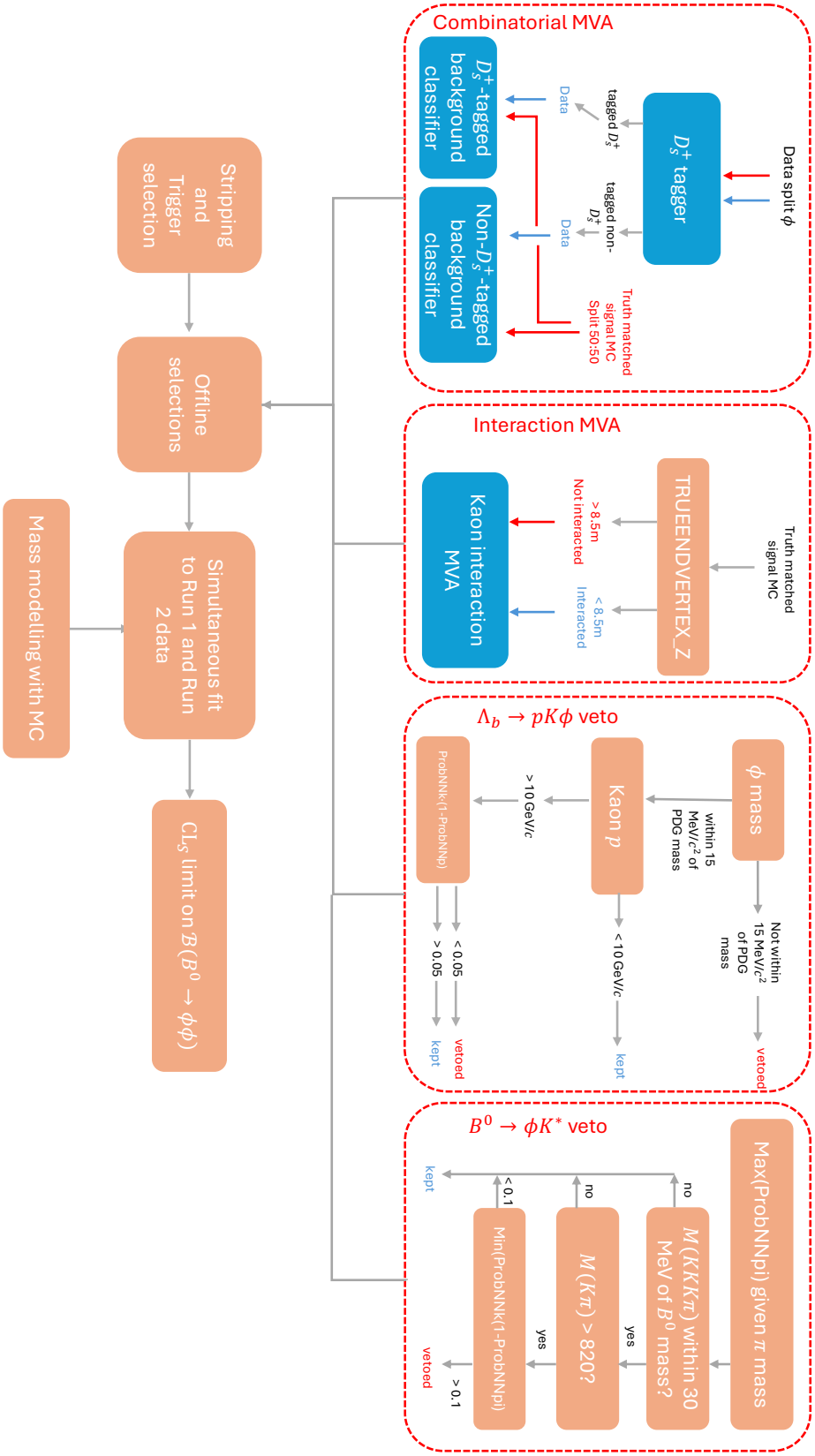

Figure 4.2 *Schematic of the analysis workflow.*

Chapter 5

Multivariate classifier approach to backgrounds from hadronic interactions and decays-in-flight

The resolution of the $B^0_{(s)}$ mass is driven by the quality of the fitted tracks for the four charged kaons in the final state. The track Kalman fit, as described in Section 3.11, assumes a continuous trajectory for the kaons. The hits that are left in the tracking detectors are coupled with the magnetic field transport model to extract the track momentum. In the case that the track has a large kink, for example if the kaon has some hadronic interaction or decays-in-flight, then the track will no longer be roughly smooth. There will be a breakpoint at which the track momentum direction is changed as a result of this interaction, and the track fitter may not properly account for this. These 'kinked' tracks have a poorer momentum resolution, which increases the overlap between the $B^0_s \to \phi\phi$ and $B^0 \to \phi\phi$ peaks. Identifying breakpoints or discontinuities in a track is an established technique for discriminating between muons and hadrons that have decayed-in-flight [128–130].

The technique developed here aims to categorise these tracks into interacted and non-interacted with BDT classifier, trained using the TMVA toolkit [131]. This allows the poor-quality interacted tracks to be removed to improve overall resolution and separation between the B^0_s and B^0 peaks. Decays-in-flight can be identified using muon information. However, many of these decays-in-flight can be missed in the muon identification, since the inner coverage of the muon stations

is smaller than the tracking stations. This approach also will not select hadronic interactions. A combination of muon ID and the developed MVA provides greater control of the $B_s^0 \to \phi\phi$ tail in the $B^0 \to \phi\phi$ mass region.

5.1 Studying the properties of interacted tracks

In order to develop a classifier that will separate tracks into these two categories, a sample of each type of track is required. These are obtained from the simulation. The approximate grouping of tracks into interacted or stable categories is based on the true z-position of the kaon decay vertex point as there is no flag that exists in the simulation that would indicate whether a decay-in-flight or interaction took place.

The threshold z-position for the grouping is determined by arguing that a track is likely to be well reconstructed, regardless of whether it interacts or is stable, providing it has left hits in at least two of the T-stations. For this, the mid-point of the T-stations at $z = 8.5$ m, approximately at the centre of T2, is chosen. Tracks are defined as interacted if their decay vertex lies before 8.5 m. The plots in Figure 5.1 show $B_s^0 \to \phi\phi$ MC simulation for the case where all kaons are stable and where at least one of the kaons has interacted with this criteria. The plots also show the RMS values of each distribution. Worse B_s^0 mass resolution is seen in the case where there is at least one kaon interaction, quantified by a significantly larger RMS value of the distribution. Using this simulation, the fraction of events with interactions is found to be 3% of the total sample and 34% of the $B_s^0 \to \phi\phi$ events in the $B^0 \to \phi\phi$ signal region ($5240\ \text{MeV}/c^2 < M(K^+K^-K^+K^-) < 5320\ \text{MeV}/c^2$). Having a handle on these events is key to reducing the background contribution from $B_s^0 \to \phi\phi$ decays.

5.1.1 Discriminating variables

The multivariate classifier uses several variables to discriminate interacted tracks from stable ones. These variables generally relate to the quality of the result of the track fit, the kinematics of the track, the number of hits that form a track and the probability the track is a ghost track. The LHCb Kalman filter algorithm [132] allows to calculate the χ^2 for segments of tracks up to some break point. This

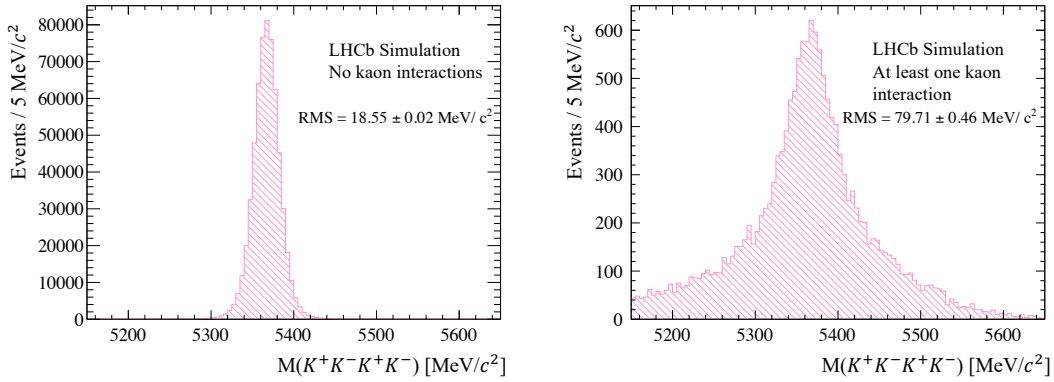

Figure 5.1 *The four-kaon invariant mass distributions are shown for truth-matched signal simulation events containing stable kaons only (left) or at least one interacted kaon track (right) where a stable kaon is defined as one with a decay vertex position greater than 8.5 m from the origin of the LHCb coordinate system.*

allows one to calculate

$$\chi^2_{\text{match}} = \chi^2_{\text{track}} - \chi^2_{\text{upstream}} - \chi^2_{\text{downstream}} \tag{5.1}$$

which will follow a χ^2 distribution with 5 degrees of freedom for real tracks. This is the variable `TRACK_MatchCHI2`. Table 5.1 lists all variables used in the classifier and their definitions. This final list of variables is obtained following several iterations of the classifier where the most important features that are reasonably described by simulation are persisted.

The distributions for these variables are shown in Figure 5.2. The signal sample, shown in solid blue, is truth-matched MC simulation for which the kaon has a decay vertex with $z > 8.5$ m from the origin of the LHCb coordinate system and is therefore defined as stable. The rest of the tracks (those that have an interaction) are assigned to the background sample, shown in hatched red. Clear discrimination is seen between interacted and stable tracks for these selected variables. The linear correlations between the variables in the signal and background samples are shown in Figure 5.3

5.2 Validation with $B^+ \to J/\psi\ K^+$ decays

Since this classifier is trained purely on simulation, the variables are checked for agreement with data and corrected if needed. For the validation studies, the

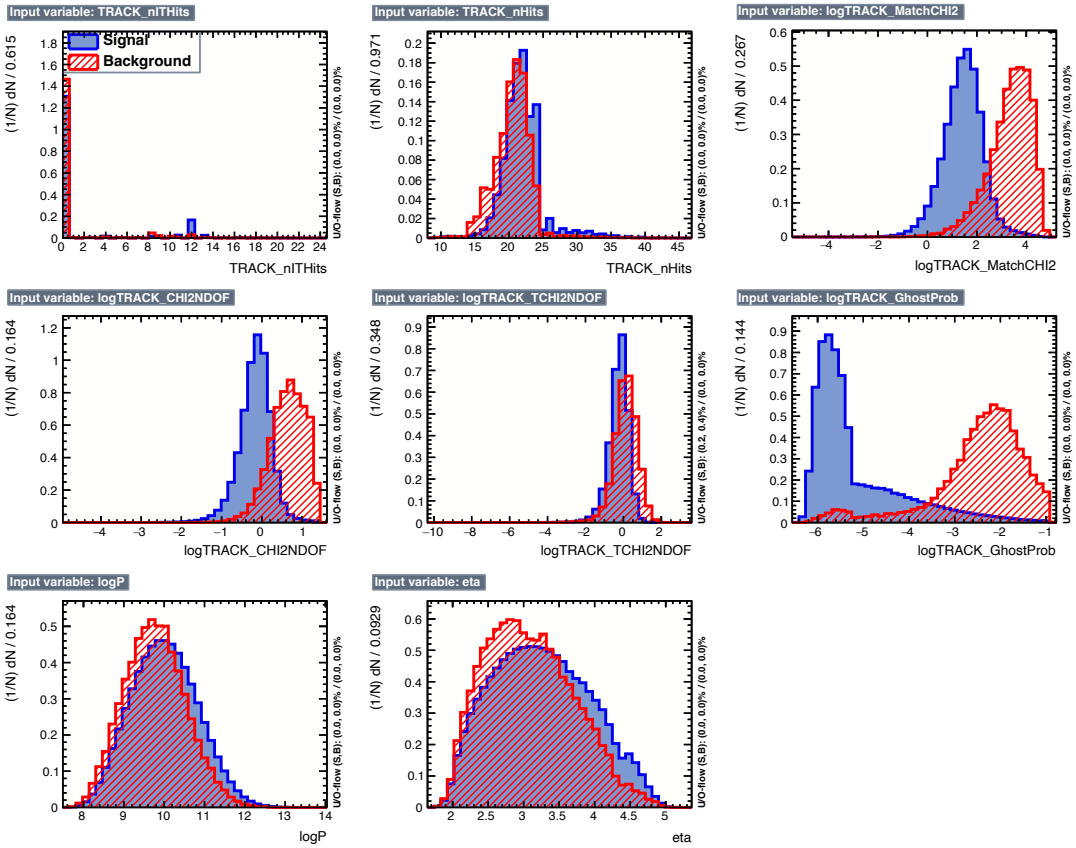

Figure 5.2 *Distributions of input variables used in the kaon interaction MVA, shown for signal and background. Signal events, stable kaons, are shown in solid blue; background events, interacted kaons, are shown in hatched red. The plots are made with tuned Run 2 $B_s^0 \to \phi\phi$ simulation.*

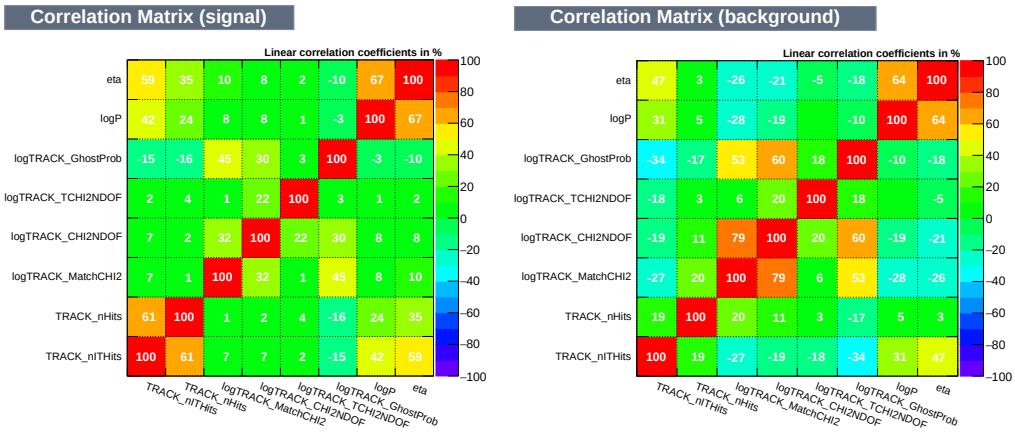

Figure 5.3 *Linear correlations of the discriminating variables used in the kaon interaction MVA. Shown for the signal sample (left) and background sample (right).*

Variable name	Description
logTRACK_MatchCHI2	Log of the χ^2 of the breakpoint between upstream and downstream segments
logTRACK_CHI2NDOF	Log of the track fit χ^2 per degree of freedom
logTRACK_TCHI2NDOF	Log of the track fit χ^2 per degree of freedom in the T region
logTRACK_GhostProb	Log of the probability that the track is a ghost as defined in Section 3.11
logP	Log of the track momentum
logeta	Log of the track η at production
TRACK_nITHits	The number of hits in the IT
2TRACK_nITHits + TRACK_nOTHits	Weighted sum of IT and OT hits (2× IT hits + OT hits)
TRACK_Likelihood	Track likelihood method described in [115]

Table 5.1 *Table of variables used in kaon decay-in-flight and hadronic interaction MVA training. The* TRACK_Likelihood *variable was only available in Run 1.*

mode $B^+ \to J/\psi K^+$ is used, where the J/ψ is reconstructed from a dimuon pair. This mode is chosen for validation as the final state contains a pair of muons and a charged kaon. Muons are stable within the volume of the detector and do not typically interact or decay until the muon stations. Therefore, they should not display any behaviour of interactions and the classifier should not identify a background component in the sample of muon tracks. For the charged kaon track, the behaviour of the classifier should resemble that of the kaons in $B_s^0 \to \phi\phi$. Since the muon tracks do not display the relevant interaction behaviour, the input variables can be tuned by studying the comparisons between data and simulated muon tracks.

These studies are performed with data taken during 2012 and 2016, and corresponding samples of $B^+ \to J/\psi K^+$ simulation. The data is signal weighted using the Custom Orthogonal Weights (COWs) procedure which is able to account for correlations between the discriminating and control variable [133]. The fit to data that is used to extract the signal weights for 2016 is shown in Figure 5.4. The model used to describe the $B^+ \to J/\psi K^+$ signal is the sum of a wide Gaussian and a double-sided Crystal Ball function [134], with the background modelled by an exponential.

The signal-weighted data is compared to simulation to understand the agreement of the variables used in the classifier. The comparisons for a muon track are

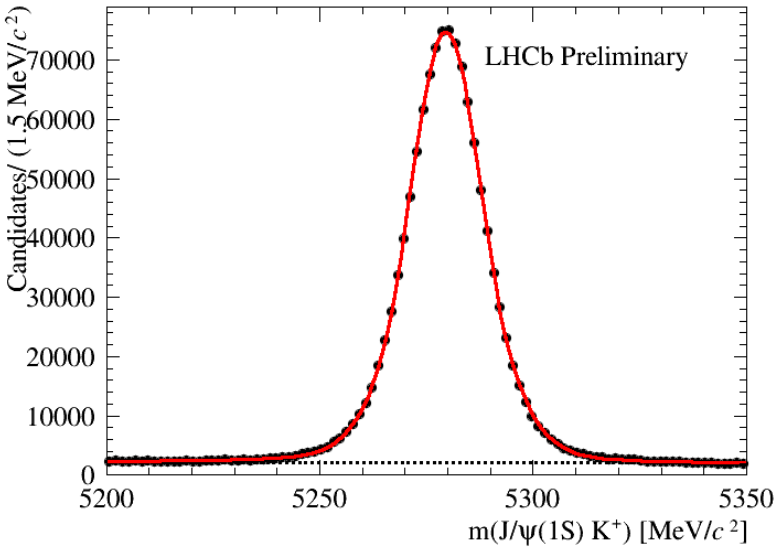

Figure 5.4 *Invariant mass distribution for selected $B^+ \to J/\psi K^+$ candidates in the 2016 dataset. The fit used to extract signal weights is superimposed.*

Variable	Tuning in Run 1	Tuning in Run 2
`TRACK_MatchCHI2`	$\times 1.12$	$\times 1.05$
`TRACK_CHI2NDOF`	Gaussian smear $(0, 0.15)$	Gaussian smear $(-0.15, 0.15)$
`TRACK_TCHI2NDOF`	Gaussian smear $(0.1, 0.2)$	Gaussian smear $(-0.15, 0.1)$
`TRACK_Likelihood`	Gaussian smear $(-0.25, 0.75)$	-
`TRACK_GhostProb`	$\times 1.5$	-

Table 5.2 *Tuning applied to variables to give better agreement in data and MC. For Gaussian smearing, the first number inside the brackets is the mean of the Gaussian and the second is the width.*

shown in Figure 5.5. The data is represented by the black points, with simulation shown in solid yellow. To improve agreement between data and simulation, the MC has been tuned to better match the distribution seen in data using an ad-hoc method to choose appropriate scalings. These can be seen in Figure 5.6. A similar series of plots are made for Run 1, using 2012 $B^+ \to J/\psi K^+$ data and MC. The distributions before tuning applied are shown in Figure 5.7, and the distributions after tuning is applied are shown in Figure 5.8. The tuning applied to the variables in both Run 1 and Run 2 is summarised in Table 5.2. Any remaining discrepancy between the data and simulation in the discriminating variables is not relevant since the classifier response has good agreement which is discussed further in Section 5.3.

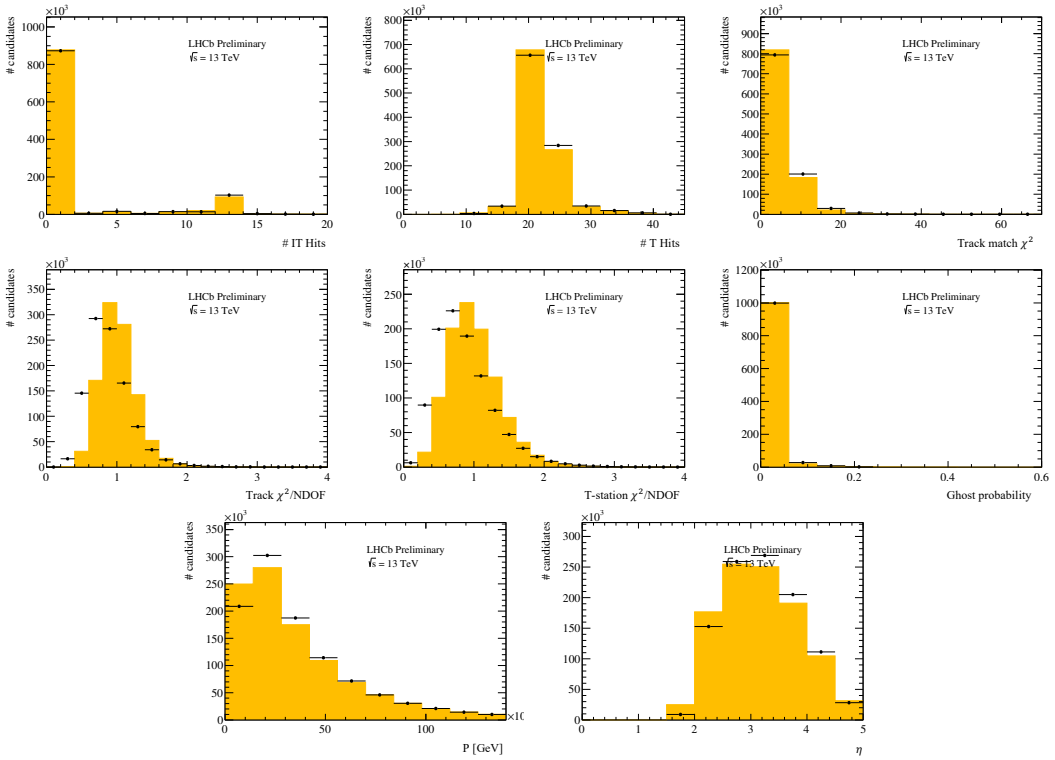

Figure 5.5 *Input variables, prior to tuning, for the kaon interaction BDT shown for a 2016 $B^+ \to J/\psi K^+$ muon. The solid yellow histogram shows truth matched MC, and the black markers show data weighted using COWs to extract signal. From top left to bottom right, these are; the number of IT hits, the number of T-station hits, track match χ^2, track χ^2 per number of degrees of freedom, T-station χ^2 per number of degrees of freedom, ghost probability, track momentum and pseudorapidity.*

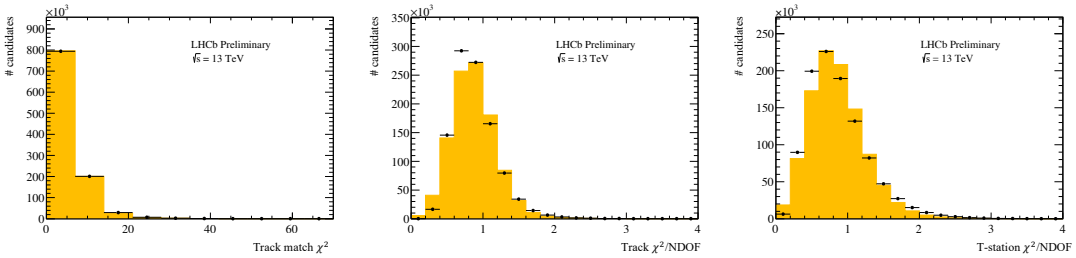

Figure 5.6 *Tuned input variables for the kaon interaction BDT shown for a 2016 $B^+ \to J/\psi K^+$ muon. The solid yellow histogram shows truth matched MC, and the black markers show data weighted using COWs to extract signal. From left to right, these are; track match χ^2, track χ^2 per number of degrees of freedom and T-station χ^2 per number of degrees of freedom.*

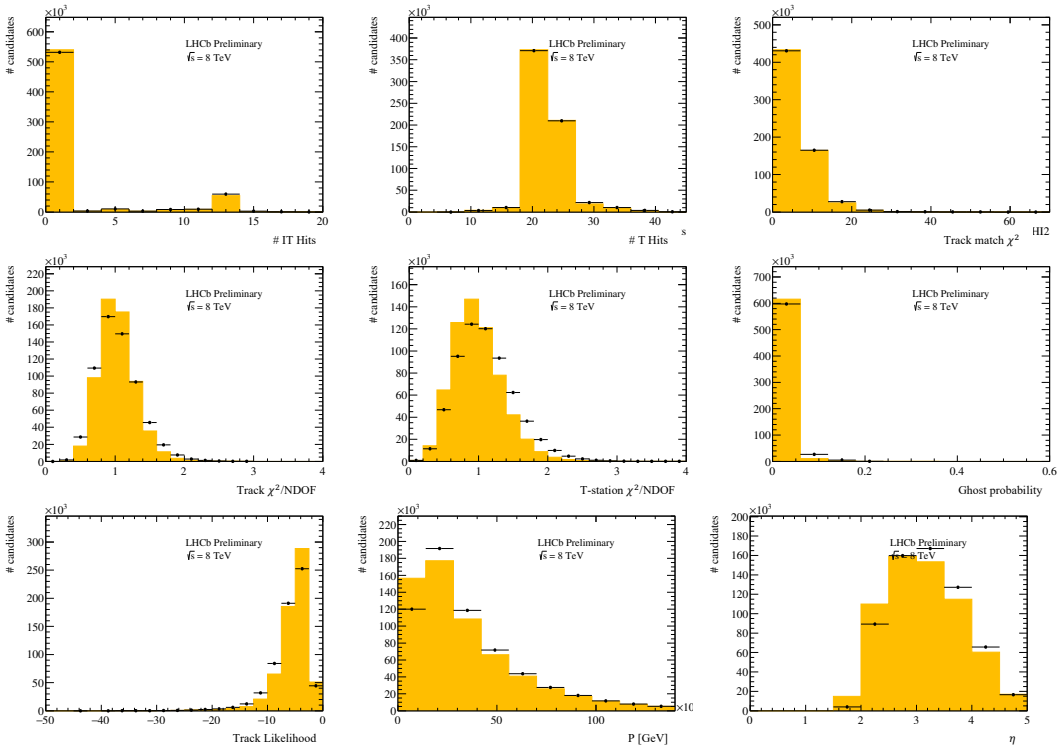

Figure 5.7 *Input variables for the kaon interaction BDT shown for a 2012 $B^+ \to J/\psi K^+$ muon. The solid yellow histogram shows truth matched MC, and the black markers show data weighted using COWs to extract signal. From top left to bottom right, these are; the number of IT hits, the number of T-station hits, track match χ^2, track χ^2 per number of degrees of freedom, T-station χ^2 per number of degrees of freedom, ghost probability, track likelihood, track momentum and pseudorapidity. No tuning is applied.*

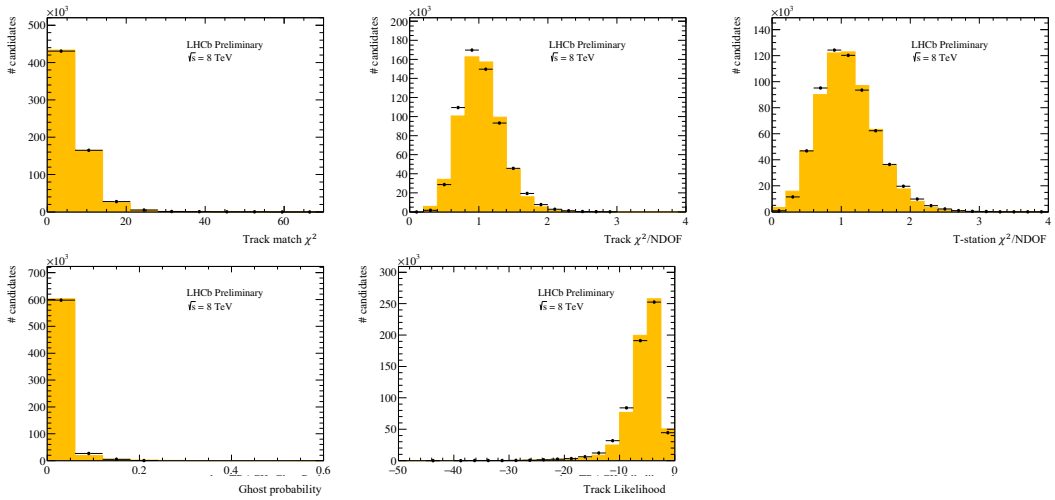

Figure 5.8 *Tuned input variables for the kaon interaction BDT shown for a 2012 $B^+ \to J/\psi K^+$ muon. The solid yellow histogram shows truth matched MC, and the black markers show data weighted using COWs to extract signal. From top left to bottom right, these are; track match χ^2, track χ^2 per number of degrees of freedom, T-station χ^2 per number of degrees of freedom, ghost probability and track likelihood.*

5.3 Classifier performance

The classifier chosen to discriminate between the interacted and stable tracks is a gradient-boosted Boosted Decision Tree (BDTG) trained using the TMVA package [131]. The classifier is trained using the kaons from MC simulation, tuned according to $B^+ \to J/\psi K^+$ data MC comparisons. The tracks are tagged as interacted or stable using the procedure described in Section 5.1 and each category is further split randomly into a sample for training and a sample for testing.

The performance of the classifier is evaluated using two criteria. The ROC curve shows the signal efficiency of a series of working points and their corresponding background rejection factor. Secondly, the classifier output distribution shows the response of the classifier on the testing and training samples which is used to evaluate if the classifier achieves good separation between signal and background and also can show if the classifier is overtrained. The classifier output also show values from a Kolmogorov-Smirnov (KS) test [135]. These numbers represent how likely the testing and training sets are to have originated from the same distribution. That is, the closer the KS test value is to 1, the better the agreement

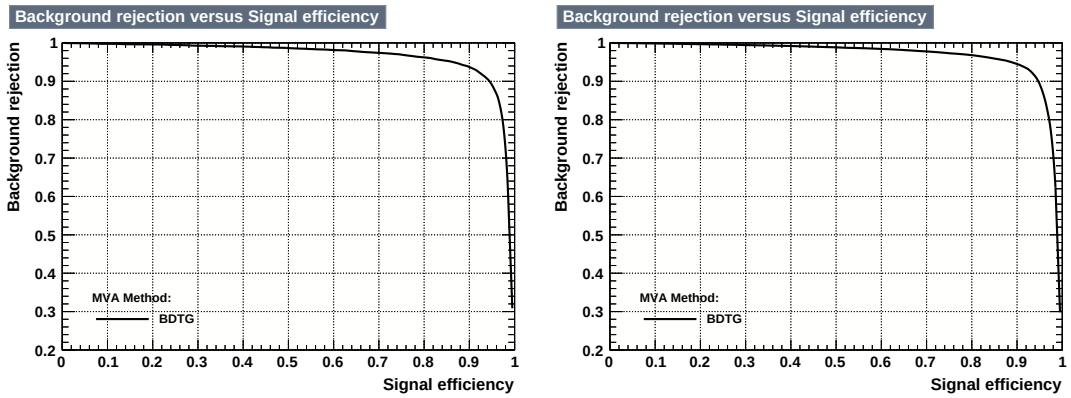

Figure 5.9 *The ROC curves for each classifier is shown. This shows the signal efficiency versus the background rejection for each track. Run 1 is shown on the left, and Run 2 on the right.*

between the testing and training samples. This number is used to quantify the potential overtraining of a classifier.

The ROC curves for Run 1 and Run 2 are shown in Figure 5.9. These show a consistent performance in both Run 1 and Run 2. Since these classifiers are trained on individual tracks, the efficiencies shown here are per-track efficiencies. The working point is chosen to have a per-track efficiency of 95%, which gives a background rejection of 89% in both Run 1 and Run 2. This corresponds to a cut on the classifier output at -0.4 for each kaon track.

The classifier output distributions are shown in Figure 5.10 for each data-taking period. These show the signal and background samples used to train the classifier, and also those used to test the classifier output. The separation between the signal and background shows how well the classifier is able to distinguish between stable and interacted tracks. The agreement between the testing and training samples is used to highlight if the classifier is overtrained. The good agreement between the testing and training samples shows that the classifier is not overtrained.

The comparison of the classifier output between data and simulation in $B^+ \to J/\psi K^+$ decays is shown for Run 2 in Figure 5.11. This figure displays the expected behaviour: that the muons should return a classifier response consistent with signal only. This figure also shows that the agreement between the data and the MC is reasonable, particularly at values below zero. This is particularly important since optimal cut point is at -0.4, as discussed further in Section 6.4.

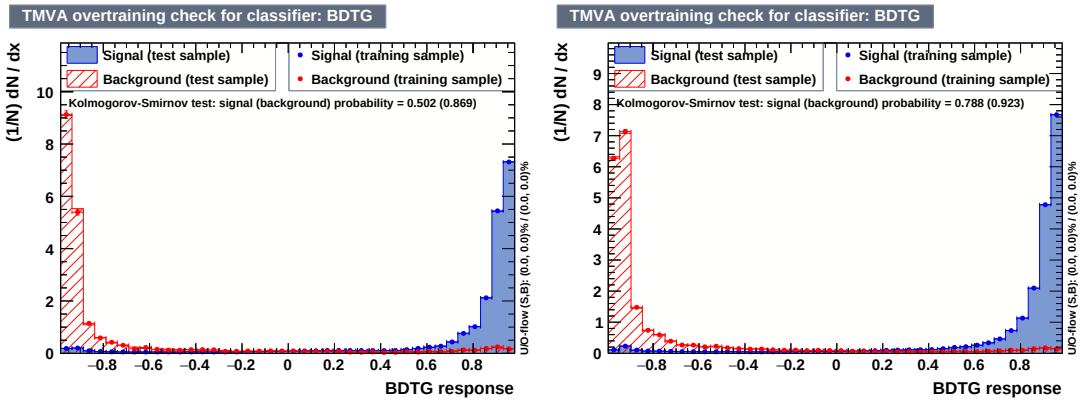

Figure 5.10 *The response of each classifier on testing and training samples for signal and background. The testing samples are shown with shaded histograms, and training samples are shown with circular markers. The red distributions are the background samples, formed of interacted kaons. The blue distributions are signal samples, formed of uninteracted kaons. Run 1 is shown on the left, and Run 2 on the right.*

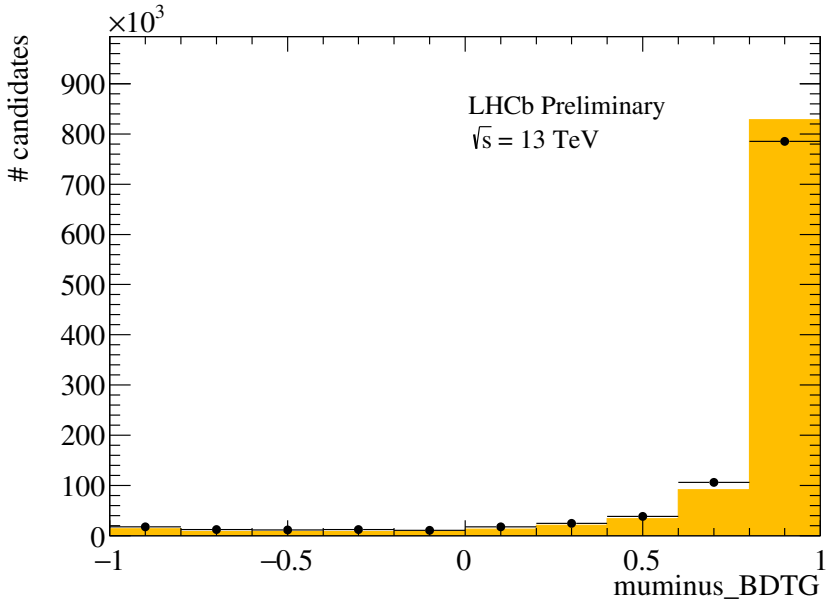

Figure 5.11 *The classifier response on a muon in data (black points) and MC (yellow) after training samples are tuned, shown for 2016 $B^+ \to J/\psi K^+$ data and MC.*

Chapter 6

Dataset and selection

The dataset used for this analysis is the full Run 1 and Run 2 dataset from LHCb, taken between 2011 - 2012 and 2015 - 2018 respectively. Data taken during Run 1 was collected with centre-of-mass energies of 7 and 8 TeV, with Run 2 data collected at 13 TeV. To select $B^0_{(s)} \to \phi\phi$ candidates, a specific set of trigger lines are used. The trigger selection is described in Section 6.1. Following this, events selected by the trigger are centrally streamed, known as 'stripping', and a loose preselection is applied in the data tupling process. Background from the decays $\Lambda^0_b \to pK^-\phi$ and $B^0 \to \phi K^*(892)$ are treated with dedicated vetoes, described in Section 6.2. A two-stage multivariate classifier is deployed to remove combinatorial background (Section 6.3). A further multivariate classifier is trained to remove background from poorly reconstructed $B^0_s \to \phi\phi$ decays with interactions or kaon decays-in-flight, as described in the previous chapter.

6.1 Trigger, stripping and preselection

The full sequence of triggering, stripping and preselecting events is shown in Figure 6.1. Each stage is described in turn.

6.1.1 Trigger selection

The specific trigger lines used to select $B^0_{(s)} \to \phi\phi$ candidates are shown in Table 6.1. Candidates are categorised as being triggered on signal (TOS) or

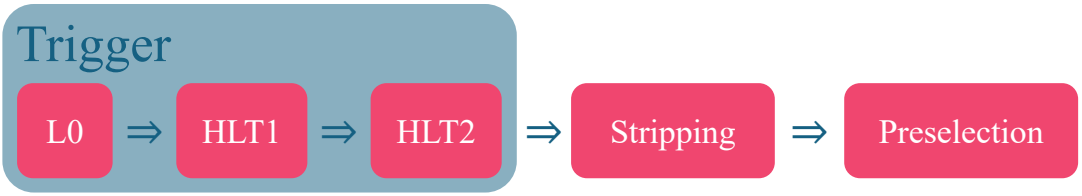

Figure 6.1 *The sequence of trigger, stripping and preselection.*

Level	Run 1
L0	`L0Hadron_TOS` or `L0Global_TIS`
HLT1	`Hlt1TrackAllL0_TOS`
HLT2	`HLT2Topo3BodyBBDT_TOS`
	`HLT2Topo4BodyBBDT_TOS` or `HLT2IncPhi_TOS` or
	Run 2
L0	`L0Hadron_TOS` or `L0Global_TIS`
HLT1	`Hlt1TwoTrackMVA_TOS` or `Hlt1TrackMVA_TOS`
HLT2	`Hlt2Topo2Body_TOS` or `Hlt2Topo3Body_TOS` or
	`Hlt2Topo4Body_TOS` or `Hlt2PhiIncPhi_TOS`

Table 6.1 *Trigger lines used to select* $B^0_{(s)} \to \phi\phi$ *candidates.*

triggered independently of signal (TIS). For the latter category, other parts of the event were responsible for triggering the candidate. At the L0, it is required that either the hadron L0 line triggered due to the candidate event or the global L0 line triggered independently of the signal. Due to the different requirements for the events that are TIS, the kinematics of the TIS-only events are slightly different to that of TOS events. This is taken into consideration when training the combinatorial MVA, described in Section 6.3. For all the HLT1 and HLT2 lines used in this analysis, the candidate must have triggered on signal.

At L0, the candidates selected are those with high transverse momentum in the muon system or high transverse energy in the calorimeters [136]. As discussed in Section 3.9, there are dedicated lines, for example, for hadron candidates or muon candidates. In this analysis, candidate events are required to pass the global L0 requirement independently of the candidate signal, or required to have passed the hadronic line on signal. This imposes a restriction to select only high p_T tracks. TOS decisions are required on the HLT1 track lines given in Table 6.1, which require high p_T displaced tracks, either a single track or pair of tracks, to be selected. At HLT2, TOS decisions are required on the topological triggers or an additional trigger line to select events including at least one ϕ meson. The topological lines (`Hlt2Topo(2,3,4)Body_TOS`) look for 2, 3, or 4 tracks that are consistent with being from a heavy flavour hadron, and the ϕ line

(Hlt2PhiIncPhi_TOS) looks for a displaced, high p_T ϕ meson.

6.1.2 Stripping selection

Following to the trigger requirements, offline data is required to pass a dedicated $B_s^0 \to \phi\phi$ stripping line. The stripping introduces loose selection criteria on the candidate events. At this stage, well-identified kaons are combined to form the ϕ mesons. To be considered well-identified, a kaon is required to have a value of ProbNNk greater than 0.02[1], a transverse momentum greater than 400 MeV/c and the fit to the primary vertex must converge. Each ϕ candidate must then have a mass within 25 MeV/c^2 of the nominal ϕ mass, and the product of their transverse momenta must be greater than 1.2 GeV$^2/c^2$. For the B candidate, the mass must be within 300 MeV/c^2 of the known B_s^0 mass. Finally, the angle between the line that joins the primary and secondary vertices and the B candidate momentum vector is calculated. The cosine of this angle, known as the DIRA, is required to be greater than 0.999.

6.1.3 Preselection

When creating tuples, the data and simulation is loosely preselected with the following requirements. To reduce combinatorial background, the decay time must be in the range $0.3 - 14$ ps and the maximum DOCA of the B candidate must be less than 50 mm. This selection on the maximum DOCA is chosen to be loose due to the poor precision of the ϕ vertices. The vertex is fitted with a primary vertex constraint using the DecayTreeFitter package [137]. The decay tree fit is required to converge with a χ^2 per degree of freedom less than 5. The value of the PID variable ProbNNpi must be smaller than 0.9 to veto pion backgrounds. The PID selection is further studied and tightened in the optimisation procedure described in Section 6.4. A selection is also made on the error associated with the B-meson mass value at a value of 20 MeV/c^2. The distribution of the B-meson mass error is shown on the left of Figure 6.2. Using this distribution, 1 million B-meson mass measurements can be sampled from the pull distribution to produce the plots in the right of Figure 6.2. In this figure, the B_s^0 and B^0 peaks can be seen where the $B^0 \to \phi\phi$ yield is scaled to a branching

[1]This requirement is is more than 97% efficient at retaining kaon tracks, and removes more than 70% of pion tracks.

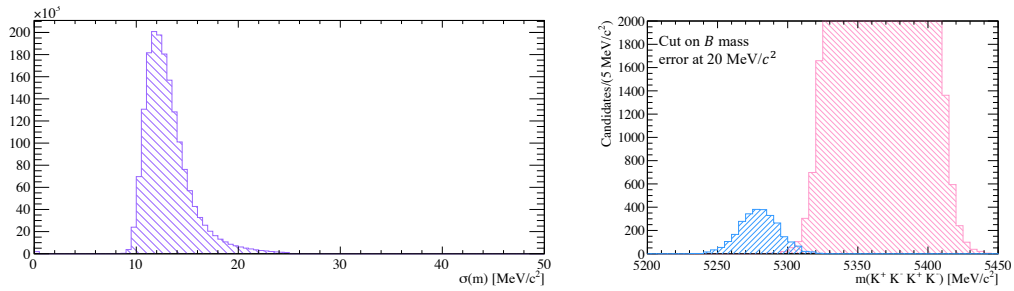

Figure 6.2 *The plot on the left shows the distribution of error values associated to the B meson mass, with the plot on the right showing distributions of the B meson masses resampled from the B meson mass error.*

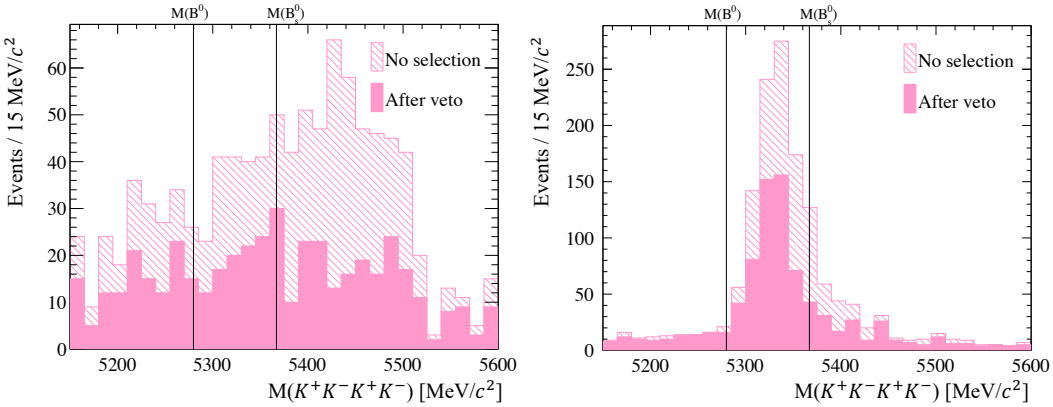

Figure 6.3 *The peaking backgrounds in the $B^0 \to \phi\phi$ search shown before and after applying selection. Plots are made using simulation, with $\Lambda_b^0 \to pK^-\phi$ on the left and $B^0 \to \phi K^*(892)$ on the right.*

fraction of 1.2×10^{-8}. The plots show the B_s^0 meson mass error and the separation achieved applying a cut at 20 MeV/c^2.

6.2 Veto of peaking backgrounds

The decays $\Lambda_b^0 \to pK^-\phi$ and $B^0 \to \phi K^*(892)$ are sources of peaking background that survive the trigger and stripping selections. To suppress these, specific vetoes are developed. Simulated samples of the peaking backgrounds are shown in Figure 6.3 before and after the veto is applied, with $\Lambda_b^0 \to pK^-\phi$ on the left and $B^0 \to \phi K^*(892)$ on the right. The vetoes developed for each of these backgrounds is described in the following subsections.

6.2.1 $\Lambda_b^0 \to pK^-\phi$ veto

The $\Lambda_b^0 \to pK^-\phi$ decay can mimic the signal if the proton in the final state is misidentified as a kaon. A requirement is made on the reconstructed ϕ meson mass that it must be within 15 MeV/c^2 of the known value. For the events surviving this ϕ meson mass window requirement, particle identification is applied. Particles with $p < 10$ GeV/c are below the RICH proton threshold and are not removed as there is no proton-kaon discrimination. However, if an event has a track with a momentum greater than 10 GeV/c above the RICH proton threshold, a tight cut is applied on the track PID. The cut is placed on the combination $\texttt{ProbNNk} \times (1 - \texttt{ProbNNp})$ at 0.05 for these high momentum tracks. This selection removes 53% of the background from $\Lambda_b^0 \to pK^-\phi$ with an efficiency of 95% on signal MC.

6.2.2 $B^0 \to \phi K^*(892)$ veto

The $B^0 \to \phi K^*(892)$ decay mimics the signal mode if the pion from the decay of K^* is misidentified as a kaon. The track with the largest value of `ProbNNpi` is assigned the pion mass. With the substituted pion mass, the $KKK\pi$ and the $K\pi$ invariant masses are calculated. If $M(KKK\pi)$ is within 30 MeV/c^2 of the nominal B^0 mass or $M(K\pi)$ is within 70 MeV/c^2 of the nominal $K^*(892)$ mass then the particle identification is tightened to $\min(\texttt{ProbNNK} \times (1 - \texttt{ProbNNpi})) < 0.1$. This veto removes 30% of $B^0 \to \phi K^*(892)$ background with an efficiency of selecting $B_s^0 \to \phi\phi(B^0 \to \phi\phi)$ of 96%(99%).

6.3 MVA for combinatorial background

To reduce combinatorial background, a two-stage approach is adopted. As described in Section 4.1, the combinatorial background can come from two main sources, tagged as D_s^+ or non-D_s^+. Since the background from D_s^+ mesons will have different properties than more general combinatorial background, a classifier is trained specifically for D_s^+ backgrounds and a further, more general classifier is trained to act on the remaining combinatorial. In order to classify events as having come from D_s^+ decays or not, an algorithm to tag background events coming from D_s^+ decays is developed. The algorithm designed to tag candidates

	Selection applied		
Variable	π	μ	e
`ProbNNpi`	> 0.3	–	< 0.9
`ProbNNK`	< 0.5	< 0.9	–
`ProbNNmu`	–	> 0.2	–
`ProbNNe`	–	–	> 0.9
`TRGHOSTPROB`	–	< 0.1	–
p_T	$> 400\text{MeV}/c^2$	$> 400\text{MeV}/c^2$	$> 400\text{MeV}/c^2$
χ^2_{IP}	> 9	> 9	> 9

Table 6.2 *Selections on π^+, μ^+ and e^+ that are vertexed with the ϕ meson.*

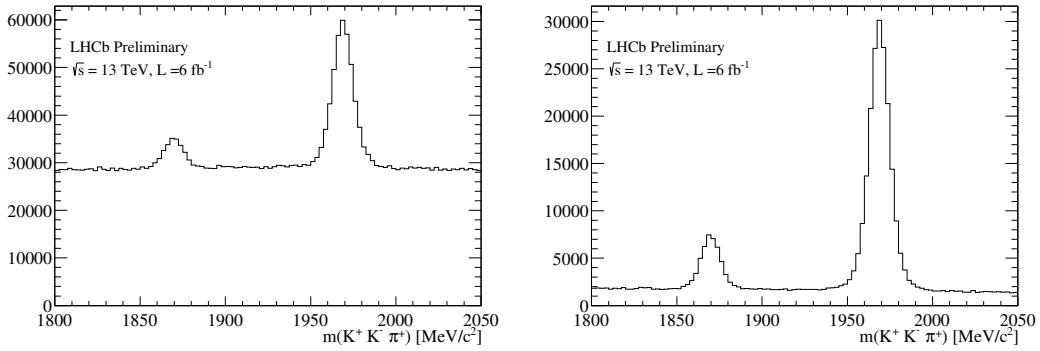

Figure 6.4 *$KK\pi$ invariant mass spectrum for candidates made by combining selected ϕ candidates from $B^0_s \to \phi\phi$ data sample with a displaced pion candidate. Loose cuts are applied to the plot on the left and a cut on the trained BDT is shown the right.*

is described in Section 6.3.1. The first-stage classifier for removing D_s^+-tagged background is described in Section 6.3.2, and the second-stage classifier for removing remaining non-D_s^+-tagged background is described in Section 6.3.2.

6.3.1 D_s^+ tagger

In order to train the MVA to remove background from D_s^+ decays, a D_s^+-tagger is developed. Firstly, the ϕ meson candidates from the stripping selection are split and each vertexed with a displaced track, either an electron, muon or pion. The criteria for selecting each of these is shown in Table 6.2. In the $\phi\pi^+$ invariant mass spectrum shown on the left of Figure 6.4, D_s^+ peaks are clearly seen.

In order to cleanly select D_s^+ candidates,[2] BDTG classifiers are trained using TMVA [131]. A total of four classifiers are trained. There is a classifier for

[2]Charge conjugation implied.

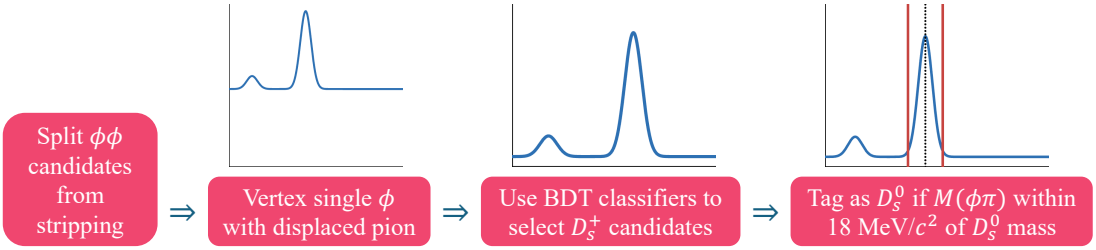

Figure 6.5 *Full sequence of tagging D_s^+ candidates.*

hadronic D_s^+ decays where a ϕ meson can be combined with a displaced pion, $D_s^+ \to \phi\pi^+$, and for semileptonic D_s^+ decays, $D_s^+ \to \phi l^+\nu$ where $l = e, \mu$. These classifiers are trained separately for Run 1 and Run 2 data. These classifiers are trained on data where the individual ϕ candidates are vertexed with a displaced pion. The signal proxy is the signal weighted data, where s-weights have been determined from a fit to the D_s^+ mass [138]. For the semi-leptonic decays, due to the missed neutrino, the D_s^+ peak is not well reconstructed. In this case, the MVA is trained on a subset of the variables used in the $D_s^+ \to \phi\pi^+$ tagger, using the same input data. The input variable distributions are detailed in Appendix D. Figure 6.4, shows the $\phi\pi$ invariant mass following this selection. Most tagged events arise from the π^+ tagger with a rate of 64%, followed by the μ^+ tagger with a rate of 23%. There is a small mistag rate, around 0.3%, which likely comes from $B_c^+ \to B_s^0\pi^+$ events.

Tagged D_s^+ candidates are chosen as those passing the BDTG classifier criteria, shown in the right of Figure 6.4, that have a $\phi\pi$ mass within 18 MeV/c^2 of the known D_s^+ mass. The D_s^+ tag is applied in two ways. Firstly, it can be used on data to effectively veto obvious D_s^+ events. Secondly, D_s^+ tagged data is used to train the MVAs to capture the background the tagger did not identify, for example non-D_s^+ combinatorial background or D_s^+ decays where the missing track was not reconstructed. The full sequence of tagging D_s^+ candidates is summarised in Figure 6.5.

6.3.2 Two-stage combinatorial background classifier

First stage targetting D_s^+-tagged background

The classifier trained to target D_s^+-tagged background is a multilayer perceptron (MLP) trained with TMVA [131], with hyperparameters of the classifier

Variable	Description
`dira`	Log. of the pointing angle
`doca12`	Log. of the ϕ meson DOCA
B-meson η	Pseudorapidity of the B candidate
`ConeIT`	Transverse isolation of the B for cone size of 1.8
DTF χ^2	The χ^2 per degree of freedom of the decay tree fit
ϕ-meson χ^2_{IP}	The impact parameter χ^2 of the ϕ meson
`DChi2TwoTrack`	Log. of the two track $\Delta\chi^2$ isolation variable
`DChi2OneTrack`	Log. of the one track $\Delta\chi^2$ isolation variable

Table 6.3 *Input variable descriptions for the combinatorial background MLP classifier.*

taken from previous studies. The classifier is trained using truth-matched signal MC and data sidebands that are tagged as coming from D_s^+ decays. Background sidebands are defined as $M(K^+K^-K^+K^-) < 5240$ MeV/c^2 or $M(K^+K^-K^+K^-) > 5400$ MeV/c^2. The data and MC have the loose preselection applied as described in Section 6.1.3. The discriminating variables chosen relate to the quality of the vertex reconstruction and signal isolation, reflecting the nature of their background. These variables were chosen using an iterative procedure and their definitions are detailed in Table 6.3. The cone isolation variable, `ConeIT`, is calculated by studying all track objects within a cone defined around the candidate signal event. The cone has a size defined as

$$r = \sqrt{\Delta\phi^2 + \Delta\eta^2} = 1.8 \tag{6.1}$$

where ϕ and η are the usual azimuthal angle and psuedorapidity of the B-meson track candidate. The vertex isolation variables are calculated by taking the vertexed particle and adding further tracks from the event and creating a new vertex. The distributions of all discriminating variables in signal and in background are shown in Figure 6.6. The input variables agree in signal-weighted data and MC, discussed in Appendix B.1

The performance of this classifier is shown for Run 2 data and MC in Figure 6.7. These plots show a good separation between signal and background and no evidence of overtraining as quantified by the KS test values of 0.98 and 0.45 for signal and background respectively. The ROC curve shows good signal efficiency is achieved with a sizeable background rejection. The chosen working point for this classifier is discussed further in Section 6.4.

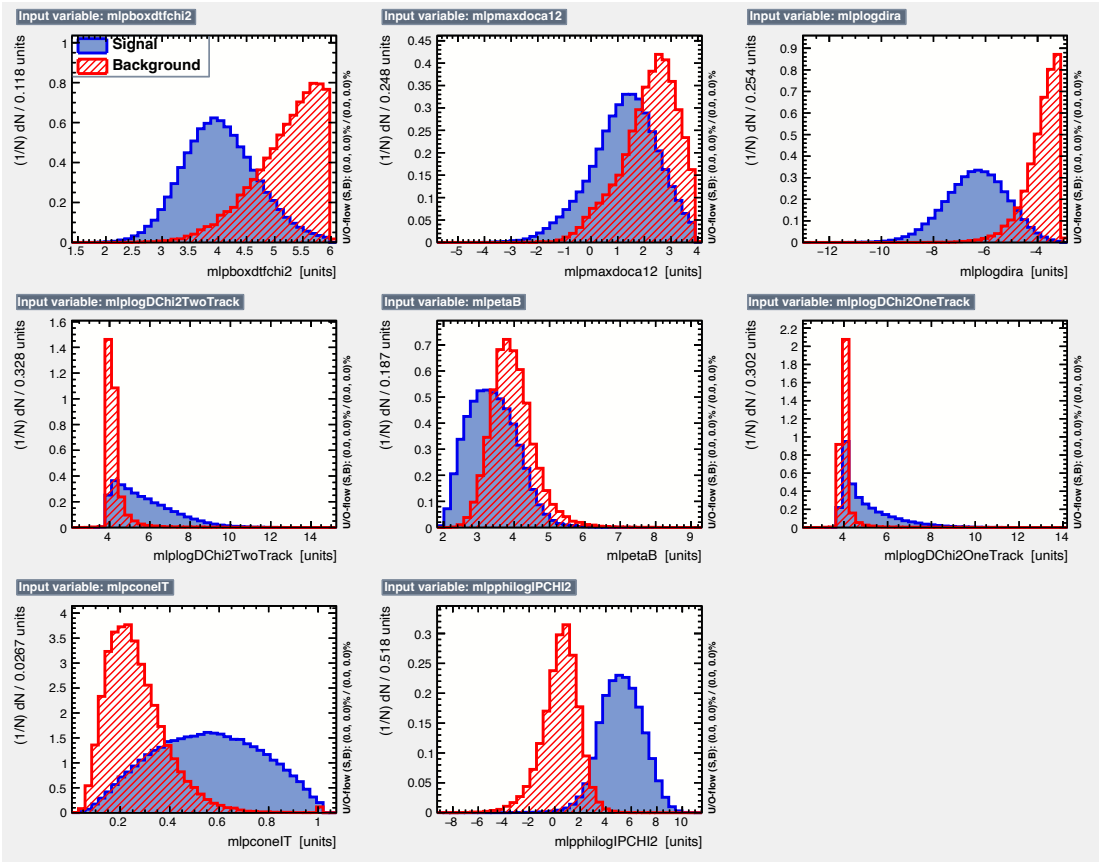

Figure 6.6 *The input variables for the MLP trained to remove D_s^+-tagged combinatorial background. The signal distributions are shown in solid blue and the background distributions are shown in hatched red.*

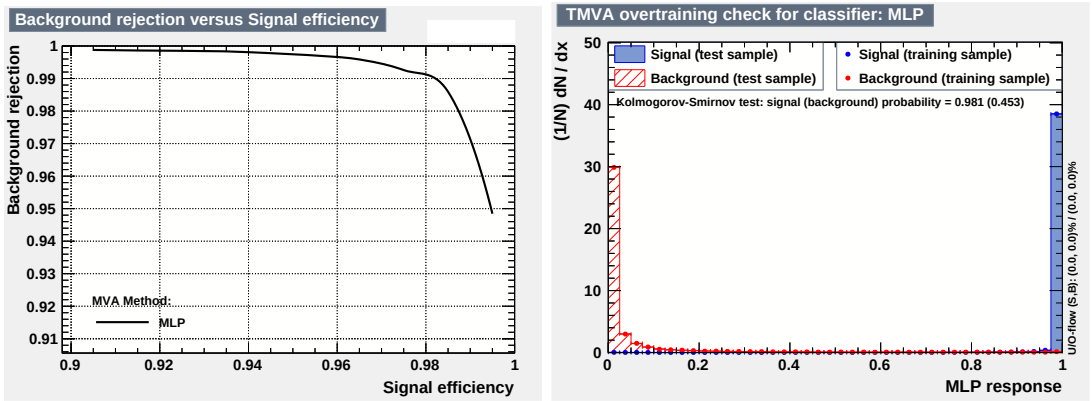

Figure 6.7 *The ROC curve (left) and classifier output distributions (right) for the MLP trained to remove D_s^+-tagged combinatorial background. The classifier output distribution on the right shows the classifier response to signal (blue) and background (red). The samples used for training are represented by the points and the samples used for testing are represented by the shaded regions.*

Second stage targetting non-D_s^+-tagged background

The second stage of the combinatorial background MVA is designed to target more general combinatorial background that does not come from D_s^+ decays. The classifier is a BDT trained with XGBoost [139], trained using truth-matched MC as the signal sample and the non-D_s^+-tagged data sidebands as background. In this case the background sidebands are defined as $M(K^+K^-K^+K^-) < 5100$ MeV/c^2 or $M(K^+K^-K^+K^-) > 5650$ MeV/c^2. In order to reduce the overlap between the MVAs, a loose requirement is made on the MLP classifier at 0.2 which removes around 50% of the D_s^+ background. As previously mentioned, events with a TIS decision at L0 will have slightly different kinematics to those with a TOS decision. For this reason, this stage of the MVA is split in two with a classifier for each of the TIS and TOS categories. In order to split this way, we require that TIS events have a positive TIS decision and a negative TOS decision, since it is possible that an event can have both TIS and TOS decisions at L0. Here the important criteria is that an event is triggered as TIS only, and so any events that have both TIS and TOS decisions at L0 are labelled as TOS events.

The XBDT classifier uses the transverse momentum of the B-candidate as a discriminating variable. Since the simulation does not describe the B-meson p_T distribution accurately the simulation is reweighted to improve agreement with the data. This reweighting is performed seperately for TIS and TOS events. The result of this is better agreement in the classifier response for data and MC. The other variables used as discriminating variables are described in Appendix B.2.

The performance of these classifiers is shown by the ROC curves in Figure 6.8 and the classifier output distributions in Figure 6.9. The ROC curves shown are for Run 2 samples, shown separately for the TIS and TOS classifier. The area under the ROC curve is given in the plot as a measure of the performance, where perfect performance would have a ROC curve with an area of 1. The classifier output distributions shown are for Run 1 (top of the figure) and Run 2 (bottom of the figure), for both TOS (left) and TIS (right) categories. These show good separation between signal and background and do not display sign of overtraining.

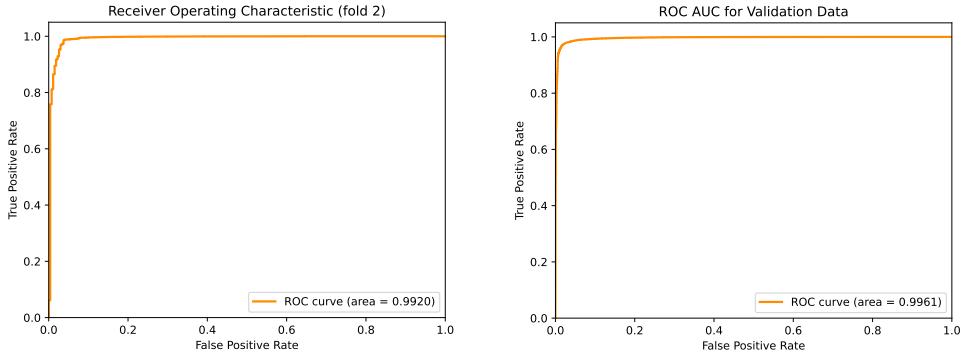

Figure 6.8 *ROC curves the XBDT classifier, shown for TOS events (left) and TIS events (right).*

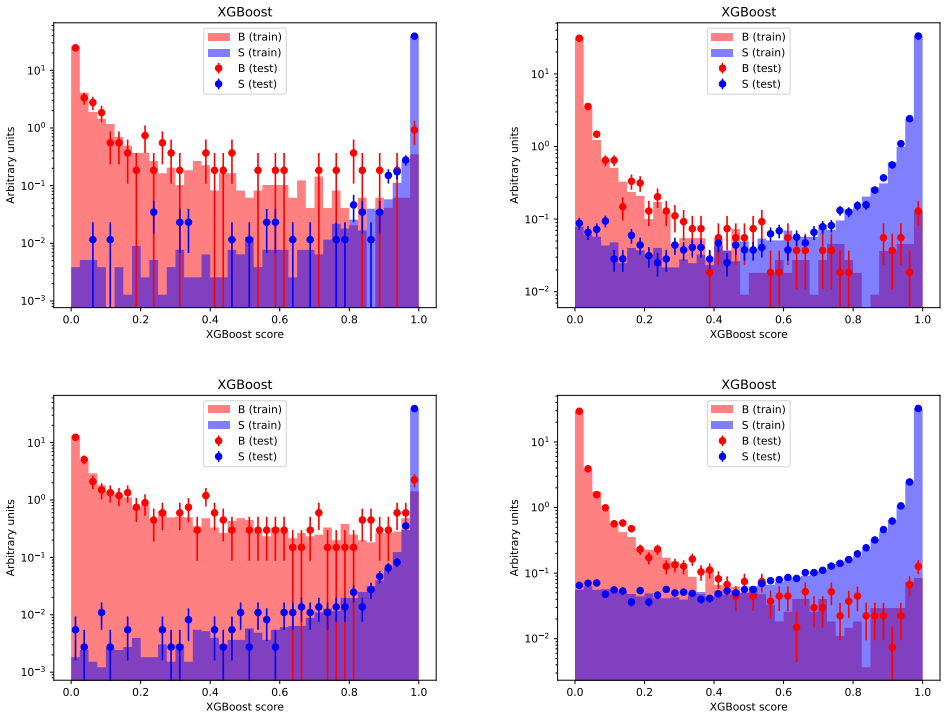

Figure 6.9 *Classifier output distributions for the XGBT classifier, shown for TOS (left) and TIS (right), where the y-axis is in log scale. The plots on the top of the figure show Run 1, with the plots on the bottom showing Run 2. Background is shown in red and signal is shown in blue. The samples used to train the classifier are shown with the shaded regions and the samples used to test the classifier are represented by the points.*

6.4 Working point optimisation

The selections on the first stage MLP, the second stage XBDT, and also the selection on particle identification are all able to remove background with some

efficiency of retaining signal. The selection on each of these is optimised to achieve the best possible background removal without compromising the efficiency of retaining any $B^0 \to \phi\phi$ signal. To do this, a figure of merit is chosen to quantify the performance of each working point and to choose an optimal selection. The chosen figure of merit is the Punzi multi-channel figure of merit [140, 141]. This is chosen since the data is partitioned into the two TIS and TOS categories. The figure of merit is defined as,

$$\text{FOM} = \frac{A^2/B}{a/2 + A^{3/2}/B}, \tag{6.2}$$

where,

$$A = \sum_i \frac{\epsilon_i^2}{b_i} \quad , \quad B = \sum_i \frac{\epsilon_i^3}{b_i^2} \tag{6.3}$$

where ϵ_i is the efficiency of the selection on signal in category i, b_i is the estimated background level in the blind region in category i and a is the signal significance that the selection is optimised for. In this case, a is set to 3 in this case to optimise for 3σ evidence. The signal efficiency is obtained from simulation and the expected background level is calculated by fitting the data with the full selection applied to the complete model. Each of the shapes for the background contributions are interpolated into the blind region and the integral calculated to give the total estimated background. The two categories, i, are TIS and TOS events. The scan is done separately for Run 1 and Run 2 data.

The XBDT classifier cut is scanned for both TIS and TOS events. The scans are repeated for multiple cut points on the MLP and with multiple values of the cut on particle identification, specifically on the minimum value of the combination (`ProbNNK(1-ProbNNpi)`) for each kaon track. The choice of denominator when calculating these efficiencies is made as the total number of events in simulation surviving all selections except the MLP, PID and XBDT cuts. This allows a global comparison across the scans done at various MLP and PID cut values. As the result of the several scans, the optimal MLP cut is chosen as 0.95, and a cut is applied on the minimum value of `ProbNNK(1-ProbNNpi)` at 0.05. This MLP cut corresponds to 97.74% (97.75%) signal efficiency for a rejection of D_s^+-tagged background of 99.0% (99.2%) in Run 1 (Run 2). In the scan corresponding to these MLP and PID selections, the optimal cut points on the XBDT are chosen as 0.97 (0.975) for TIS events and 0.995 (0.998) for TOS events in Run 1 (Run 2) corresponding to an overall efficiency of the XBDT selection of 92.7% (82.63%) in Run 1 (Run 2). This is shown in the scans in Figure 6.10. The scan for Run

Selection	B^0 efficiency (%)	B_s^0 efficiency (%)
Stripping, acceptance, reconstruction and preselection	4.939 ± 0.011	5.469 ± 0.007
ϕ mass window	91.99 ± 0.06	91.80 ± 0.03
Cut on B-meson mass error	98.79 ± 0.03	98.48 ± 0.02
`ProbNNpi` < 0.9	98.72 ± 0.03	98.76± 0.01
`ProbNNk(1-ProbNNpi)` > 0.05	93.18 ± 0.06	92.85 ±0.03
Λ_b^0 veto	96.56 ± 0.05	96.59 ± 0.02
Muon veto	93.21 ±0.07	93.34 ± 0.03
Kaon interaction BDTG	83.02 ± 0.10	79.67 ± 0.06
MLP	97.74 ± 0.04	97.75 ± 0.02
XBDT	87.83 ± 0.10	87.85 ± 0.05
$B^0 \to \phi K^*(892)$ veto	99.39 ± 0.02	96.95 ± 0.03
All selections (not truth matched)	2.632 ± 0.008	2.712 ± 0.005

Table 6.4 *Efficiency of selections calculated with Run 2 MC. All efficiencies are calculated with respect to the previous step, except for the first step which is calculated with respect to the number of events generated.*

1 shown at the top of Figure 6.10 shows several points yielding high sensitivity. These points are all consistent within the uncertainties and the tightest cut point is chosen. It is also checked that a cut point for TIS XBDT < 0.95 does not give higher values of the figure of merit. Scans at other working points of the MLP and PID points are shown in Appendix C.

6.5 Full selection criteria and efficiencies

The efficiency of the full selection is calculated using signal MC for $B_s^0 \to \phi\phi$ and $B^0 \to \phi\phi$. Table 6.4 shows the efficiency of each cut applied sequentially, with the efficiencies calculated with respect to the previous selection in the table. For the stripping, acceptance, reconstruction and preselection, the efficiency is calculated with respect to the total number of events generated which has been corrected for any differences in MC generation efficiencies.

The ratio of the selection efficiencies for $B^0 \to \phi\phi$ and $B_s^0 \to \phi\phi$ is calculated for Run 1 and Run 2 separately and included in the fit to data to correct the B^0 yield. The ratio is found to be 1.006 ± 0.006 for Run 1 and 0.971 ± 0.003 for Run 2.

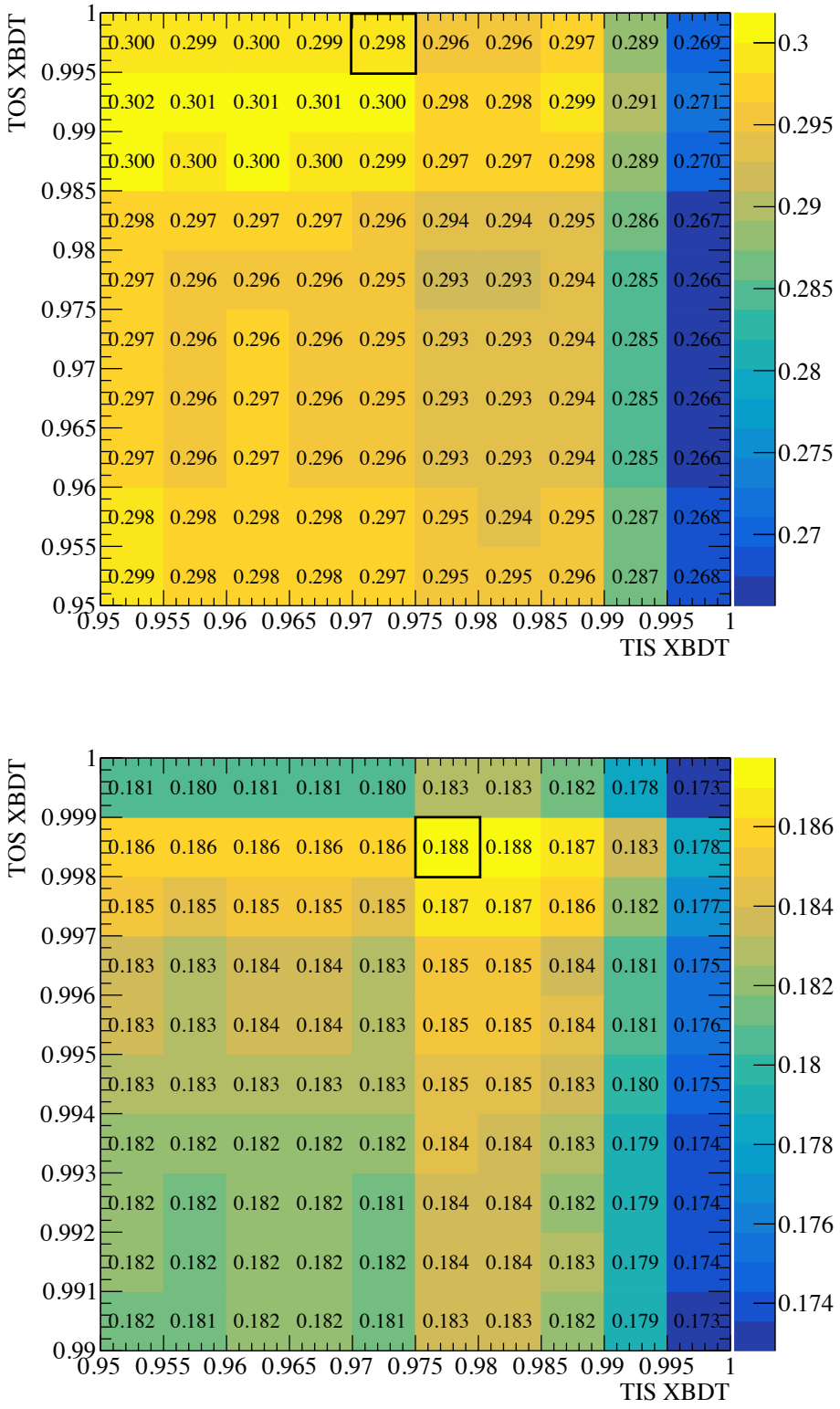

Figure 6.10 *Results of multi-channel Punzi scan with a cut on the MLP at 0.95 and a cut on the minimum value of* `ProbNNK(1-ProbNNpi)` *at 0.05. Run 1 is shown on the top, and Run 2 on the bottom. The chosen cut points are highlighted by black outline.*

Chapter 7

Modelling the $K^+K^-K^+K^-$ invariant mass distribution

In this chapter, the modelling of the contributions to the $K^+K^-K^+K^-$ invariant mass spectrum is described. Firstly, the modelling of the signal mode, $B^0 \to \phi\phi$, and the normalisation mode, $B^0_s \to \phi\phi$, is described. These modes are nearly identical so have the same treatment. This model is validated with a spurious signal test [142]. Each background contribution is then described in turn.

7.1 Modelling $B^0_{(s)} \to \phi\phi$ decays

The shape of the $B^0_{(s)} \to \phi\phi$ invariant mass distributions are caused by various effects. The tails of the distributions depend on the hadronic interactions and decays-in-flight, discussed in Chapter 5. The remaining tail after the full selection needs careful modelling to demonstrate clear understanding of the contributions from $B^0_s \to \phi\phi$ in the $B^0 \to \phi\phi$ mass range. Another effect is driven by the fraction of events that pass the L0 trigger with either a TIS or TOS decision. The different requirements imposed in the trigger leads to different kinematics and hence the mass resolution for each trigger category. To correctly model this effect, the simulation is reweighted so that the fraction of TIS and TOS events matches that of the data. Using data in the mass range 5320 MeV/c^2 $< M(K^+K^-K^+K^-) <$ 5380 MeV/c^2, the sample of $B^0_s \to \phi\phi$ decays is sufficiently pure to calculate the fractions of TIS and

	data	MC
Run 1: TOS/TIS	0.675	0.905
Run 2: TOS/TIS	0.728	0.910

Table 7.1 *Fraction of TOS/TIS events in data and MC. The MC fraction is tuned to match the data fraction.*

TOS events. Table 7.1 shows the calculated fractions of TIS and TOS events in both data and MC. These fractions are used to correct the MC by randomly removing TOS events. Well-reconstructed events and poorly-matched events can be separated in simulation using the Monte Carlo truth information. A tool exists that attempts to categorise candidates according to whether they are signal or one of several background categories [143]. The relevant categories here are *well-reconstructed* and *ghosts*. The latter is dominated by signal candidates that fail the truth-matching due to missed associated hits. Ghost candidates can contribute to the $B_s^0 \to \phi\phi$ signal distribution in data and so need to be modelled. Candidates coming from kaon interactions can be in either category. The training sample is split according to this category to develop the full model. Each sample is fit with a Student-T for the core and a Gaussian to capture the kaon interaction events. The results of these fits are shown in Figure 7.1, with fitted values of the parameters shown in Table 7.2. Note that the core width of the ghost category events is 17% larger than that of well-reconstructed events.

The models are developed using the Run 2 $B_s^0 \to \phi\phi$ simulation, tuned to match the data TIS and TOS fractions. The simulation is randomly split in half to form two samples, one for developing the model and one for testing its validity. These are referred to as the training and testing samples respectively. After applying the full selection, there are three shapes contributing. These shapes come from: *well-reconstructed* signal, *ghosts* and any remaining candidates coming from kaon interactions. Each of these categories of events contributes differently to the overall invariant mass distribution and is therefore modelled separately. Well-reconstructed signal, which forms 97.9% of the sample, is well modelled by a Student-T distribution (see Appendix A.1). The events with poorly matched tracks, contributing 1.9% to the sample, are well modelled by a Student-T distribution with a larger width than that of the well-reconstructed events. The final 0.2% are the remaining events with kaon interactions and decays-in-flight. These are well described by a wide Gaussian.

These two categories are then recombined and fit to the full model, consisting of two Student-T distributions, one for each of well-reconstructed events and

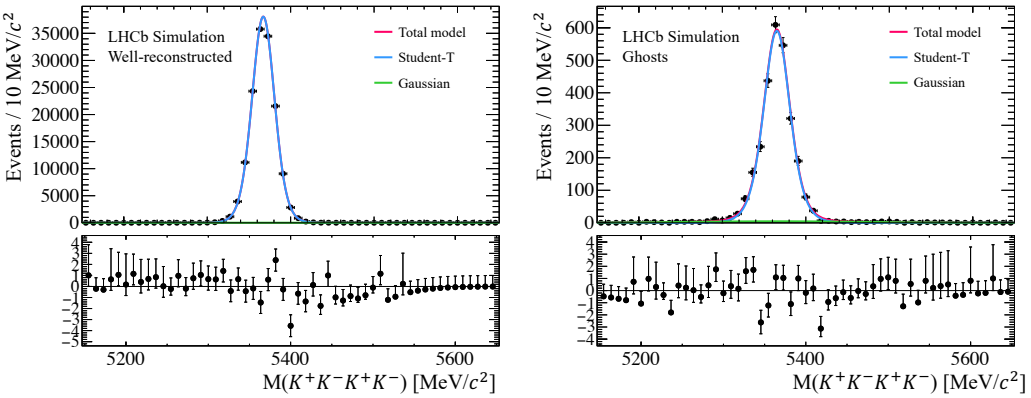

Figure 7.1 *Fit to signal MC invariant mass distribution split into categories of well-reconstructed and ghosts. Each category is fit to a Student-T distribution to represent the core and plus Gaussian distribution to represent the tail events coming from kaon interactions. The distribution of ghost events has a core width that is 17% larger than that of the well-reconstruced events.*

Parameter	Well-reconstructed	Ghosts
μ [MeV/c^2]	5367.20 ± 0.04	5365.27 ± 0.35
s_{ST} [MeV/c^2]	13.64 ± 0.03	16.01 ± 0.34
n_{ST} [MeV/c^2]	14.37± 0.42	7.71 ± 1.50
f	0.9984 ± 0.0002	0.956 ± 0.007
σ_{G} [MeV/c^2]	72.8 ± 4.3	102.7 ± 10.4

Table 7.2 *Parameter value results for fits to well-reconstructed and ghost events in the Run 2 MC training sample. The fraction, f, represents the number of events in the Student-T distribution.*

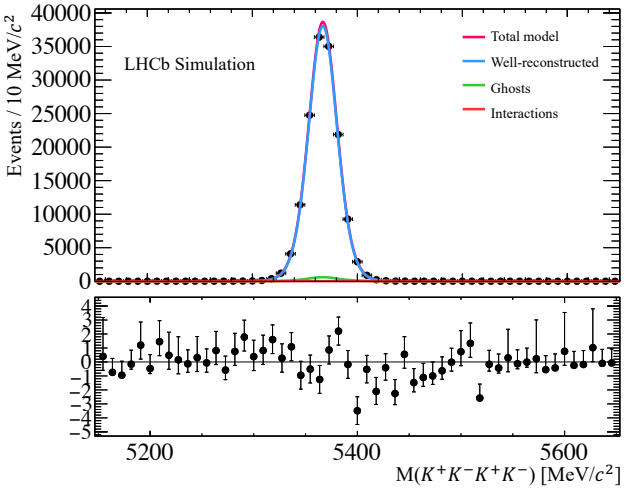

Figure 7.2 *Result of the fit to the full training MC sample. The sample is fit to a sum of two Student-T distributions and a shallow Gaussian.*

Parameter	Value
μ [MeV/c^2]	5367.17 ± 0.04
f_0	0.979
s_0 [MeV/c^2]	13.66 ± 0.03
n_0 [MeV/c^2]	14.98 ± 0.52
f_{60}	0.019
s_{60} [MeV/c^2]	16.01
n_{60} [MeV/c^2]	4.25 ± 2.91
σ_G [MeV/c^2]	87.1 ± 4.4

Table 7.3 *Parameter value results for fit to the full testing MC sample. The fraction, f_0, represents the number of events in the Student-T distribution for the well-reconstructed events, and the fraction, f_{60}, represents the number of events in the Student-T distribution for the ghost events. Values quoted without errors are fixed in the fit.*

poorly-matched events, and a single wide Gaussian for the interactions. The full fit model is given by

$$P(m) = f_0 ST(m|\mu, s_0, n_0) + f_{60} ST(m|\mu, s_{60}, n_{60}) + (1 - f_0 - f_{60}) G(m|\mu, \sigma_G), \quad (7.1)$$

where the subscript 0 refers to well-reconstructed events and the subscript 60 refers to ghost events. The definitions for the parameters of the Student-T distribution are detailed in Appendix A.1. The fractions f_0 and f_{60} are fixed to the values obtained from simulation. The fit to the full training sample is shown in Figure 7.2, with the fitted values of the parameters given in Table 7.3.

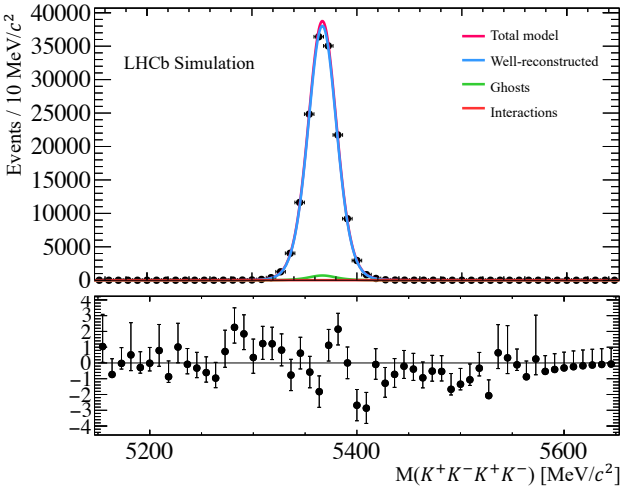

Figure 7.3 *Result of the fit to the full testing MC sample. The sample is fit to a sum of two Student-T distributions and a shallow Gaussian with only the mean and a scale factor allowed to vary.*

Parameter	Value
μ [MeV/c^2]	5367.10 ± 0.04
n_0	13.66 ± 0.33

Table 7.4 *Result of the fit Parameters to the full testing MC sample.*

To ensure this is a good description of the signal, the testing sample is fitted to the model. We introduce a scale factor, s_F, that multiplies both width parameters for the well-reconstructed and ghost events. This allows the model to be used on both Run 1 and Run 2 data, and for both $B^0_s \to \phi\phi$ and $B^0 \to \phi\phi$ shapes. Here, we fix its value to 1. All parameters are fixed to the values in Table 7.2, with the n_0 and μ parameters, allowed to vary. The parameter n_0 controls the tails of the Student-T distribution for well-reconstructed events. The results of this fit to the test sample are shown in Figure 7.3 and Table 7.4.

This model is also checked for validity using the $B^0 \to \phi\phi$ simulation. Here, the scale factor and μ are allowed to vary as it is expected the result will be different. The parameter n_0 is fixed to the value from the validation fit as it is shared between the $B^0_s \to \phi\phi$ and $B^0 \to \phi\phi$ shapes in the fit to data. The results of this fit are shown in Figure 7.4 and Table 7.5, which demonstrates that the developed model describes both the $B^0_s \to \phi\phi$ and $B^0 \to \phi\phi$ signal well.

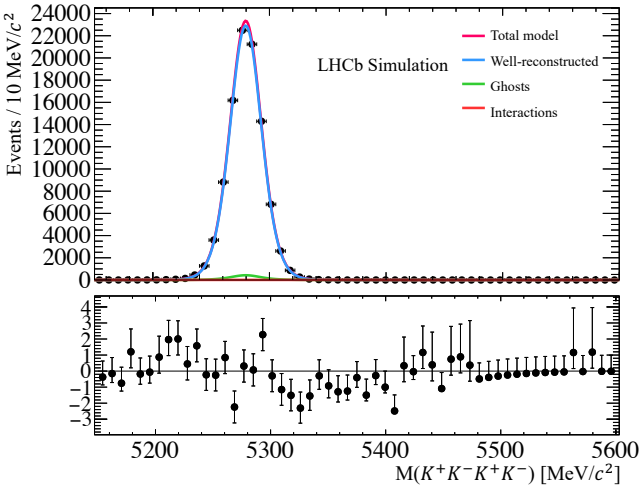

Figure 7.4 *Result of the fit to the $B^0 \to \phi\phi$ MC after the full selection. The sample is fit to a sum of two Student-T distributions and a shallow Gaussian with only the mean and a scale factor allowed to vary.*

Parameter	Value
μ [MeV/c^2]	5279.67 $\pm$ 0.05
s_F	0.996 $\pm$ 0.003

Table 7.5 *Result of the fit parameters to the $B^0 \to \phi\phi$ MC after the full selection.*

7.1.1 Testing for spurious signal

Another test to validate this model to be used for the $B_s^0 \to \phi\phi$ signal is the test for spurious signal as suggested in [142]. This test is used to validate that the model describes the signal sufficiently well that it does not falsely generate a $B^0 \to \phi\phi$ signal that is not there. To test this, the signal MC for $B_s^0 \to \phi\phi$ is split into 46 independent samples, where each of these samples contains roughly the same number of events as we expect in the Run 2 data. For each independent sample, a random sample of combinatorial background is generated from an exponential distribution and added. This provides 46 independent mock data sets with a $B_s^0 \to \phi\phi$ signal and combinatorial background. Each of these 46 samples is then fitted to a model containing $B_s^0 \to \phi\phi$ decays, a combinatorial model, and an additional component for the $B^0 \to \phi\phi$ decay that is allowed to vary freely. Since there is no added $B^0 \to \phi\phi$ component in the mock data samples, the fitted yield of $B^0 \to \phi\phi$ events should centre on zero. From this test, it is found that the model developed is unbiased and does not artificially generate a $B^0 \to \phi\phi$ signal. This is shown in Figure 7.5 which shows the distribution of the fitted $B^0 \to \phi\phi$ yields for all 46 samples. The mean of this distribution is consistent with zero, showing that this model is robust. The RMS of the distribution is less than 5 events. As the expected number of events for claiming evidence would be much greater than 5 events, this is not of concern.

7.2 Background modelling

The models for the $\Lambda_b^0 \to pK^-\phi$ and $B^0 \to \phi K^*(892)$ modes are developed using the full simulation after applying the full selection. For the background coming from $\Xi_b \to pK^-\phi$ and partially reconstructed decays of excited K^* mesons, RapidSim [116] is used to generate samples to develop a model.

7.2.1 Modelling $\Lambda_b^0 \to pK^-\phi$ and $\Xi_b \to pK^-\phi$

The background from $\Lambda_b^0 \to pK^-\phi$ is modelled well by a bifurcated Gaussian, shown in Figure 7.6, with the values of the fitted parameters given in Table 7.6. The yield of events coming from this source are estimated in a data-driven way, by applying the full selection but inverting the $\Lambda_b^0 \to pK^-\phi$ veto and using a looser

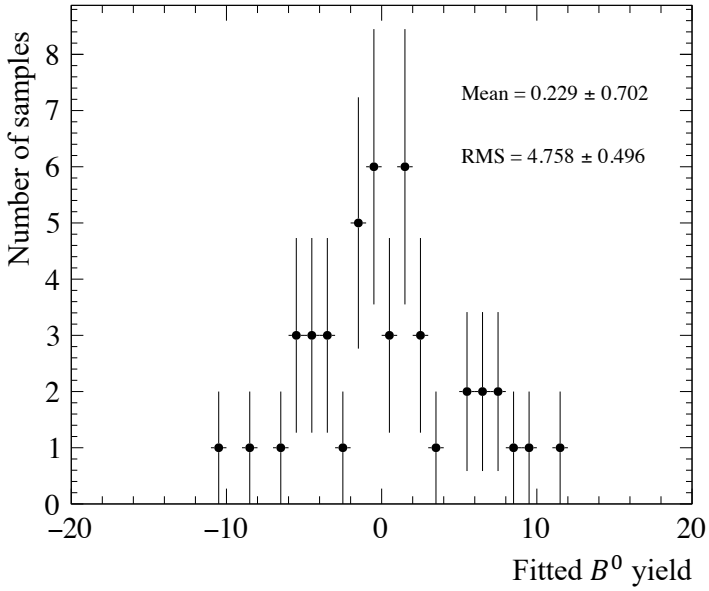

Figure 7.5 *The distribution of fitted $B^0 \to \phi\phi$ yields from 46 independent samples of data-like $B_s^0 \to \phi\phi$ decays and combinatorial background. This shows the $B_s^0 \to \phi\phi$ model and the combinatorial background model do not give rise to any spurious signal.*

ϕ mass window at ± 25 MeV/c^2. The fraction of events passing through the veto is calculated from the simulation as 0.61 ± 0.13. The veto selection is inverted on the data, which is then fitted to the $KKK\pi$ invariant mass. The data is modelled with a shape for the $\Lambda_b^0 \to pK^-\phi$ and a shape for the $\Xi_b \to pK^-\phi$ decay at the known $\Lambda_b^0 - \Xi_b$ mass splitting. The shapes of these are each double Gaussians. The yield of events failing the veto is calculated from the fit, and using the fraction of events that pass the veto, s_{PF} the expected yield of these background events is then $N_{\text{pass}} = s_{PF} \times N_{\text{fail}}$. In Run 1, the yield is of $\Lambda_b^0 \to pK^-\phi$ is estimated to be 6.7 ± 3.5 events. For Run 2, the yield is estimated to be 34.8 ± 10.5 events.

Events coming from $\Xi_b \to pK^-\phi$ appear in the high-mass sideband of the data. The distribution of $\Xi_b \to pK^-\phi$ events are described by a Crystal Ball function (see Appendix A.2), with parameters described in Table 7.7. The yield of these events is calculated in the same way as the $\Lambda_b^0 \to pK^-\phi$ yield and is found to be 0.0 ± 1.0 events in Run 1 and 5.6 ± 3.6 events in Run 2.

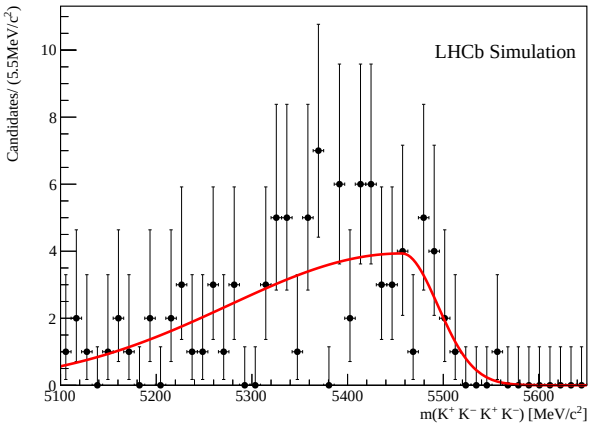

Figure 7.6 *Bifurcated Gaussian fit to $\Lambda_b^0 \to pK^-\phi$ MC after applying the full selection.*

Parameter	Value [MeV/c^2]
μ	5456 ± 26
σ_1	181 ± 30
σ_2	37 ± 32

Table 7.6 *Fit parameter results for the Bifurcated Gaussian shape that describes the shape of the $\Lambda_b^0 \to pK^-\phi$ background.*

Parameter	Value
μ [MeV/c^2]	5640.7 ± 1.2
σ [MeV/c^2]	28.7 ± 0.7
n	3.22 ± 0.30
s_F	0.28 ± 0.02

Table 7.7 *Fit parameter results for the Crystal Ball shape that describes the shape of the $\Xi_b \to pK^-\phi$ background.*

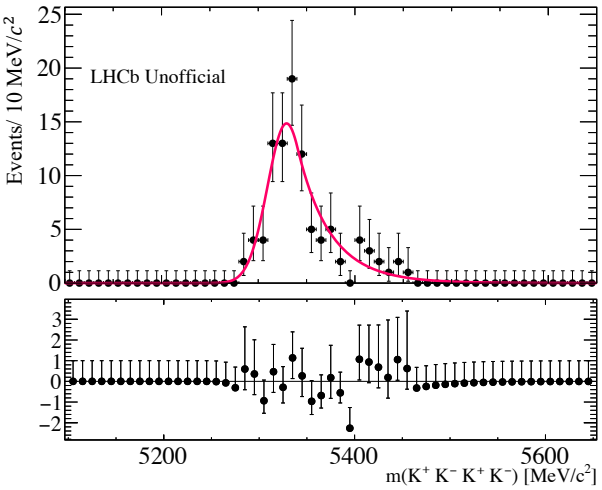

Figure 7.7 *Crystal Ball fit to $B^0 \to \phi K^*(892)$ MC after applying the full selection.*

Parameter	Value
μ [MeV/c^2]	5329 ± 4
σ [MeV/c^2]	19.7 ± 2.6
n	39.9 ± 32.2
s_F	-0.58 ± 0.11

Table 7.8 *Fit parameter results for the Crystal Ball shape that describes the shape of the $B^0 \to \phi K^*(892)$ background.*

7.2.2 Modelling $B^0 \to \phi K^*(892)$

The events coming from $B^0 \to \phi K^*(892)$ are modelled well by a Crystal Ball function. The fit is shown in Figure 7.7 with parameter values described in Table 7.8.

The fractional yield of $B^0 \to \phi K^*(892)$ candidates relative to the normalisation mode after all cuts is calculated using results from the previous LHCb measurement of the $B_s^0 \to \phi\phi$ branching fraction [144]. The fraction is calculated as shown,

$$f_{\phi K^*} = \frac{N^{2015}_{\phi K^*}}{N^{2015}_{\phi\phi}} \times \frac{\varepsilon^{2015}_{\phi\phi}}{\varepsilon^{2015}_{\phi K^*}} \times \frac{\varepsilon^{\text{gen}}_{\phi K^*}}{\varepsilon^{\text{gen}}_{\phi\phi}} \times \frac{\varepsilon^{\text{sel}}_{\phi K^*}}{\varepsilon^{\text{sel}}_{\phi\phi}} \tag{7.2}$$

where $N^{2015}_{\phi K^*}$ and $N^{2015}_{\phi\phi}$ are the measured yields of the $B^0 \to \phi K^*(892)$ and $B_s^0 \to \phi\phi$ candidates respectively and $\varepsilon^{2015}_{\phi K^*}$ and $\varepsilon^{2015}_{\phi\phi}$ are the selection efficiencies for $B^0 \to \phi K^*(892)$ and $B_s^0 \to \phi\phi$ candidates respectively, taken from the previous LHCb result [144]. The selection efficiencies, $\varepsilon^{\text{sel}}_{\phi K^*}$ and $\varepsilon^{\text{sel}}_{\phi\phi}$, are calculated

from simulation and corrected by the generator level efficiencies, $\varepsilon^{\text{gen}}_{\phi K^*}$ and $\varepsilon^{\text{gen}}_{\phi\phi}$. This calculation gives $f_{\phi K^*} = (24 \pm 4) \times 10^{-4}$ in Run 1 and $f_{\phi K^*} = (22 \pm 2) \times 10^{-4}$ in Run 2.

7.2.3 Partially reconstructed backgrounds from excited K^* decays

In addition to background from $B^0 \to \phi K^*(892)$ decays, decays with excited K^* states may also contribute to the background distribution. In particular, $K_1(1270)$ and $K_2^*(1430)$ have large fractions to $K\pi^+\pi^-$ which can contribute to background if one of the pions is misidentified and the other is missed. Using the decay modes $B_{u,d} \to \phi K_1(1270)$ and $B_{u,d} \to \phi K_2^*(1430)$, the shape of the partially reconstructed background and expected yield can be obtained using RapidSim [116]. The shape of this contribution can be described with a Gaussian kernel PDF function (see Appendix A.3). The fit result is shown in Figure 7.8. These events are suppressed by the ϕ mass window and PID, and the yield of this mode relative to the $B_s^0 \to \phi\phi$ decay is estimated to be $(12 \pm 2) \times 10^{-4}$. This is calculated using known branching fractions.

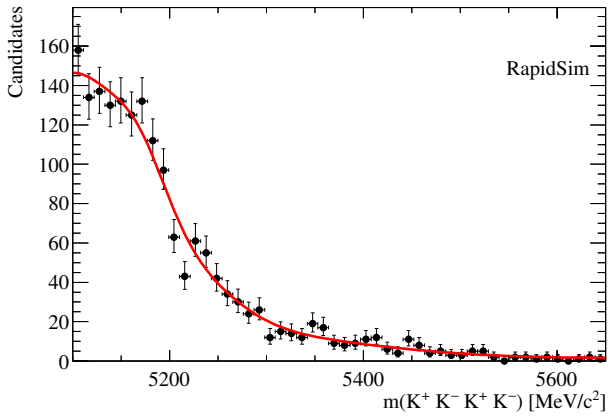

Figure 7.8 *Fit of a Gaussian kernel PDF to partially reconstructed excited K^* simulation samples.*

Chapter 8

Results

This chapter presents the final results of the analysis, including the results of the fit to the full dataset, toy studies to demonstrate significance, and the limit on the branching fraction calculated using the CL_s method [125, 126]. Section 8.1 describes the results of the full fit to the four-kaon invariant mass spectrum and the studies of toy datasets, and Section 8.2 describes the CL_s test and the upper limit that is calculated for the $B^0 \to \phi\phi$ branching fraction. The largest source of systematic uncertainty is from the measurement of the $B_s^0 \to \phi\phi$ branching fraction. Many sources of experimental uncertainty cancel due to the choice of normalisation mode having the same final state as the signal mode. In the studies of significance in Section 8.1.1 and for the limit calculation in Section 8.2, systematic uncertainties from modelling or the use of external measurements are accounted for by fluctuating the parameters within their uncertainty when generating the toy datasets.

8.1 Fit to four-kaon invariant mass distribution

Two fits are performed to the data. One fit is the full signal plus background model, shown at the top of Figure 8.1, while the other is the background-only model where the value of the $B^0 \to \phi\phi$ branching fraction is fixed to zero, shown in the bottom of Figure 8.1. The values of the fitted parameters are shown for each fit in Table 8.1. While the pull distributions suggest mismodelling around the $B_s^0 \to \phi\phi$ peak, the model of $B_s^0 \to \phi\phi$ is physically well-motivated, all pulls

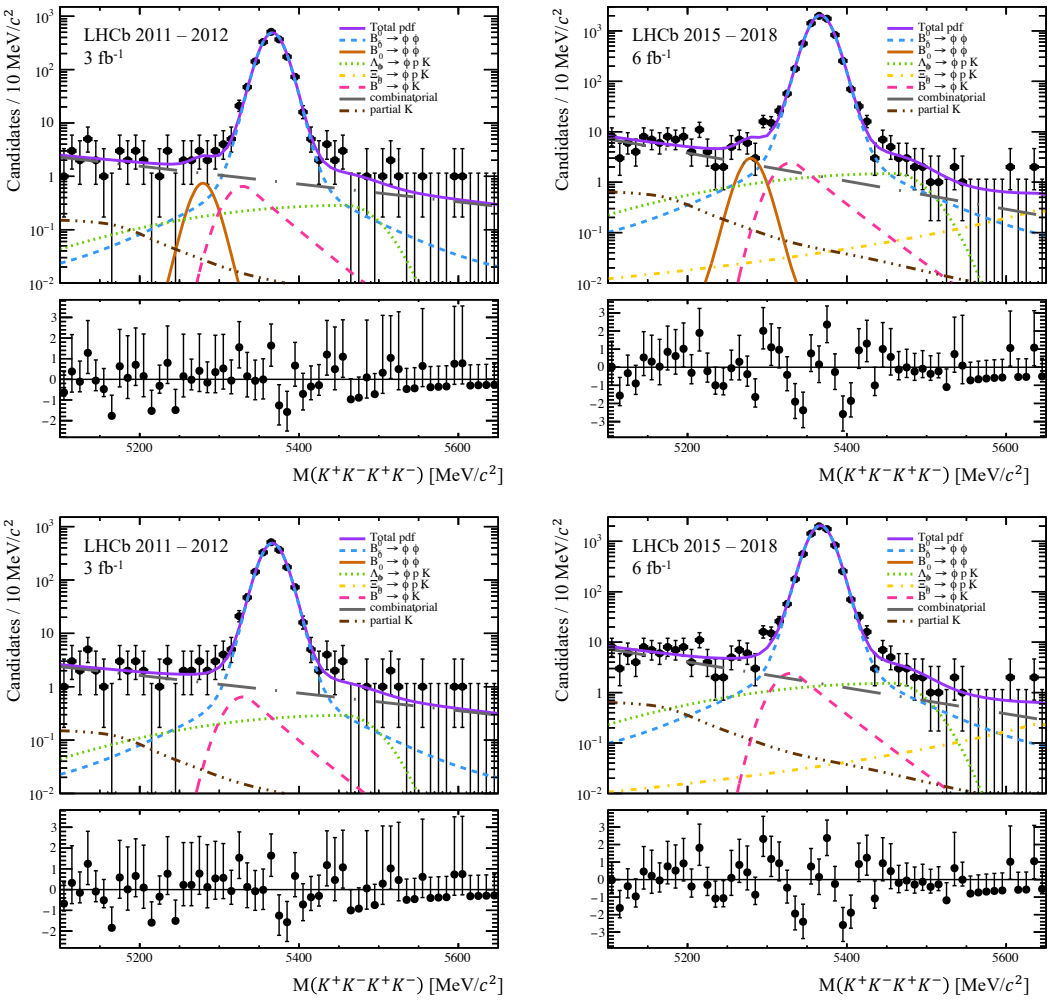

Figure 8.1 *Fit to data including a component for $B^0 \to \phi\phi$ (top) and without including a component for $B^0 \to \phi\phi$ (bottom). The left shows Run 1 data, with Run 2 data on the right.*

are within 3σ and the fit results are stable when modifications are made to the model.

The yield of $B^0 \to \phi\phi$ candidates is parameterised in terms of the yield of $B_s^0 \to \phi\phi$ candidates and the $B_s^0 \to \phi\phi$ branching fraction. The yield of $B_s^0 \to \phi\phi$ candidates is corrected by the expected S-wave contribution [144] and the ratio of efficiencies as calculated in Section 6.5. In order to calculate the $B^0 \to \phi\phi$ branching fraction relative to $B_s^0 \to \phi\phi$ events, the fragmentation fraction f_s/f_d must be taken into account which would lead to a large systematic uncertainty. Since the $B_s^0 \to \phi\phi$ branching fraction is measured relative to $B^0 \to \phi K^*(892)$ decays, the fragmentation fraction may be cancelled out using the results from

Parameter	Status	Without $B^0 \to \phi\phi$	With $B^0 \to \phi\phi$
f_0	fixed	0.979	0.979
f_{60}	fixed	0.019	0.019
$\mu_{B_s^0}$ [MeV/c^2]	free	5366.63 ± 0.16	5366.64 ± 0.16
s_0 [MeV/c^2]	fixed	13.66	13.66
s_{60} [MeV/c^2]	fixed	16.0097	16.0097
n_0 [MeV/c^2]	free	12.53 ± 1.50	12.58 ± 1.49
n_{60} [MeV/c^2]	constrained	1.051 ± 0.004	1.03 ± 0.74
$a^{\text{Run 1}}$	fixed	0.98	0.98
$a^{\text{Run 2}}$	fixed	1	1
σ_G [MeV/c^2]	constrained	86.74 ± 4.33	86.81 ± 4.34
$m_{B_s^0} - m_{B^0}$ [MeV/c^2]	constrained	-	87.22 ± 0.16
a_{B^0}	fixed	-	0.98152
$a_{\Xi_b^0}$	fixed	0.277	0.277
$\mu_{\Xi_b^0}$ [MeV/c^2]	fixed	5640.7	5640.7
$n_{\Xi_b^0}$	fixed	3.22	3.22
$\sigma_{\Xi_b^0}$ [MeV/c^2]	fixed	28.7	28.7
$a_{\phi K^*}$	constrained	-0.60 ± 0.11	-0.59 ± 0.11
$\mu_{\phi K^*}$ [MeV/c^2]	fixed	5329.29	5329.29
$n_{\phi K^*}$	fixed	39.86	39.86
$\sigma_{\phi K^*}$ [MeV/c^2]	constrained	20.3 ± 2.4	20.0 ± 2.4
$\mu_{\Lambda_b^0}$ [MeV/c^2]	constrained	5457.63 ± 16.82	5459.61 ± 17.75
$\sigma^1_{\Lambda_b^0}$ [MeV/c^2]	constrained	184.2 ± 27.2	185.0 ± 27.9
$\sigma^2_{\Lambda_b^0}$ [MeV/c^2]	constrained	35.3 ± 8.9	34.6 ± 9.2
$\tau^{\text{Run 1}}_{\text{comb.}}$	free	-0.00380 ± 0.00110	-0.00386 ± 0.00117
$\tau^{\text{Run 2}}_{\text{comb.}}$	free	-0.00592 ± 0.00115	-0.00642 ± 0.00154
$N^{\text{Run 1}}_{B_s^0}$	free	1683.81 ± 41.4	1684.3 ± 41.5
$N^{\text{Run 1}}_{\Lambda_b^0}$	constrained	7.6 ± 3.4	7.5 ± 3.4
$N^{\text{Run 1}}_{\Xi_b^0}$	constrained	0.0 ± 2.7	0.0 ± 3.0
$N^{\text{Run 1}}_{\text{comb.}}$	free	54.8 ± 9.9	52.03 ± 10.4
$f^{\text{Run 1}}_{\phi K^*}$	constrained	0.0025 ± 0.0005	0.0025 ± 0.0005
$N^{\text{Run 2}}_{B_s^0}$	free	7153.1 ± 85.2	7154.0 ± 86.3
$N^{\text{Run 2}}_{\Lambda_b^0}$	constrained	40.2 ± 9.7	38.9 ± 9.8
$N^{\text{Run 2}}_{\Xi_b^0}$	constrained	3.4 ± 3.1	3.9 ± 3.1
$N^{\text{Run 2}}_{\text{comb.}}$	free	118.9 ± 17.6	108.9 ± 21.0
$f^{\text{Run 2}}_{\phi K^*}$	constrained	0.0022 ± 0.0002	0.0022 ± 0.0002
$f_{\text{partial}K^*}$	constrained	0.0012 ± 0.0.0002	0.0012 ± 0.0.0002
$\mathcal{B}(B^0 \to \phi\phi)$	free	-	0.74 ± 0.44
Negative Log Likelihood		0	-1.66

Table 8.1 *Fit results for the simultaneous fits to Run 1 and Run 2 data, both with and without shape for the $B^0 \to \phi\phi$ component. Values quoted without uncertainty are fixed in the fit.*

this measurement [144],

$$\frac{\mathcal{B}(B_s^0 \to \phi\phi)}{1/(f_s/f_d)} = (477 \pm 37) \times 10^{-8}. \tag{8.1}$$

The yield of $B^0 \to \phi\phi$ candidates is therefore parameterised as follows,

$$N_{B^0} = N_{B_s^0}^{\text{corrected}} \times \mathcal{B}(B^0 \to \phi\phi) \times \frac{1/(f_s/f_d)}{\mathcal{B}(B_s^0 \to \phi\phi)}, \tag{8.2}$$

where $N_{B_s^0}^{\text{corrected}}$ is the yield of $B_s^0 \to \phi\phi$ candidates corrected for the potential S-wave contribution and the ratio of selection efficiencies. The results of these fits show no significant $B^0 \to \phi\phi$ yield, with the best fit value of 12.7 ± 7.7 events in the full dataset. This yield has a significance, S, of 1.8σ calculated assuming Wilks' theorem [145],

$$S = \sqrt{2\log(\Lambda)}, \tag{8.3}$$

where Λ is the ratio of the likelihoods of each fit. For the signal plus background model, the best fit value of the branching fraction is found to be $(0.74 \pm 0.44) \times 10^{-8}$. Therefore, no significant signal is seen.

8.1.1 Studies of significance with toy data samples

A robust way of determining the significance of the result is by generating many toys for the background-only hypothesis and fitting these toy samples to the signal plus background model. In doing this, a distribution branching fraction values is obtained. To find the significance, we find the fraction of generated toys that are found to have a branching fraction greater than or equal to the best fit value, 0.74. The distribution of fitted branching fractions is shown in Figure 8.2. It is found that of these 1500 toys, 3.73% of them fit a value of the branching fraction greater than $(0.74 \pm 0.44) \times 10^{-8}$. This is a p-value of 0.0373, corresponding to a significance of $1.9\sigma(2.1\sigma)$ for a one-(two-)sided test.

8.1.2 Likelihood profile of the branching fraction

The significance of the result and the limit on the branching fraction can also be seen by the profile likelihood of the branching fraction. The profile likelihood is produced by calculating, for a set of given hypotheses, the likelihood ratio of

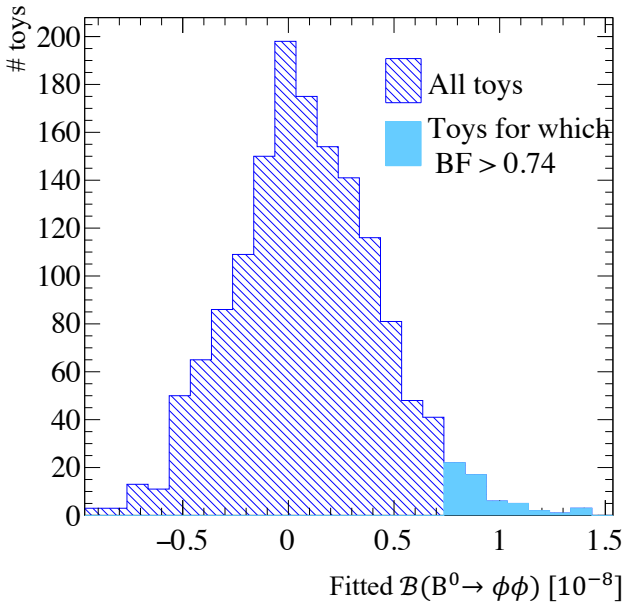

Figure 8.2 *Distribution of the fitted values of the $B^0 \to \phi\phi$ branching fraction, for 1500 background-only toy datasets. This shows how significant the signal plus background model is on data.*

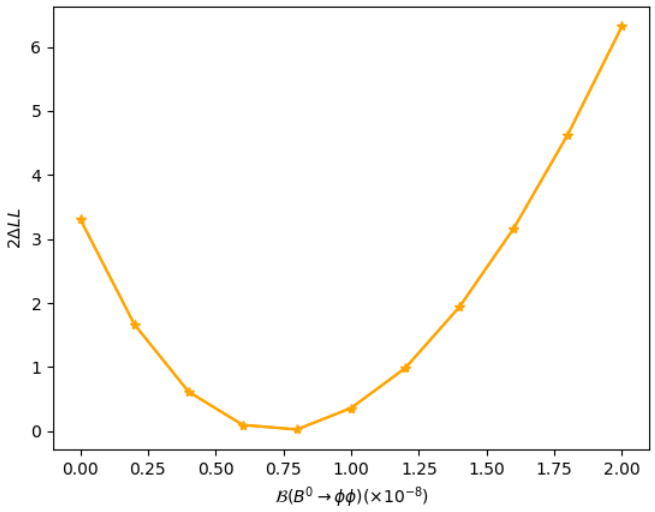

Figure 8.3 *The profile likelihood of the $B^0 \to \phi\phi$ branching fraction.*

fitting the data to the signal plus background model with the branching fraction value free to vary or fixed to the value of the hypothesis under test. This produces a curve that is at a minimum around the best fit value of the branching fraction and intercepts the y-axis at the significance of the best fit result. By finding the branching fraction value that has a value of the likelihood ratio equivalent to 90% significance, one can obtain an estimate for the 90% limit on the branching fraction. The likelihood profile for the branching fraction is shown in Figure 8.3.

8.2 CL_s method for setting a limit on the $B^0 \to \phi\phi$ branching fraction

Since no significant signal yield is seen, a limit is set on the branching fraction using the CL_s method [125, 126]. To perform the CL_s test, a series of toy data samples are used to understand the sensitivity of this analysis to a signal and calculate the 90% and 95% upper limits on the branching fraction. The fit to data is used to generate toy data samples with multiple values for $\mathcal{B}(B^0 \to \phi\phi)$. CL_s is defined as follows,

$$\mathrm{CL}_s \equiv \frac{\mathrm{CL}_{s+b}}{\mathrm{CL}_b}, \tag{8.4}$$

where CL_{s+b} is the probability that the value of the test statistic, t, to be as large or larger under the signal and background hypothesis, and $1 - \mathrm{CL}_b$ is the probability for the value of t to be as small as or smaller under the background only hypothesis. The expected value of CL_s for a particular branching fraction value is calculated from the distribution of t for the toys with no signal and the toys with signal,

$$\mathrm{CL}_{s+b} = \int_{t_{\mathrm{exp}}}^{\infty} g(t; s+b)\mathrm{d}t \tag{8.5}$$

$$1 - \mathrm{CL}_b = \int_{-\infty}^{t_{\mathrm{exp}}} g(t; b)\mathrm{d}t \tag{8.6}$$

where $g(t; s+b)$ is the distribution of the test statistic under the signal and background hypothesis and $g(t; b)$ is the distribution of the test statistic under the background only hypothesis. In practice, the value of t_{exp} is found as the median value of $g(t; s+b)$. This gives the expected value of CL_s. These values are plotted as a function of the branching fraction hypothesis.

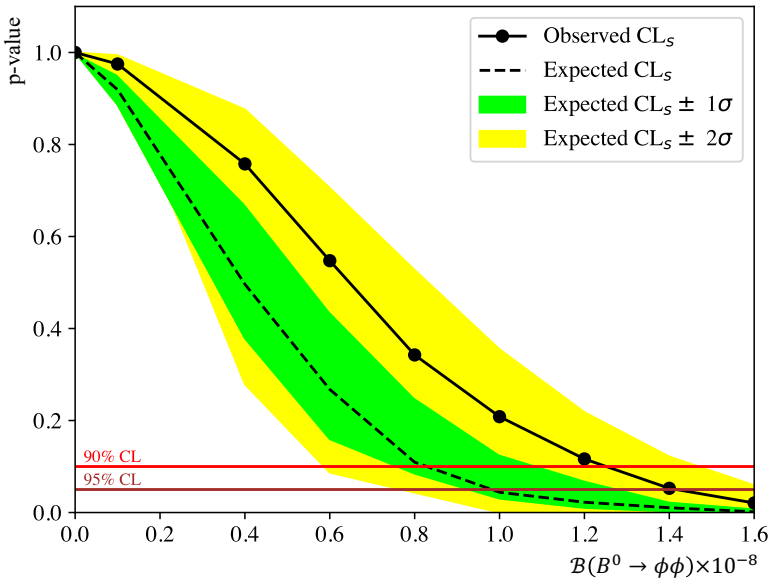

Figure 8.4 *Results of the CL_s calculation showing the expected and observed CL_s values for various signal hypotheses. This plot shows that the 90%(95%) limit on the branching fraction is at* $1.3(1.4) \times 10^{-8}$.

The limit on the $B^0 \to \phi\phi$ branching fraction is set using background-only pseudexperiments and psuedoexperiments with trial branching fractions from 0.1×10^{-8} to 1.6×10^{-8} Each toy is fit to the background-only and signal plus background models to calculate the test statistic: the likelihood ratio. These distributions are then used to produce the plot of the CL_s values for each hypothesis. This plot is then used to find the hypothesis for which the CL_s value is either 90% or 95%. The results of the CL_s calculation is shown in Figure 8.4.

The results of this calculation show that the 90% limit on the $B^0 \to \phi\phi$ branching fraction can be set at 1.3×10^{-8}. This is the world's best limit on the branching fraction of the $B^0 \to \phi\phi$ branching fraction. The previous search for this mode, published by LHCb in 2019, had an expected limit at 90% at 2×10^{-8} and an observed limit at 2.7×10^{-8} [1]. The expected limit from this analysis is improved by a factor of 2.5. There is a factor of 2 increase due to luminosity but sensitivity is further improved with a factor of 2 reduction in the background. The number of background candidates in the two analyses are the same, despite the dataset being twice as large. The result of the CL_s calculation shows that the observed limit is larger than the expected limit. The previous result also saw a similar upward fluctuation so this study, while not statistically significant, hints that the true $B^0 \to \phi\phi$ branching fraction is at the level of 1×10^{-8}. This is going to

be accessible with Run 3, providing similar background rejection performance is achieved.

Chapter 9

Sensitivity to CP violation in $B_s^0 \to \phi\phi$ decays in LHCb Upgrade I

As discussed in Chapter 3, the LHCb experiment was almost entirely upgraded during the previous long shutdown of the LHC. The new LHCb experiment started taking data in 2023 at the nominal instantaneous luminosity of 2×10^{33} cm^{-2} s^{-1}. The Upgraded LHCb has a new VELO, upgraded RICH systems, a new tracking system of the silicon Upstream Tracker and Scintillating Fibre downstream tracker, and a novel, fully software triggering system [73].

The new fully software trigger is designed to increase the yield of $B_s^0 \to \phi\phi$ events by a factor of two per fb^{-1}. The $B_s^0 \to \phi\phi$ mode is a key physics channel of interest, as discussed in Chapter 2. For LHCb, this mode is known as a 'golden channel' as it is predicted to have a CP-violating phase ≈ 0 and it is a FCNC occurring at penguin level. A value of $\phi_s^{s\bar{s}s}$ that deviates significantly from zero is a signature of new physics beyond the SM. The value of $\phi_s^{s\bar{s}s}$ is measured from a time-dependent angular analysis. In order to perform this measurement, there are a few key components to be understood. These are the decay time resolution, the decay time acceptance, the angular acceptance and the flavour tagging. This Chapter presents the first studies of $B_s^0 \to \phi\phi$ in Upgrade I, showing the improved yield per fb^{-1}, the decay time acceptance, and comparisons between data and simulation in several kinematic and angular observables. The sensitivity to $\phi_s^{s\bar{s}s}$ that can be achieved in Run 3 is presented assuming similar performance in

flavour tagging and decay time resolution.

9.1 Dataset and selection

The dataset studied was taken in 2024 and corresponds to approximately 2 fb^{-1} of integrated luminosity. During this period of data-taking, the UT information was not included and the alignment of the subdetectors was preliminary. It is also not possible to refit the tracks in this dataset. The candidates are required to pass the `Hlt1TwoTrackMVA` line with a TOS decision, and are also required to pass the `Hlt2BnoC_BdsToPhiPhi` line. Several cuts are applied on the candidates at this HLT2 line. The B-meson candidate is required to have a vertex χ^2 per degree of freedom less than 10, the cosine of the PV direction angle (DIRA) greater than 0.999 and a decay time greater than 0.2 ps. The ϕ-mseon candidates are required to have a mass in the window 990 MeV/c^2 to 1050 MeV/c^2 and a vertex χ^2 per degree of freedom less than 15. The product of the ϕ meson p_T values, $p_T(\phi_1) \times p_T(\phi_2)$, must be greater than 1.5 GeV^2/c^2. The kaons are each required to have a momentum larger than 1 GeV/c, a p_T greater than 400 MeV/c and a requirement is made on the kaon PID, the difference in log likelihood of between the kaon and pion, at -5.

Data selected by the trigger is further cleaned by tightening the cut on the B-meson p_T to 2000 MeV/c, the cut on the lifetime is tightened to 0.3 ps and the maximum DOCA is required to be less than 5. The ϕ meson mass window is tightened to ± 15 MeV/c^2, and the kaon PID tightened to 0.

9.1.1 MVA for combinatorial background

In order to reduce combinatorial background, a simple MVA classifier is developed. The classifier is a gradient boosted decision tree (BDTG). The background sample for training is taken as the data sidebands, defined as 5100 MeV/c^2 $< M(K^+K^-K^+K^-) <$ 5200 MeV/c^2 or 5500 MeV/c^2 $< M(K^+K^-K^+K^-) <$5600 MeV/c^2. The signal sample for training is truth-matched signal simulation required to pass the same selections. The classifier is trained on five variables, shown in Figure 9.1. The classifier uses the kinematic variables η and p_T of the B-meson candidate and the product of the ϕ-meson p_T. The classifier additionally uses the IP χ^2 and vertex χ^2 information which shows

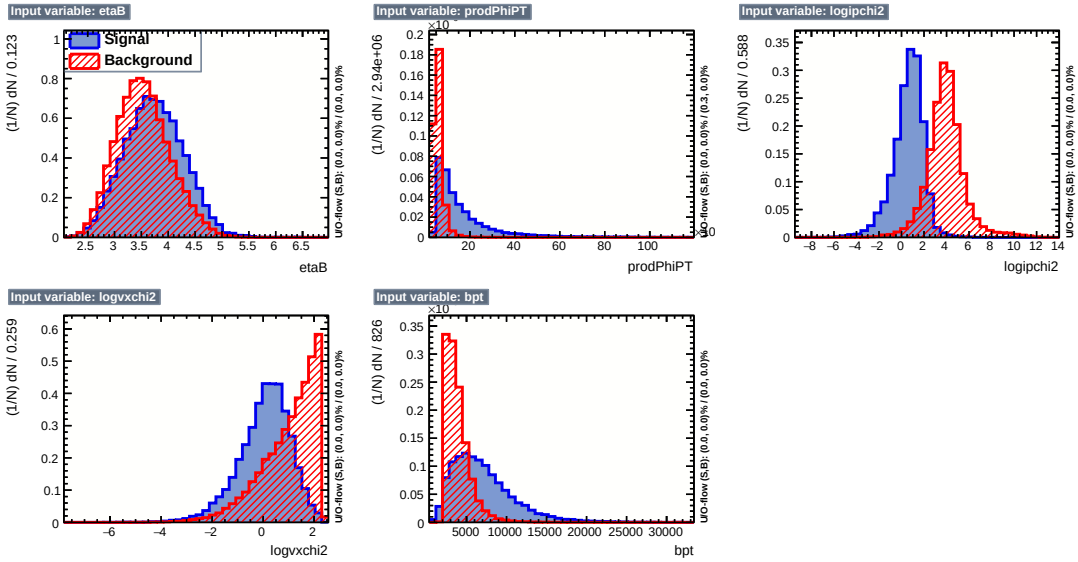

Figure 9.1 *Input variables used in the MVA classifier used to remove the combinatorial background from the 2024 data. The signal sample is represented by the solid blue histogram, with background represented by the hatched red histogram.*

good separation between signal and background.

The performance of the classifier is shown by the output classifier distributions shown on the left of Figure 9.2 and by the ROC curve on the right of Figure 9.2. The classifier distribution shows good separation between signal and background and a good agreement between the testing and training samples. The ROC curve shows good background rejection for high rate of signal efficiency.

A loose working point is chosen to retain 98.5% of signal. The candidates

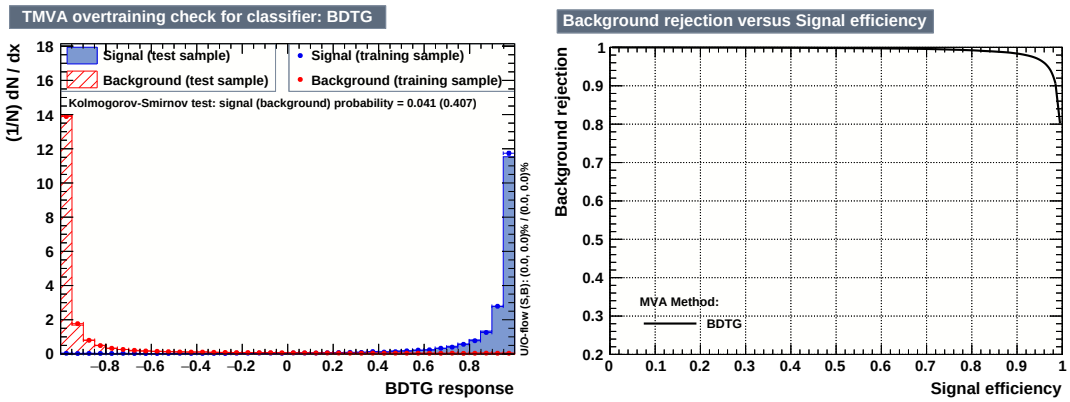

Figure 9.2 *The classifier output distribution (left) and the ROC curve (right) for the MVA classifier used to remove the combinatorial background from the 2024 data.*

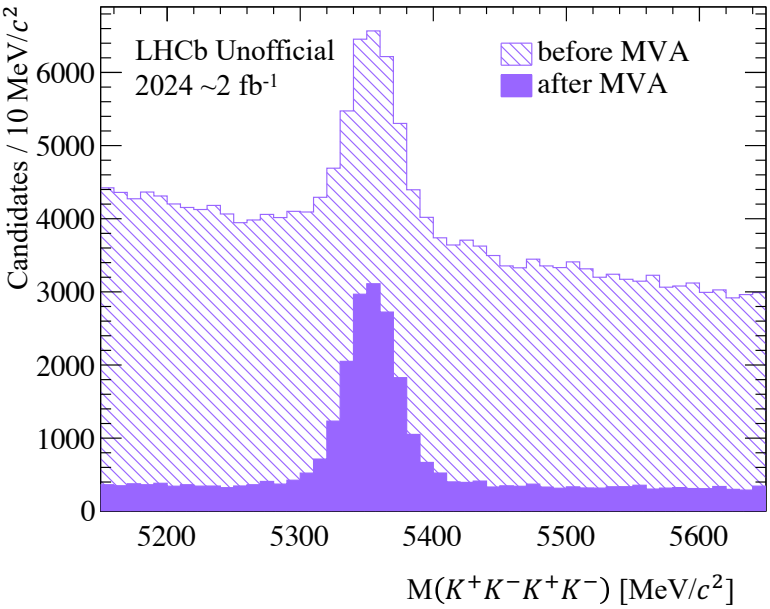

Figure 9.3 *The four-kaon invariant mass distribution before (hatched) and after (solid) applying the MVA classifier.*

remaining after applying this classifier are shown in Figure 9.3.

9.2 Comparing data and simulation

In order to develop sophisticated multivariate classifiers that work efficiently to reduce background, the simulation should describe the data well. In order to check this, signal weighted data is compared with truth-matched simulation. The signal weighted data sample is obtained using the Custom Orthogonal Weights (COWs) background subtraction method [133]. The signal weights are extracted from the data after the loose MVA cut. This is to improve the signal to background ratio without biasing the signal.

The model used for signal is the sum of a Student-T distribution and a wide Gaussian. All parameters, except for the mean and the width, are fixed to the values obtained from the fit to simulation, shown in Figure 9.4. The fitted values of the model parameters taken from MC are shown in Table 9.1. The fit to data is shown in Figure 9.5, with parameter values shown in Table 9.2. These results show that, for this dataset, the mean of the $B_s^0 \to \phi\phi$ signal distribution is shifted from the nominal B_s^0 mass of 5367 MeV/c^2 [127]. The width of the $B_s^0 \to \phi\phi$ signal peak is also significantly larger than expected from the simulation. This is due

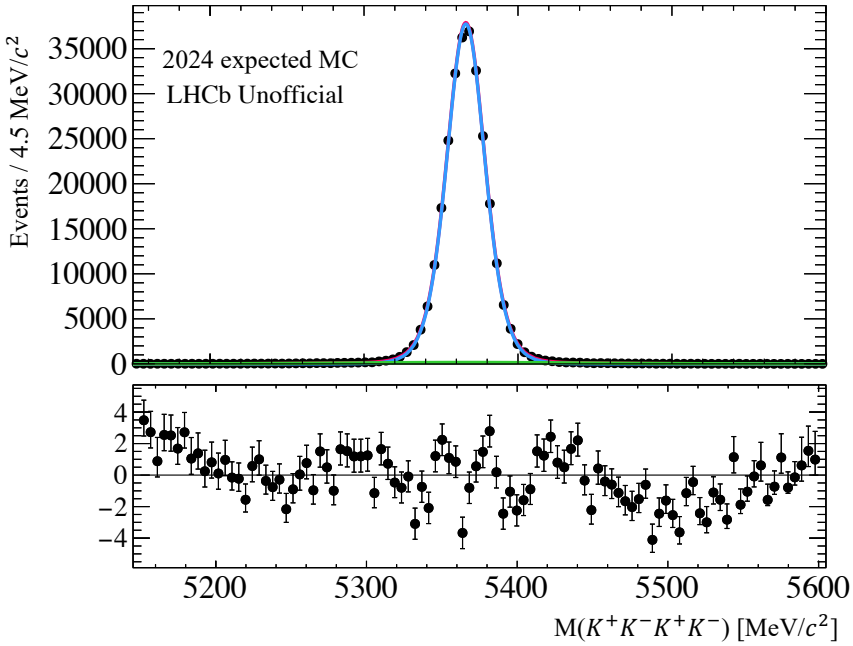

Figure 9.4 *Fit to $B_s^0 \to \phi\phi$ signal simulation used in the fit to data. The model is the sum of a Student-T distribution and a wide Gaussian. The simulated data are shown by the data points with the fit model overlaid.*

Parameter	Value
μ [MeV/c^2]	5366.13 ± 0.03
σ_{ST} [MeV/c^2]	12.63 ± 0.03
n	8.52 ± 0.17
f_{ST}	0.9764 ± 0.0006
σ_{G} [MeV/c^2]	75.2 ± 1.0

Table 9.1 *Values of fitted parameters for model of $B_s^0 \to \phi\phi$ in 2024 simulation.*

to subdetector misalignments. Despite this, it is still possible to understand the agreement between data and simulation.

A good agreement between data and simulation improves the performance of the MVA since simulation is used to define the signal in the training procedure. If the agreement is poor, the simulation does not describe the real signal well and will result in an MVA that is not as performant. It can be seen in Figure 9.6 that the transverse momentum, p_T, of the B_s^0 meson does not agree well with the data, but the discrepancy is similar to what was observed in Run 2.

The value of the CP-violating phase is extracted from a 4D fit to the three helicity angle distributions and the decay time distribution, and so the simulation should

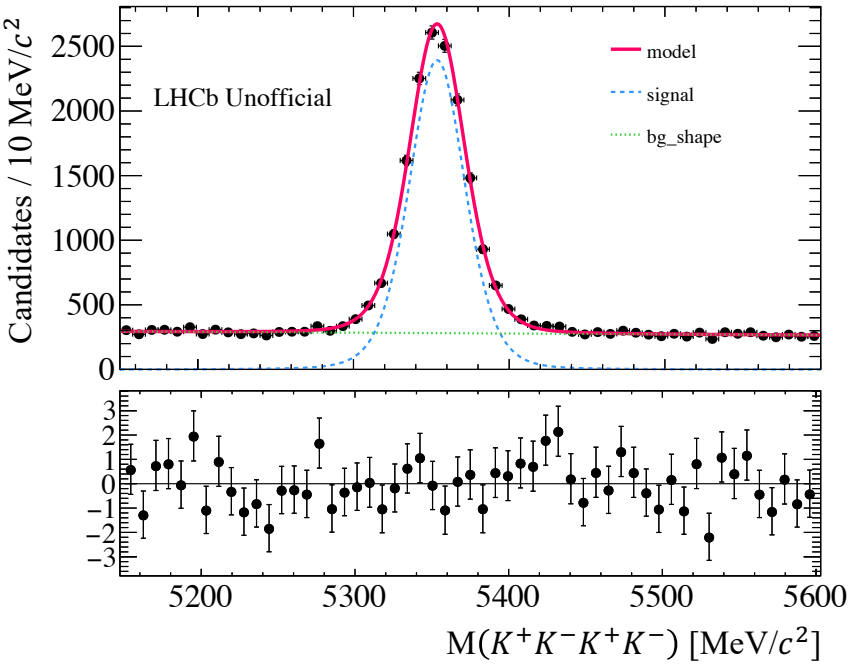

Figure 9.5 *Fit to $B_s^0 \to \phi\phi$ candidates in 2024 data used to extract signal weights. The signal model is the sum of a Student-T distribution and a wide Gaussian and the background is modelled by an exponential.*

Parameter	Value
μ [MeV/c^2]	5353.7 ± 0.2
σ_{ST} [MeV/c^2]	18.2 ± 0.2
$\tau_{\text{background}}$	$(22.5 \pm 6.3) \times 10^{-5}$
$N_{B_s^0 \to \phi\phi}$	13963 ± 143
$N_{\text{background}}$	15395 ± 148

Table 9.2 *Results of fit to $B_s^0 \to \phi\phi$ candidates in 2024 data.*

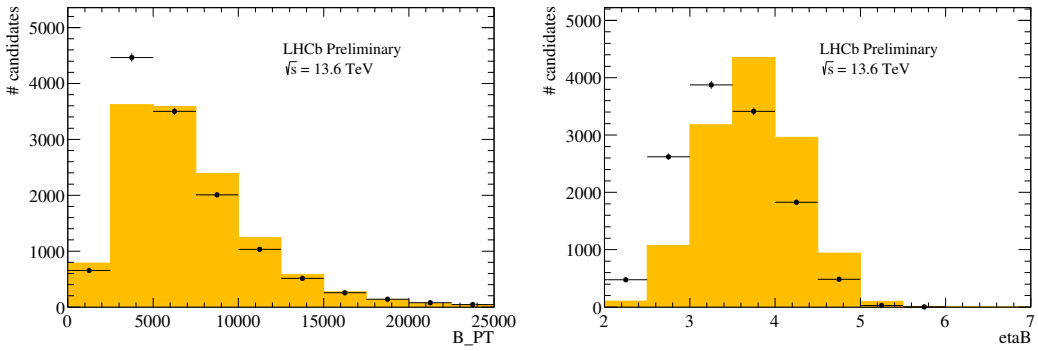

Figure 9.6 *Distributions of B_s^0 meson p_T and η for data (black points) and simulation (solid yellow). Data has been signal weighted using the COWs method to extract a signal-only sample.*

model these distributions well. The helicity angles, defined in the rest frame of the B_s^0 meson, are described in Section 2.4.2. Figure 9.7 shows reasonable agreement is seen between data and simulation, particularly in the B_s^0 decay time. Calculated from the helicity angles, good agreement is also seen in triple product variables U and V, shown in Figure 9.8. To improve agreement, simulation samples are to be reweighted to better match the distribution seen in data and further work is required to control and carefully model background contributions.

9.3 Decay time acceptance

Since CP-violation in $B_s^0 \to \phi\phi$ is measured in a time-dependent fit, it is crucial to understand how the acceptance of LHCb affects the measured decay time distribution of $B_s^0 \to \phi\phi$ candidates. This can be understood by fitting the decay time distribution of simulated events to a model where the usual exponential decay time model is multiplied by an acceptance function. In these studies, a dedicated simulation sample is generated where the difference between the heavy and light lifetimes, $\Delta\Gamma_s$, is fixed to zero. This simplifies the model to a single exponential with the lifetime of 1.512 ps. The simulated events that pass selections and are within the LHCb acceptance are modelled with the product of an exponential, fixed to the generated lifetime, and the following acceptance function,

$$f(t;\beta,z,\gamma) = \frac{1-\beta t}{1+(zt)^{-1}}, \tag{9.1}$$

where β,z and γ are free parameters in the fit. The fit to simulation is shown in Figure 9.9 alongside the fitted acceptance function. The values of the fit

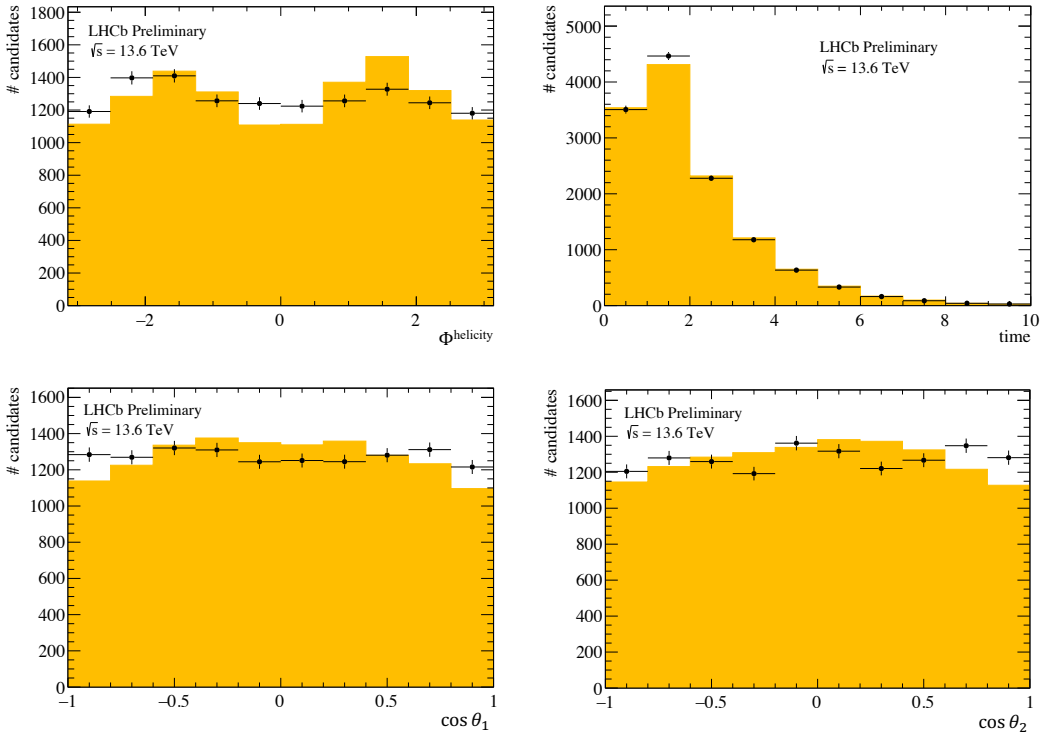

Figure 9.7 *Distributions of B_s^0 meson helicity variables and decay time for data (black points) and simulation (solid yellow). Data has been signal weighted using the COWs method to extract a signal-only sample.*

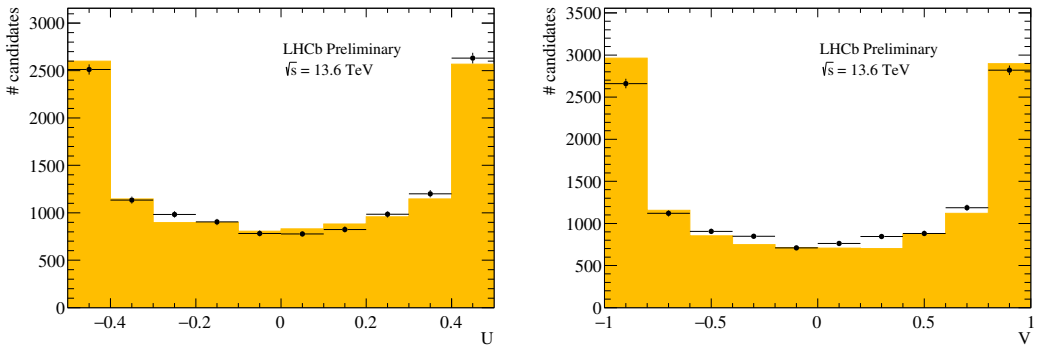

Figure 9.8 *Distributions of B_s^0 meson triple product variables for data (black points) and simulation (solid yellow). Data has been signal weighted using the COWs method to extract a signal-only sample.*

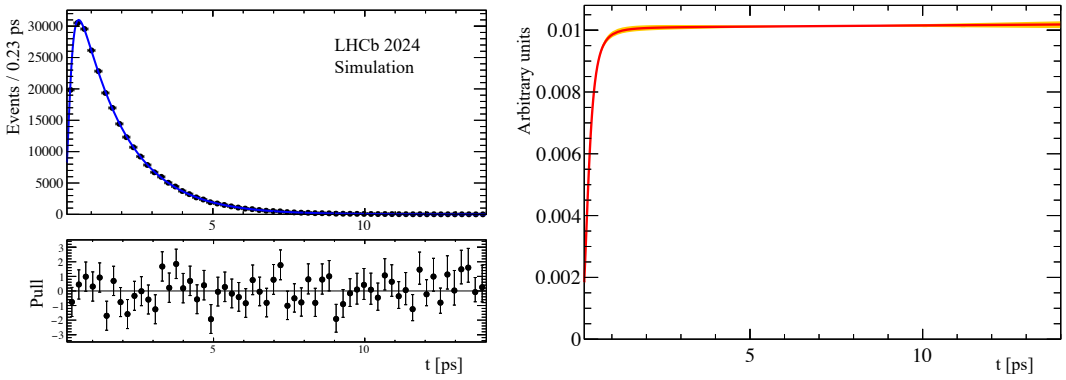

Figure 9.9 *Simulated decay time with fit model overlaid (left) and the extracted decay time acceptance (right).*

Parameter	Value
β	$(-7.3 \pm 15.7) \times 10^{-4}$
z	3.16 ± 0.02
γ	3.24 ± 0.05

Table 9.3 *Results of fit to $B_s^0 \to \phi\phi$ decay time distribution.*

parameters are shown in Table 9.3.

9.4 Sensitivity to $\phi_s^{s\bar{s}s}$ in LHCb Run 3

Using the results of the fit to data in Figure 9.5, the expected Run 3 yield of $B_s^0 \to \phi\phi$ candidates can be extracted. This data corresponds to approximately 2 fb^{-1} and yield per fb^{-1} of 6485 $B_s^0 \to \phi\phi$ candidates is calculated from the sum of signal weights. The analysis of Run 2 data finds a signal yield of 15840 ± 140 events, which corresponds to a yield per fb^{-1} of 2640 events [42]. The projected data sample that LHCb could collect in Run 3 is 25 fb^{-1}. This would correspond to around 160,000 $B_s^0 \to \phi\phi$ candidates, more than a factor of 10 increase on the Run 2 data sample. Scaled by statistics as $1/\sqrt{N}$, this would give a sensitivity of $\phi_s^{s\bar{s}s}$ of 23 mrad. This scaling assumes a similar performance will be achieved in timing resolution and in tagging the flavour of the B_s^0 meson.

9.5 Results and outlook

These studies show promising results for studies of $B_s^0 \to \phi\phi$ in Run 3 of the LHCb experiment. The yield per fb^{-1} has increased in line with expectations set when designing LHCb Upgrade I. The agreement between data and simulation is good for the very early stages of data taking, and at a level comparable to Run 2 in the kinematic variables. The decay time acceptance is modelled and is close to flat. These results show a competitive measurement of TPAs may be measured with early Run 3 data, and a full analysis of Run 3 data could yield a sensitivity of 23 mrad on $\phi_s^{s\bar{s}s}$. For the full analysis, further studies will need to be done to improve agreement between data and simulation and take into account contamination from peaking backgrounds. The angular acceptances will need to be modelled and, for the full time-dependent analysis, the timing resolution and flavour tagging will need to be carefully calculated and calibrated.

Chapter 10

Scoping of LHCb Upgrade II

The LHCb Upgrade II is due to be installed in 2033, during LS4 of the LHC [146]. It will operate in the HL-LHC era of the LHC, where the instantaneous luminosity delivered to LHCb will be 1.3×10^{34} cm^{-2}s^{-1}. This is a factor of 10 larger than the luminosity during Upgrade 1. During this phase, it is anticipated that an integrated luminosity of ~ 300 fb^{-1} will be delivered to LHCb.

The order of magnitude increase in instantaneous luminosity means the number of visible pp interactions per bunch crossing will be around 40 [147]. Reconstruction of the charged tracks and vertices will therefore be more challenging, and three methods to alleviate this are proposed [148]. These are; increasing detector granularity, reducing the detector material and exploiting precision timing [148].

Adding timing information is a crucial element, in particular for the VELO in Figure 10.1. In the right of the image, we see the charged tracks from 42 collisions in one bunch crossing. On the right, we see the visible interactions and tracks in a 20 ps window. It can therefore be seen that being able to include timing information so tracks may be separated in time as well as space will provide a much cleaner environment to search for tracks and reconstruct primary vertices.

To perform studies of momentum resolution and acceptance in a variety of cases, it is useful to have access to simulated decays readily. For this, the RapidSim fast simulation package [116] is used with custom models of momentum smearing. To smear the momentum, the covariance matrix of the Upgrade II Kalman filter is required and so a tool has been developed that performs the Kalman fit on full Upgrade II MC [149, 150]. By specifying the number and positions of

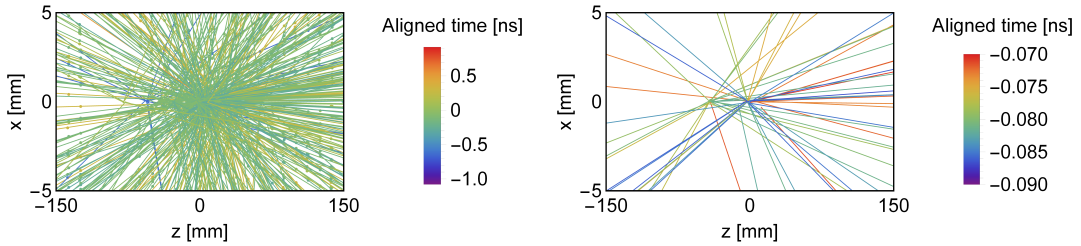

Figure 10.1 *Demonstration of pile-up in the VELO in Upgrade II conditions. On the left, the plot shows the charged tracks during one bunch crossing with 42 interactions. On the right, we see a 20 ps window of the same bunch crossing which demonstrates the power of precision timing in these higher pile-up bunch crossings. Source: the LHCb Collaboration [147]*

tracking layers, the pixel pitch and magnet model, a specific configuration of LHCb Upgrade II is built and the momentum resolution of this configuration is determined from the Kalman filter. The momentum resolution calculated for each specification is passed as a smearing term in RapidSim to generate realistic Upgrade II simulation for a variety of detector configurations in a reasonable timeframe.

Once a reasonable simulation is generated for each scenario, the positions of the particle tracks at the Mighty Tracker stations must be understood to be able to calculate the efficiency of reconstructing all four tracks in a descoped option. To do this, the momentum change due to the magnet is modelled as a single kick, shown in Figure 10.2. Full simulation from Run 2 is used to parameterise the kick of the magnet with the track slope. This is then used to calculate the momentum of the track after it has passed through the magnet, and to calculate the position at the downstream tracking stations.

10.1 Tracking in Upgrade II

To mitigate the larger pile-up and multiplicity expected in the HL-LHC conditions, the tracking systems have been redesigned to increase granularity, include timing information to the track hits, and reduce the material. The requirements are that the momentum resolution is between 0.5% and 1% at 200 GeV/c, the precision on the impact parameter is ≈ 25 µm, the material budget cannot exceed 0.5 (0.2) radiation (interaction) lengths, and the efficiency of reconstructing long tracks much exceed 95% with a ghost rate below 10% [147]. The proposed tracking

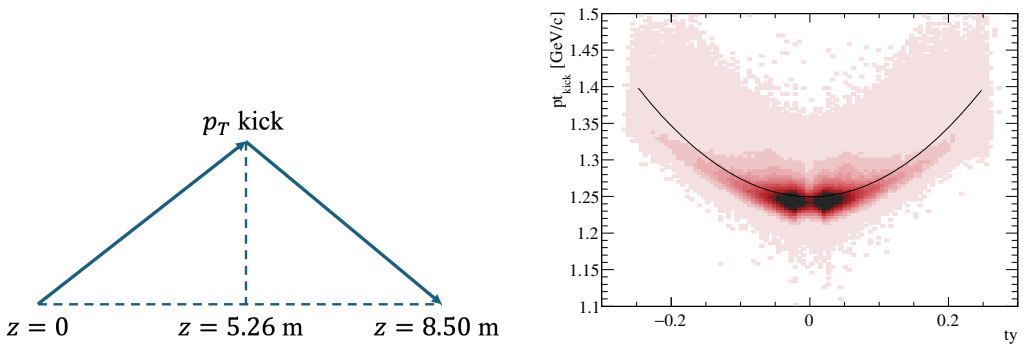

Figure 10.2 *The single p_T kick model of the LHCb magnet. The left shows a diagram of how the track is modelled with a single kick. On the right the plot shows the kick in p_T as a function of the track slope t_y from Run 2 simulation.*

solution in LHCb Upgrade II is shown in Figure 10.3. Upstream of the magnet, there is the VELO and UP (a pixel tracking detector replacing the current UT), with the Mighty Tracker (composed of fibre and pixel trackers) tracking stations downstream. There is also the inclusion of tracking stations within the magnet.

10.1.1 The VELO

The VELO is one of the most crucial instruments in LHCb as it provides primary and secondary vertex reconstruction. In Upgrade II, it follows a similar layout as the original and Upgrade I versions as described in Section 3.3 but the technology is modified to withstand new HL-LHC conditions [146]. Many technologies are being considered for the Upgrade II VELO, with a target timing resolution of 35 ps [147]. The baseline for the Upgrade II VELO, shown in Figure 10.4, uses 32 modules covering the pseudorapidity range $2.0 < \eta < 4.8$. Each station has a thickness of 150 µm and spatial resolution of 10 µm. The RF shielding is redesigned to be cylindrical with a thickness of 75 µm. In light of the studies presented in this Chapter, a `Middle` and a `Low` descoped option is chosen. In a `Middle` scenario, a lower instantaneous luminosity allows for cost-saving with fewer read-out boards. In the `Low` scenario, the first two and last two stations are removed, reducing the inner acceptance to $\eta < 4.7$, a thicker and corrugated RF foil is used, and the material budget is doubled due to a heavier cooling substrate.

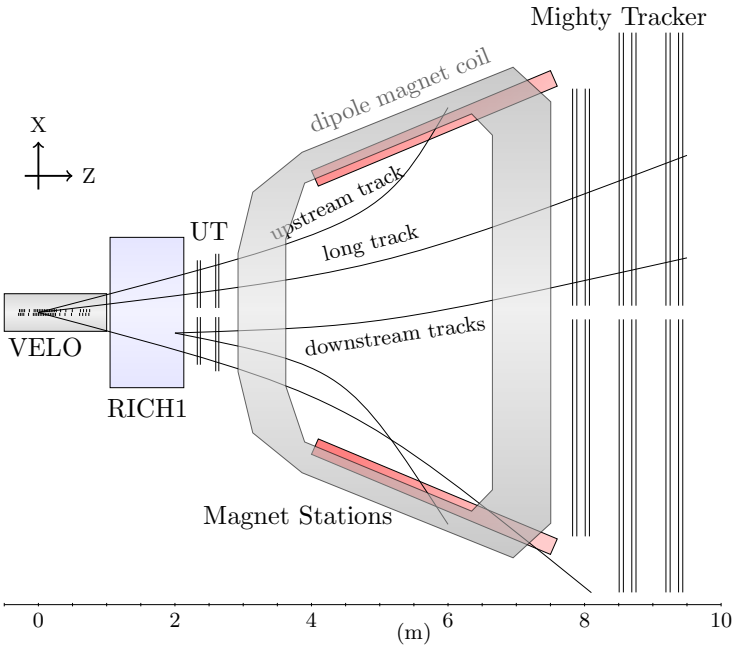

Figure 10.3 *Types of tracks reconstructed at LHCb and the proposed Upgrade II tracking stations.*

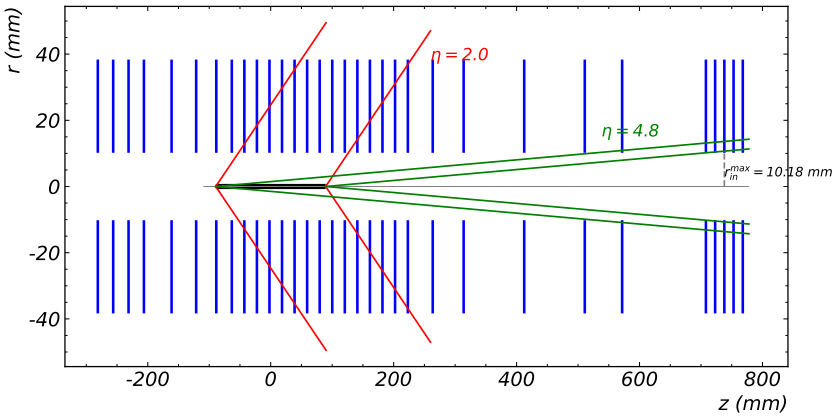

Figure 10.4 *Layout of modules in* `Baseline` *and* `Middle` *VELO scenarios. For the* `Low` *scenario, the first and last two modules are removed, reducing the inner acceptance. Source: LHCb Collaboration*

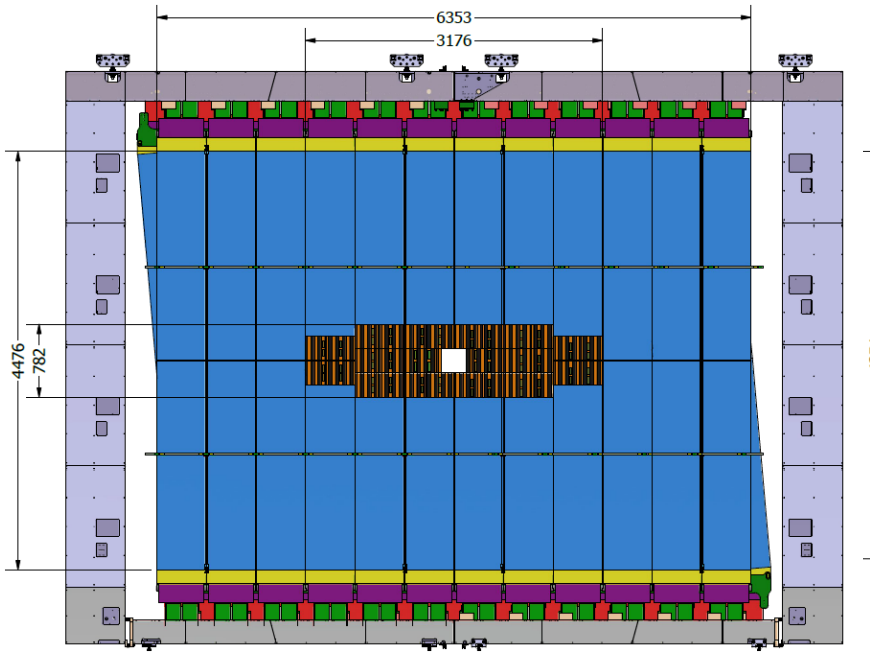

Figure 10.5 *The baseline design for the Mighty Tracker. The inner region shows the Mighty-Pixel detector, wth the blue outer region showing the acceptance of the Mighty-SciFi fibre tracker.*

10.1.2 The Mighty Tracker

The Mighty Tracker (MT) is the proposed upgrade for the downstream tracking stations [146]. It will adopt the current Scintillating Fibre (SciFi) technology for the outer acceptance, with the inner regions covered by HV-CMOS silicon pixel sensor modules [151]. These are referred to as Mighty-SciFi and Mighty-Pixel respectively. The Mighty-Pixel will provide higher granularity in the inner regions and provide precise timing. An important consideration for the final design of the Mighty Tracker is the size of the inner region to be covered by silicon sensors and the outer acceptance as these drive the cost of the subdetector. Studies have been performed to demonstrate what can be achieved in various funding scenarios. The following sections describe the effect of the reducing outer acceptance on signal efficiency of various key decay channels, and the effect of the silicon acceptance on the $B^0_{(s)}$ meson mass resolution in the $B^0_{(s)} \to \phi\phi$ channels. Since the Framework Technical Design Report (FTDR) [146], studies have shown the coverage required from the Mighty-Pixel can be reduced with no real impact on performance. The current baseline for the detector is shown in Figure 10.5. In the `Middle` scenario, the Mighty-Pixel region is reduced in size and the Mighty-SciFi modules are each shortened by 10 cm. In the `Low` scenario, shown in Figure 10.6, the width of the

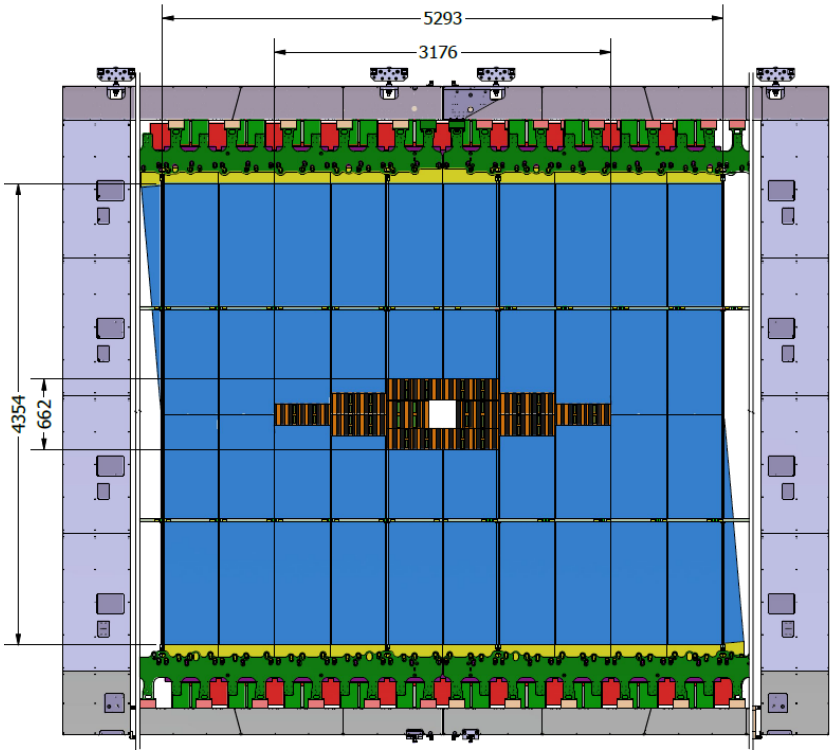

Figure 10.6 *The* `Low` *design for the Mighty Tracker with reduced Mighty-Pixel and shorter Mighty-SciFi modules as in the* `Middle` *scenario, with a further cost saving achieved by removing Mighty-SciFi modules from each side of the detector.*

detector is reduced by removing one Mighty-SciFi module from each side.

10.2 Studies of Upgrade II acceptance

The following studies were performed to understand the impact of the changes in acceptance in each of the `Middle` and `Low` scenarios on some key modes for LHCb.

10.2.1 Inner acceptance

A crucial consideration for the design is the inner acceptance of the detector. This is particularly important for the VELO which has to close very tightly around the interaction point to be able to reach the high η coverage that makes LHCb unique. It is important to understand the interplay of the inner acceptances of the tracking stations upstream of the magnet and those downstream. Since there

	Baseline	Middle	Low
$\mathcal{L}$ (10^{34} cm^{-2}s^{-1})	1.5	1.3 or 1.0	1.0
VELO	nominal	nominal	first and last two two modules removed
Mighty-Pixel	nominal	reduced coverage	reduced coverage
Mighty-SciFi	nominal	modules shortened	modules shortened and module removed per side

Table 10.1 *Summary of descoping scenarios for the instantaneous luminosity, $\mathcal{L}$, the VELO and the Mighty Tracker*

are mechanical constraints and safety limits on the size of the beam pipe hole at the tracking stations, this limits the usefulness of a tight inner acceptance at the VELO stage.

Assuming a baseline Mighty Tracker outer acceptance and not accounting for the VELO inner acceptance, simulated samples of $B_s^0 \to \phi\phi$ and $B_s^0 \to \mu^+\mu^-$ are generated. To understand the effect of enlarging the hole in the centre of the Mighty Tracker for the beam pipe, the selection efficiency is calculated by requiring that all final state tracks lie within the detector, outside of the beam pipe region. The denominator of this efficiency is the number of simulated events that lie within the acceptance assuming there is no beam pipe hole,

$$\epsilon = \frac{N_{\text{beampipe: } x \text{ cm}}}{N_{\text{no beampipe hole}}} \tag{10.1}$$

where x is the width of the square region left clear for the beampipe. The values considered for x are 20, 22, 24 and 26 cm. The efficiency is calculated in bins of pseudorapidity at production and are shown in Figures 10.7 and 10.8 for $B_s^0 \to \phi\phi$ and $B_s^0 \to \mu^+\mu^-$ respectively. This study shows that the Mighty-Pixel hole defines the detector acceptance. The original VELO covered up to an η of 5, but the construction of the Upgrade II VELO with coverage above $\eta = 4.8$ is difficult. Figures 10.7 and 10.8 show that many of these tracks have poor efficiency due to the MT beam pipe hole and so it does not make sense to push for coverage greater than this. This has set the inner acceptance of the VELO in the baseline and descoped scenarios.

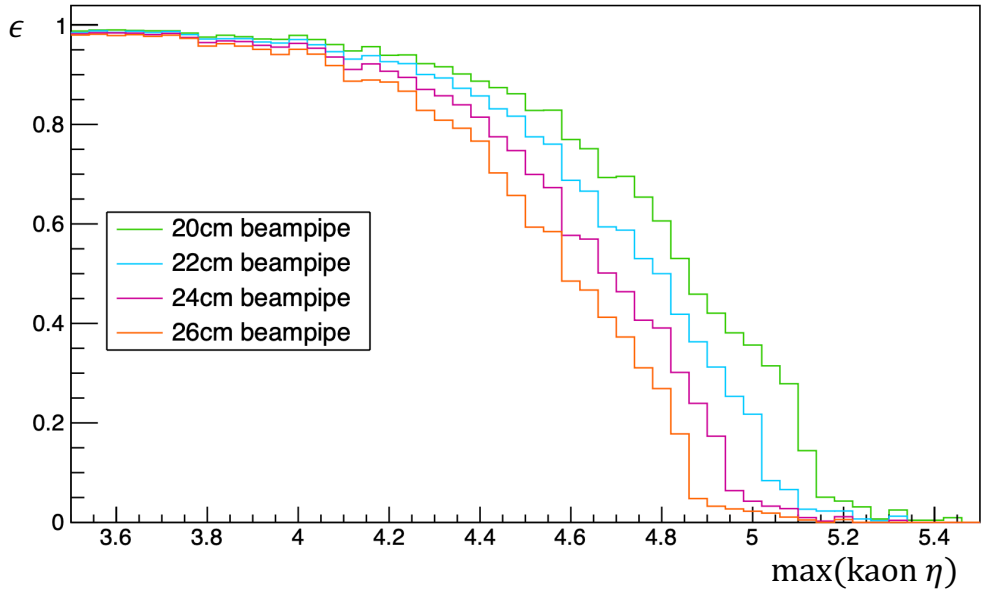

Figure 10.7 *Studies of Mighty Tracker geometric acceptance efficiency in* $B_s^0 \to \phi\phi$.

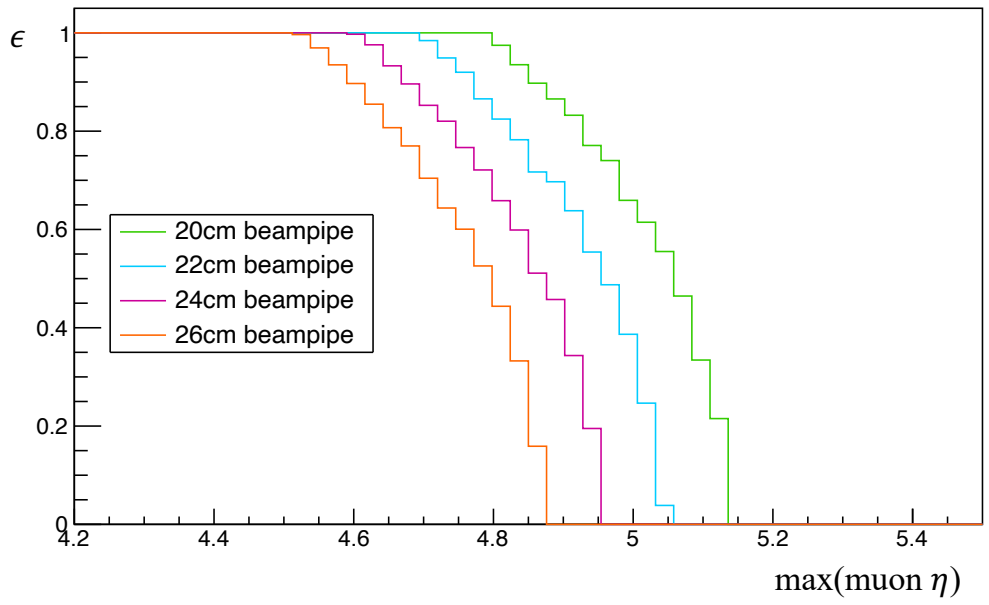

Figure 10.8 *Studies of Mighty Tracker geometric acceptance efficiency in* $B_s^0 \to \mu^+\mu^-$.

MT Geometry	baseline VELO efficiency (%)	reduced VELO efficiency (%)
nominal	-	99.05 ± 0.05
short	99.40 ± 0.04	98.46 ± 0.06
narrow	92.04 ± 0.13	91.14 ± 0.13
narrow and short	91.49 ± 0.13	90.60 ± 0.14
staggered	99.59 ± 0.03	98.65 ± 0.05

Table 10.2 *For $B_s^0 \to \phi\phi$ in nominal and reduced VELO scenarios, the coverage with respect to the nominal arrangement (13cm beampipe) is shown as a percentage.*

10.2.2 Outer acceptance

Four scenarios were proposed to reduce the outer acceptance of the Mighty Tracker to reduce the cost with small loss to physics performance. These options are; removing one SciFi module from each side of the detector, reducing the heights of the SciFi modules, manufacturing all SciFi modules to be the same height to form a staggered detector, and the combination of a reduced height and the removal of a module on each side. These options are shown in Figure 10.9. To understand the effect of these changes, full simulation samples of $B_s^0 \to \phi\phi$, $B_s^0 \to \mu^+\mu^-$ and $D_s \to K_S\pi^+\pi^-$ decays are generated in a nominal (`Baseline` and `Middle`) VELO scenario or a reduced (`Low`) VELO scenario. Using the single momentum kick model of the magnet the track positions at the tracking stations are calculated. These track positions are then used to calculate the efficiency of retaining tracks in each of the reduced scenarios. Tables 10.2, 10.3 and 10.4 show the results for $B_s^0 \to \phi\phi$, $B_s^0 \to \mu^+\mu^-$ and $D_s \to K_S\pi^+\pi^-$ modes respectively. It is clear that making the Mighty Tracker narrower is the worst in terms of efficiency, with staggered or short options providing reduced areas, and therefore cost, while retaining high efficiency. In light of this work, the short option is chosen as the `Middle` descoped option, with the narrow and short option chosen as the `Low` descoped option. The staggered option gives high efficiency, but in reality this would be mechanically very difficult to construct and so is not considered.

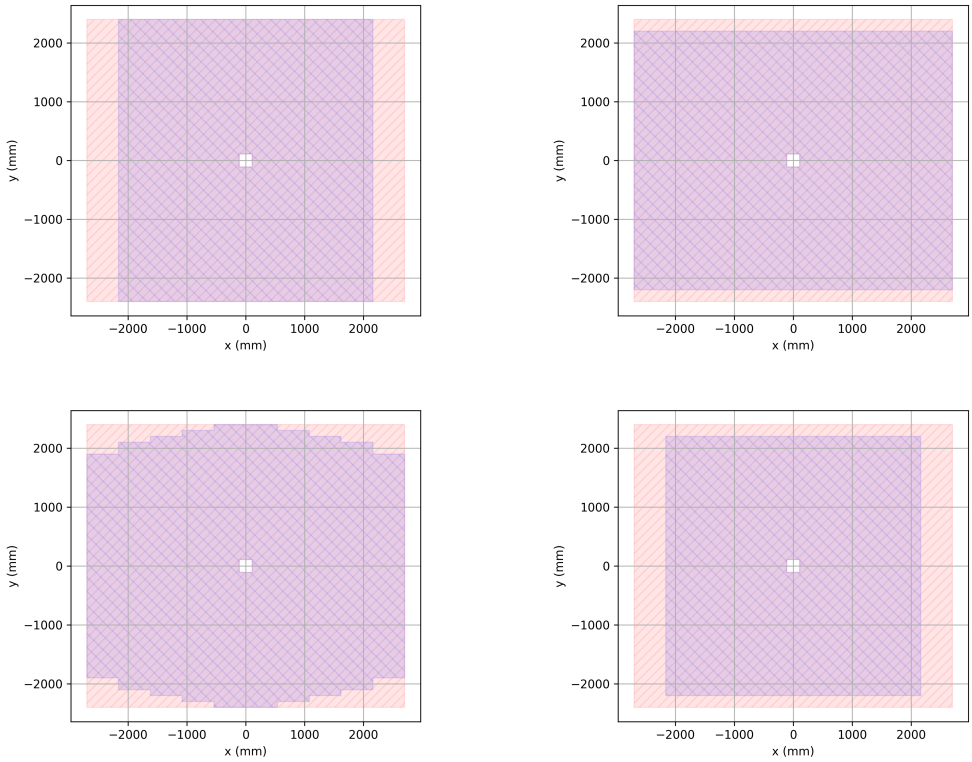

Figure 10.9 *The four options for descoping the outer acceptance of the MT. The red upwards-hatched shape represents the size of the nominal MT, and the blue downward-hatched shape represents the descoping option. From left to right then top to bottom: removal of SciFi modules from the sides, shortening of all SciFi modules, staggering identical SciFi modules around the silicon, and shortening of all SciFi modules and removal of SciFi modules from the sides.*

MT Geometry	baseline VELO efficiency (%)	reduced VELO efficiency (%)
nominal	-	98.92 ± 0.04
short	99.33 ± 0.03	98.25 ± 0.05
narrow	97.15 ± 0.07	96.09 ± 0.08
narrow and short	96.50 ± 0.07	95.44 ± 0.08
staggered	99.81 ± 0.02	98.72 ± 0.04

Table 10.3 *For $B_s^0 \to \mu\mu$ in nominal and reduced VELO scenarios, the coverage with respect to the nominal arrangement (13cm beampipe) is shown as a percentage.*

MT Geometry	baseline VELO efficiency (%)	reduced VELO efficiency (%)
nominal	-	91.2 ± 0.6
short	99.7 ± 0.1	90.9 ± 0.5
narrow	93.2 ± 0.5	84.4 ± 0.8
narrow and short	92.9 ± 0.5	84.1 ± 0.8
staggered	99.7 ± 0.1	90.8 ± 0.6

Table 10.4 *For $D^0 \to K_S\pi^+\pi^-$ in nominal and reduced VELO scenarios, the coverage with respect to the nominal arrangement (13cm beampipe) is shown as a percentage.*

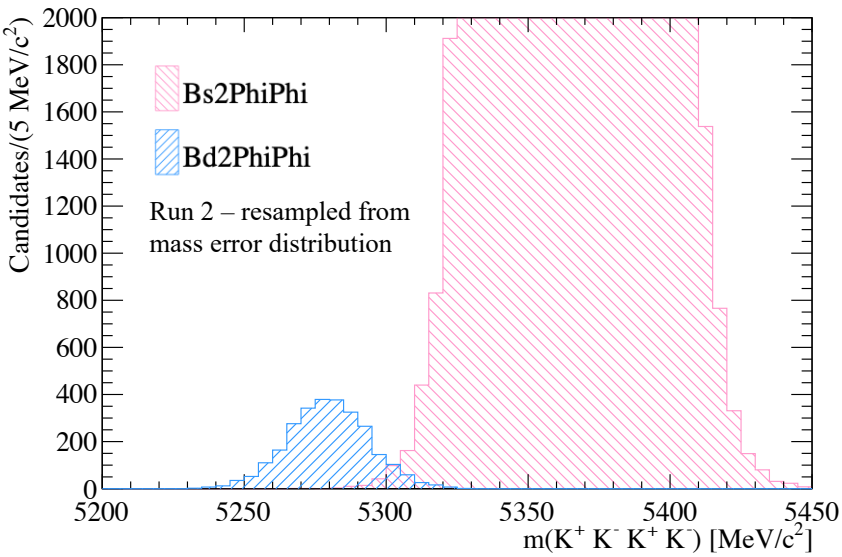

Figure 10.10 *$B_s^0 \to \phi\phi$ and $B^0 \to \phi\phi$ peaks, resampled from mass error distributions. Produced using Run 2 MC samples.*

10.3 Studies of mass resolution in Upgrade II

The resolution of the $B^0_{(s)}$ mass in Upgrade II is of importance as a metric to understand the LHCb detector performance, but also for the search of $B^0 \to \phi\phi$ decays. The mass splitting between B^0 and B^0_s mesons is measured to be 86.22 ± 0.16 MeV/c^2, so improvement in the mass resolution is of importance when resolving the individual B^0_s and B^0 peaks. This can be seen in Figure 10.10, which shows $B^0_s \to \phi\phi$ and $B^0 \to \phi\phi$ peaks that have been resampled from the mass error distributions of Run 2 simulation samples. Using the fast simulation, the change in mass resolution in the upgrade scenarios is studied. One million $B^0_s \to \phi\phi$ events are generated in each of four scenarios: the Run 2 scenario, the Run 3 Upgrade I scenario, a modest Upgrade II scenario with four UP layers, and a nominal Upgrade II scenario with three UP layers. Kinematic selections

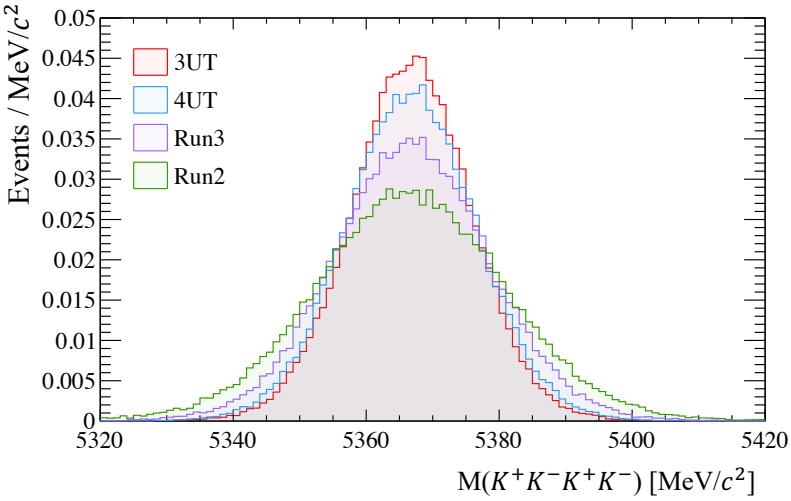

Figure 10.11 *Plot showing comparison of $B_s^0 \to \phi\phi$ mass distributions in Run 2, Upgrade I and Upgrade II scenarios. In the Upgrade I scenario, a Run 3 momentum smearing is assumed. The Upgrade II scenarios are a UP with 4 layers with a modest Mighty Tracker and UP with 3 layers with a nominal Mighty Tracker.*

are applied to each sample. For each kaon track, the transverse momentum must be greater than 400 MeV/c. The four kaon tracks must have pseudorapidity in the range 2 to 5 and must all lie within the nominal acceptance of the Mighty Tracker, as described in Section 10.2. For the ϕ mesons, the mass must be within 25 MeV/c^2 of the measured mass, and the product of the transverse momentum of each ϕ meson must be greater than 1.5 GeV$^2/c^2$. This emulates the requirements of the Run 3 HLT2 trigger line for $B_s^0 \to \phi\phi$ events. With these kinematic selections, the four-kaon invariant mass spectrum is plotted for each sample, seen in Figure 10.11. Each of these distributions is fit to the sum of two Gaussians to and a value for the width, σ_{total}, calculated as

$$\sigma_{\text{total}} = \sqrt{f_1\sigma_1^2 + f_2\sigma_2^2} \tag{10.2}$$

where $f_{1,2}$ are the fractions multiplying each of the two Gaussians, each with width $\sigma_{1,2}$. These results are shown in Table 10.5. A 23% improvement is seen in mass resolution from the Upgrade I Run 3 scenario to a nominal MT scenario with 3 UP layers. This is improvement reduced to a 17% improvement if a modest MT scenario with 4 UP layers is considered. This is due to the additional UP material.

In the context of the study of $B^0 \to \phi\phi$, the separation between the B^0 and B_s^0 peaks in Upgrade I and in a modest Upgrade II scenario with 4 UP layers is shown

Sample	Width (MeV/c^2)
Run 2	14.54 ± 0.06
Run 3	11.86 ± 0.06
Modest MT, 4 UP layers	9.88 ± 0.10
Nominal MT, 3 UP layers	9.14 ± 0.05

Table 10.5 *Mass resolutions for Run 2, Upgrade I and Upgrade II scenarios. Calculated from a fitting the distributions shown in Figure 10.11 to the sum of two Gaussian distributions.*

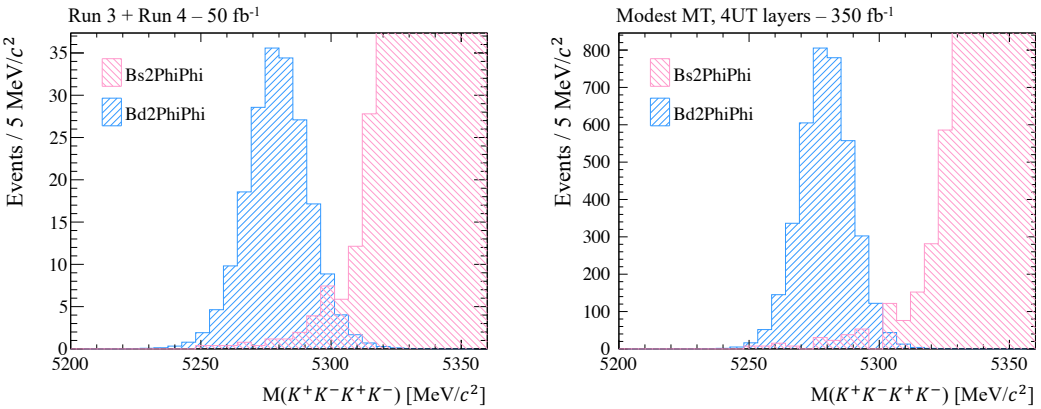

Figure 10.12 *Mass distributions for $B^0_{(s)} \to \phi\phi$ events in Upgrade I and Upgrade II with a modest MT and 4 UP layers. The yields are scaled to represent the anticipated data collection for each era of LHCb. The samples are smeared to represent kaon interaction events, with the rate of these events assumed to be the same as in Run 1 and 2.*

in Figure 10.12. To construct the $B^0 \to \phi\phi$ shape, the $B^0_s \to \phi\phi$ events have been shifted down by the known $B^0_s - B^0$ mass splitting [127], normalised to the rate expected by considering a $B^0 \to \phi\phi$ branching fraction equal to 1.2×10^{-8}, and assuming the efficiency of selecting $B^0_{(s)} \to \phi\phi$ candidates is the same in Upgrade I and Upgrade II. The samples have been tuned to include a tail component that arises from kaon interactions assuming the same level as Run 2. The rate of these events and their mass resolution are taken from Run 2 simulation samples of kaon interaction events. These samples were used for the $B^0 \to \phi\phi$ study in Chapter 4. To add the interaction component to the Upgrade I and II samples, the rate of interaction events is assumed to remain the same as in Run 1 and 2 and it is assumed that they can be removed with the same efficiency as in the Run 1 and 2 analysis.

From these studies, a good separation in the $B^0 \to \phi\phi$ and $B^0_s \to \phi\phi$ signals is achieved, and the Upgrade II scenario has an improved overlap in these two

distributions even in the case of a modest MT. Further studies of the rare modes $B^0_{(s)} \to \mu\mu$ have been performed and are detailed in Appendix E.

Chapter 11

Conclusions

This thesis presents a series of studies on the charmless decay modes $B^0 \to \phi\phi$ and $B_s^0 \to \phi\phi$ with the LHCb Experiment. Using the full Run 1 and Run 2 datasets, a search was performed to find evidence for the rare mode $B^0 \to \phi\phi$. Using a suite of advanced background rejection techniques, the search presented is the most sensitive search to date. No significant signal is seen, therefore a limit is set on the branching fraction at 1.3×10^{-8} and 1.4×10^{-8} at 90% and 95% confidence level respectively. This is the most stringent limit set on this mode to date. These results agree with the SM and favour a limit at the low end of the predictions.

This new limit has implications for models of particle physics beyond the Standard Model, in particular models of R-parity-violating SUSY. Since the $B^0 \to \phi\phi$ branching fraction can be enhanced in R-parity-violating SUSY models, the result of the search for $B^0 \to \phi\phi$ will allow theorists to put new bounds on these models.

With this limit on the branching fraction in the range of the SM theory predictions, it is expected that the statistics obtained by LHCb in Run 3 and Run 4 should be enough to obtain evidence for this decay mode providing the same sensitivity can be achieved. The sensitivity that can be achieved in Upgrade I is dependent on quality and variety of information that is made available to analysts about the events that are stored. It is only with a plethora of event information that is well-described by simulation that high-level background rejection techniques, like those presented in this thesis, may be developed.

A study of early LHCb Run 3 data is also performed. This shows the significant

boost in trigger efficiency for $B_s^0 \to \phi\phi$ events gained by removing the L0 trigger. More work is still to be done on fully understanding the detector in Run 3, but it expected that a competitive measurement of TPAs in $B_s^0 \to \phi\phi$ can be made with data collected in 2024 alone. A sensitivity of 23 mrad on the CP-violating phase $\phi_s^{s\bar{s}s}$ is possible with the projected 25 fb^{-1} data sample from Run 3, given that the time resolution and flavour tagging can achieve similar performance as in Run 2. The Upgrade I era of LHCb promises to provide many world's best measurement of CP violation and other observables in charmless modes such as $B_s^0 \to \phi\phi$.

Further into the future, LHCb will be upgraded again for the high-luminosity LHC. Studies are presented to show the effect of varying the acceptance of the proposed subdetectors. The decision is made to reduce the inner acceptance of the VELO and Mighty Tracker to save costs, while retaining good selection efficiency for the most crucial channels for LHCb. Four options for the outer acceptance of the Mighty Tracker have been studied to allow for varying degrees of cost saving.

The study of charmless B-decays provides an excellent laboratory to explore the most curious puzzles in the Standard Model. There are no significant BSM signatures yet, but by continuing the studies of $B_s^0 \to \phi\phi$ and $B^0 \to \phi\phi$ into both the Upgrade I and Upgrade II eras of LHCb then the Standard Model can be further constrained. With the greater statistics and precision promised by the future of LHCb, the effects of new physics may be realised.

Appendix A

Mass models

A.1 The Student-T distribution

The Student-T distribution arises as a weighted mixture of an infinite number of Gaussians, all with common mean μ. It has the form

$$P(x|\mu, s, n) = \frac{1}{Z} \frac{1}{(1 + (x-\mu)^2/(ns^2))^{(n+1)/2}}$$

where the normalization parameter

$$Z = \sqrt{\pi n s^2} \frac{\Gamma(n/2)}{\Gamma((n+1)/2)},$$

n is the number of degrees of freedom and Γ is the gamma function. For $n > 1$ the distribution has mean μ. If $n > 2$ then the distribution has a finite variance given by

$$\sigma^2 = \frac{n \cdot s^2}{n-2}.$$

As $n \to \infty$ the distribution tends to the normal distribution.

A.2 The Crystal Ball function

The Crystal Ball function [134] is a model with a Gaussian core and a power-law tail to one side. The shape is controlled by four variables:

- μ: central value,
- σ: width,
- α: defines the transition from the power law to the Gaussian core,
- n: power-law value.

It has the functional form,

$$f(m;\alpha,n,\mu,\sigma) = \begin{cases} \exp\left(-\frac{(m-\mu)^2}{2\sigma^2}\right), & \text{for } \frac{m-\mu}{\sigma} > -\alpha \\ A\cdot(B-\frac{m-\mu}{\sigma})^{-n}, & \text{for } \frac{m-\mu}{\sigma} \leq -\alpha \\ , \end{cases} \tag{A.1}$$

where,

$$A = \left(\frac{n}{|\alpha|}\right) \quad , \quad B = \frac{n}{|\alpha|} - |\alpha|. \tag{A.2}$$

The double-sided Crystal Ball function, similarly to an ordinary Crystal Ball function, is an asymmetric Gaussian with power law tails. The double-sided Crystal Ball has power-law tails on either side. Its shape is controlled by six variables:

- μ: central value,
- σ: width,
- $\alpha_{L,R}$: defines the transition from the power law to the Gaussian core on the left and right sides,
- $n_{L,R}$: left and right side power-law values.

It has the functional form:

$$f(m;\alpha_{L,R},n_{L,R},\mu,\sigma) = \begin{cases} A_L\cdot(B_L-\frac{m-\mu}{\sigma})^{-n_L}, & \frac{m-\mu}{\sigma} < -\alpha_L \\ \exp(-\frac{1}{2}\cdot[\frac{m-\mu}{\sigma}]^2), & -\alpha_L < \frac{m-\mu}{\sigma} < \alpha_R \\ A_R\cdot(B_R+\frac{m-\mu}{\sigma})^{-n_R}, & \text{otherwise} \end{cases} \tag{A.3}$$

where,

$$A_i = (\frac{n_i}{|\alpha_i|})^{n_i}\cdot\exp(-\frac{|\alpha_i|^2}{2}), B_i = \frac{n_i}{|\alpha_i|} - |\alpha_i| \tag{A.4}$$

A.3 The Gaussian kernel PDF

The Gaussian Kernel PDF (`RooKeysPdf` in RooFit [152]) is a one-dimensional kernel estimation PDF, constructed as the superposition of Gaussian kernels that represent each data point. It is an unbinned and non-parametric method for estimating the parent distribution of a dataset [153].

Appendix B

Agreement between data and MC in the MVAs used to remove combinatorial background in the search for $B^0 \to \phi\phi$ decays

B.1 MVA for D_s^+-tagged background

Figures B.1 and B.2 show the agreement between data and MC in the variables used to train the MLP. These are split into TIS and TOS events respectively.

Figure B.3 shows the agrement of the MLP classifier output between data and MC for TIS and TOS events.

B.2 MVA for non-D_s^+-tagged background

Figures B.4 and B.5 show the agreement between data and MC for the input variables of the XGBoost (XBDT) classifier, for TIS and TOS events respectively. This classifier is used to remove non-D_s^+-tagged combinatorial background.

Figure B.6 shows the data and MC comparison of the classifier output following the full selection, excluding the cut on the XBDT itself.

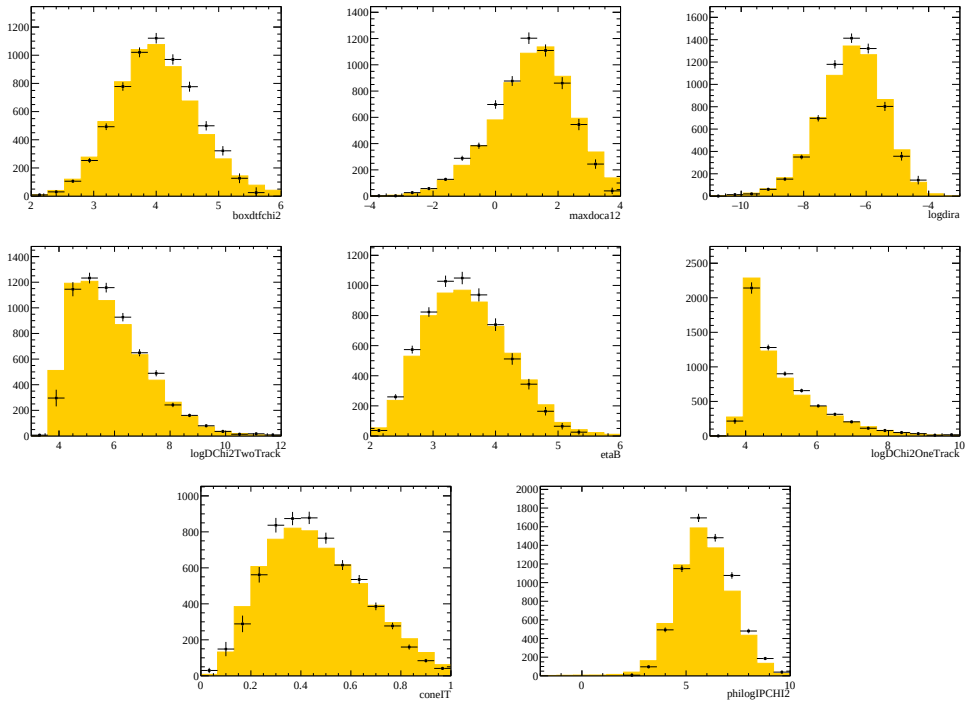

Figure B.1 *Comparisons between COWs-weighted data (black points) and truth-matched MC (solid yellow) for variables used in the MLP. Comparisons shown for TIS events*

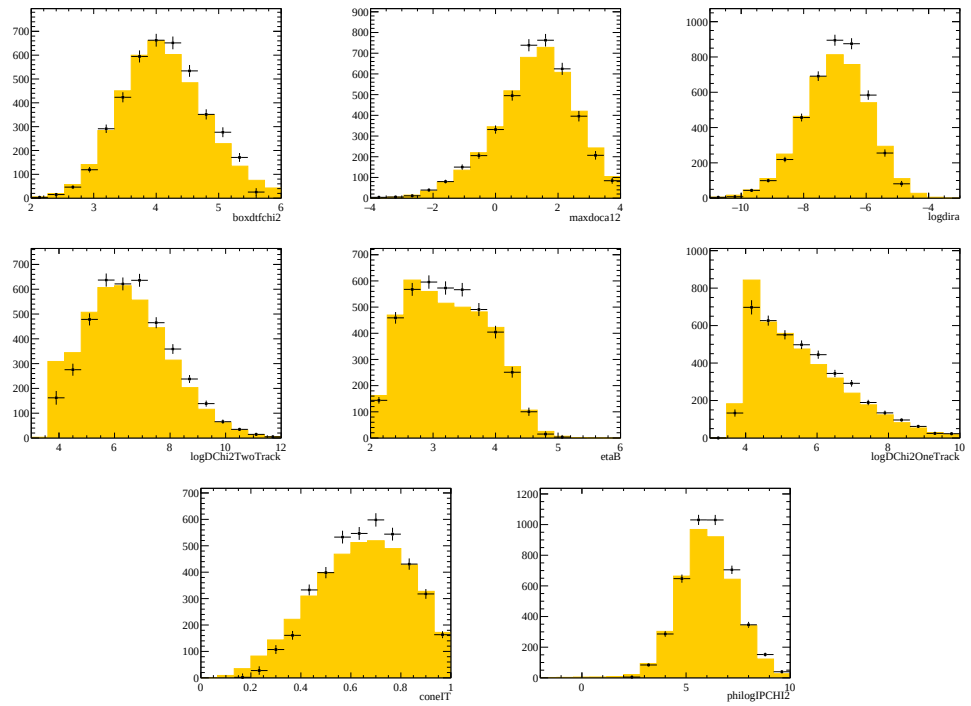

Figure B.2 *Comparisons between COWs-weighted data (black points) and truth-matched MC (solid yellow) for variables used in the MLP. Comparisons shown for TOS events*

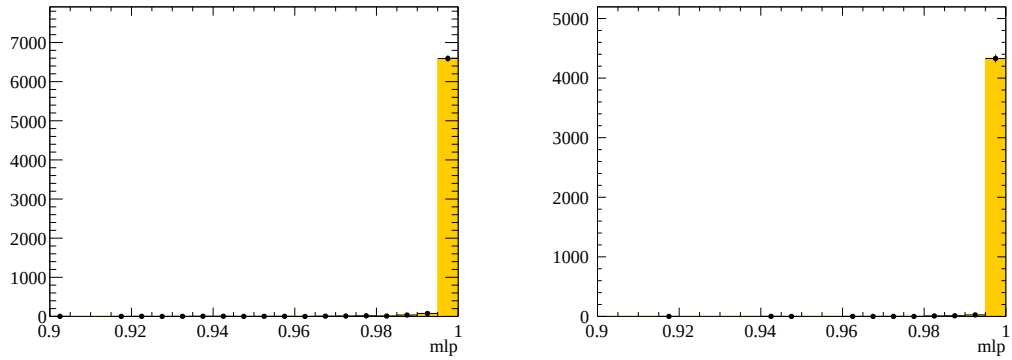

Figure B.3 *Comparisons between COWs-weighted data (black points) and truth-matched MC (solid yellow) for the output of the MLP MVA classifier. TIS events are shown on the left, and TOS events on the right. The chosen cut point is at 0.95.*

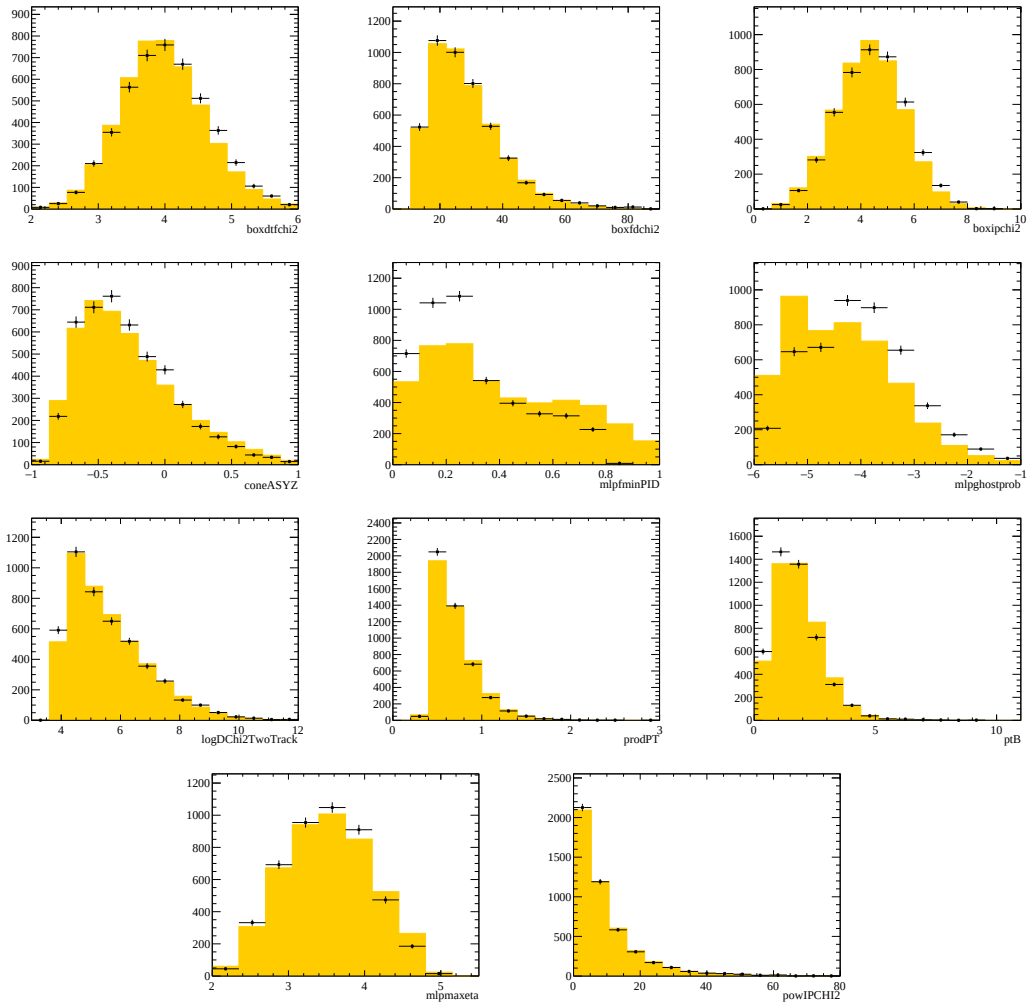

Figure B.4 *Input variables used in XBDT. Truth matched signal MC (yellow) and signal weighted data (black) for Run 2. Shown for TIS events*

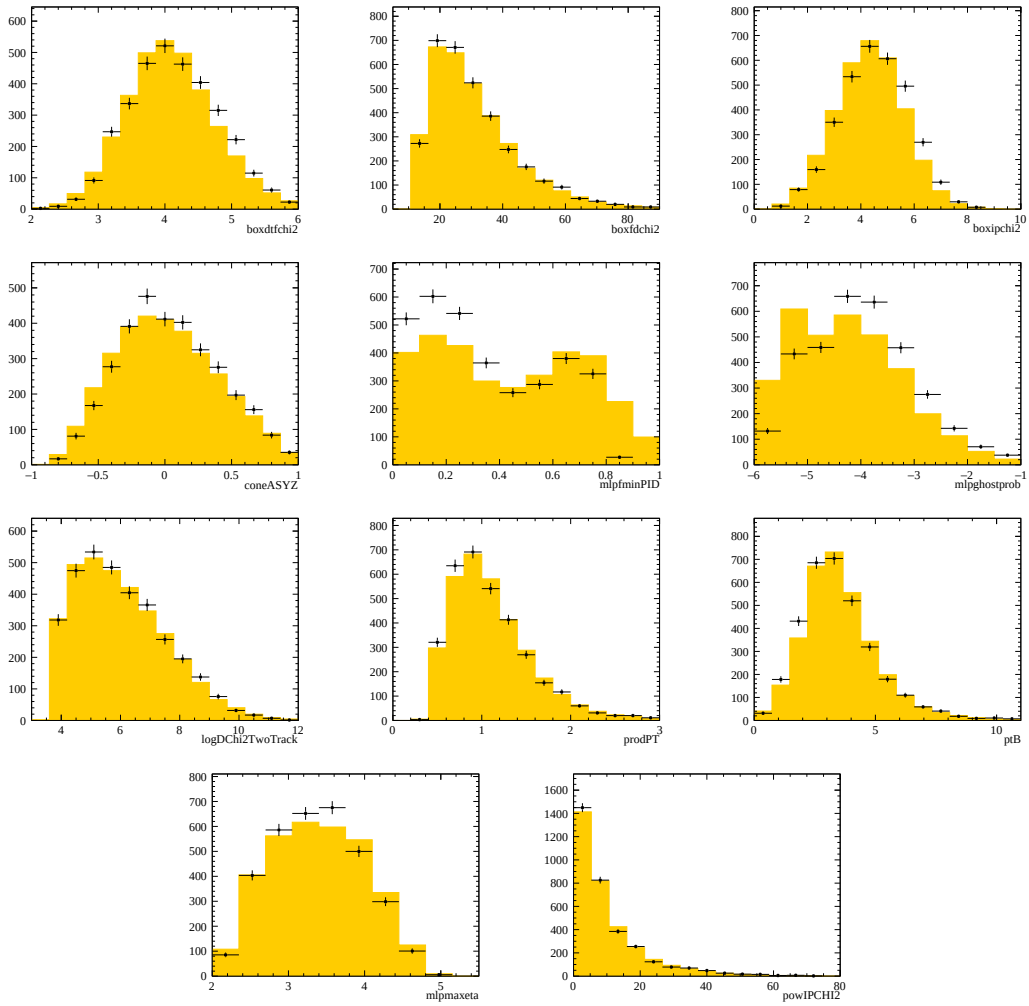

Figure B.5 *Input variables used in XBDT. Truth matched signal MC (yellow) and signal weighted data (black) for Run 2. Shown for TOS events*

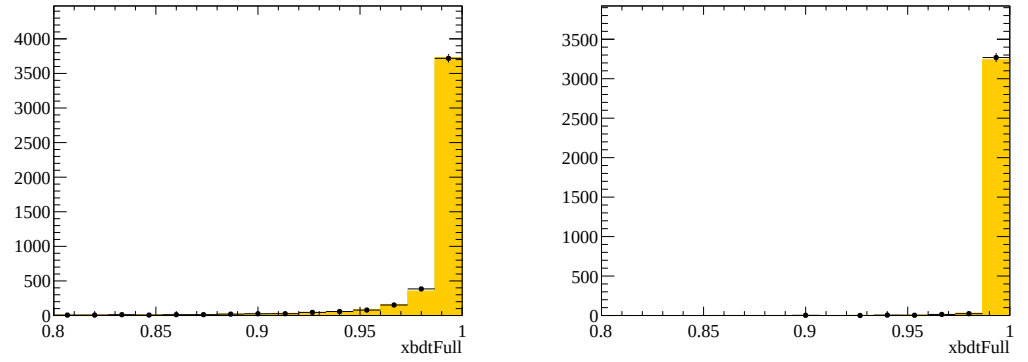

Figure B.6 *Comparisons between COWs-weighted data (black points) and truth-matched MC (solid yellow) for the output of the XBDT MVA classifier. TIS events are shown on the left, and TOS events on the right. Both data and MC have the full selection applied as described in Table 6.4, excluding the XBDT cut.*

Appendix C

Punzi multichannel optimisation scans

The Punzi figure of merit scans described in Chapter 6 were repeated for several cuts on the MLP classifier and on the PID. This means a global scan of the four selections: MLP, PID, TIS and TOS XBDT, can be done. Examples of the other scans are shown in Figure C.1.

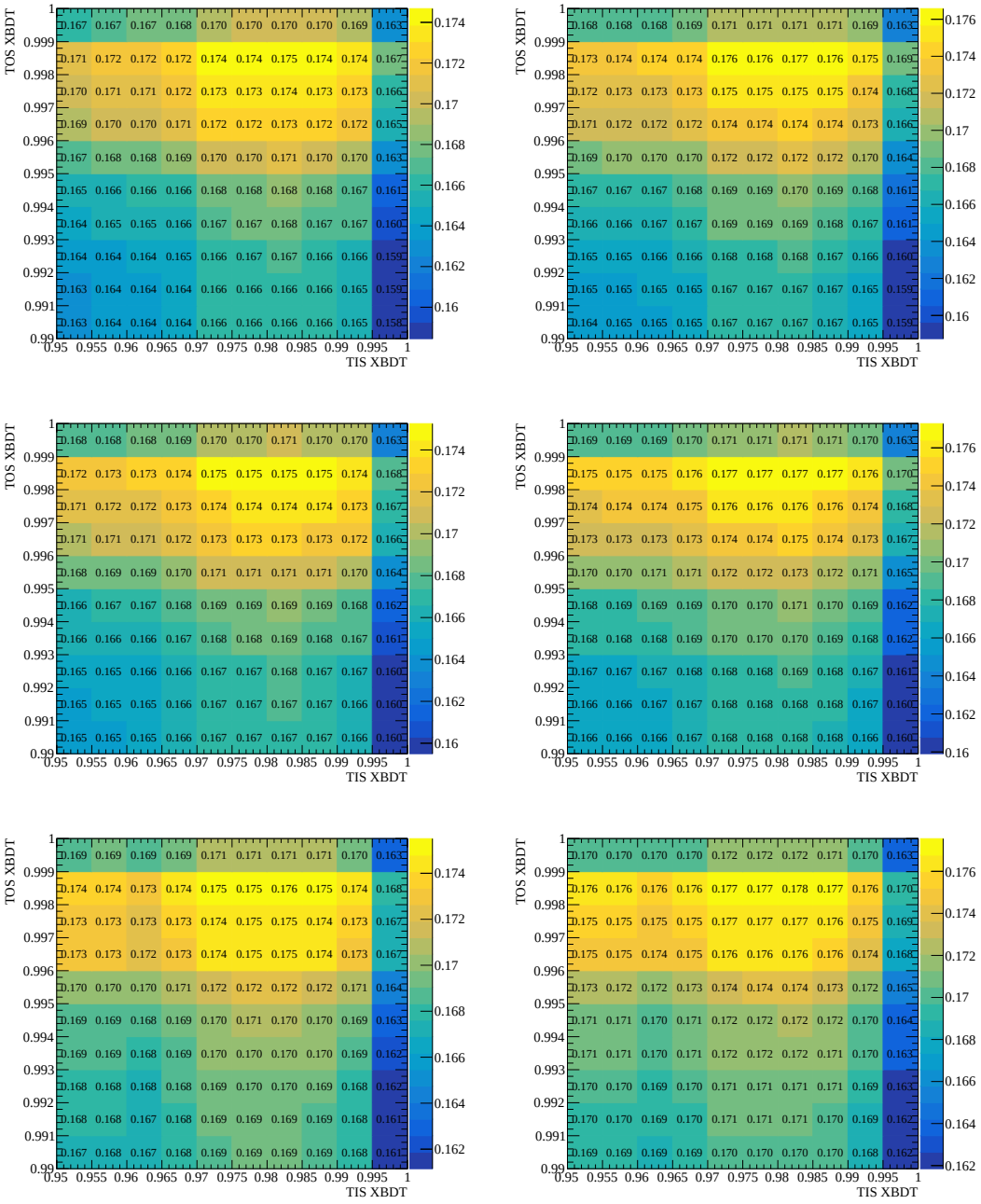

Figure C.1 *Examples of Run 2 Punzi scans at other MLP and PID working points. Scans on the left have a cut on the minimum value of (*`ProbNNK(1-ProbNNpi)`*) at 0.02, and on the right the cut is tightened to 0.05. From top to bottom, the MLP cut is tightened. The values of the cut are 0.5, 0.7 and 0.9 for the top, middle and bottom plots respectively.*

Appendix D

Input variables and performance of BDTG for D_s^+ candidates

The input training variables for the D_s^+ classifier are summarised in Table D.1, and shown for the Run 2 sample in Figure D.1. The output and ROC curve of the $D_s^+ \to \phi\pi^+$ classifiers are shown in Figure D.2, using the Run 2 dataset as an example. The working point of the classifiers is chosen to be 90% efficient which removes 94% of background.

Variable	$D_s^+ \to \phi\pi^+$	$D_s^+ \to \phi l^+\nu$
The vertex χ^2	✓	✓
The η of the pion	✓	✓
The minimum `ProbNNk` for the kaons	✓	
`ProbNNk` for the pion	✓	
`ProbNNpi` for the pion	✓	
`DOCA12` for the D_s^+ candidate	✓	✓
The flight-distance χ^2	✓	✓
The track ghost probability for the pion	✓	
The η of the D_s^+ candidate	✓	✓
The p_t of the D_s^+ candidate	✓	

Table D.1 *Input variable for the D_s^+ taggers.*

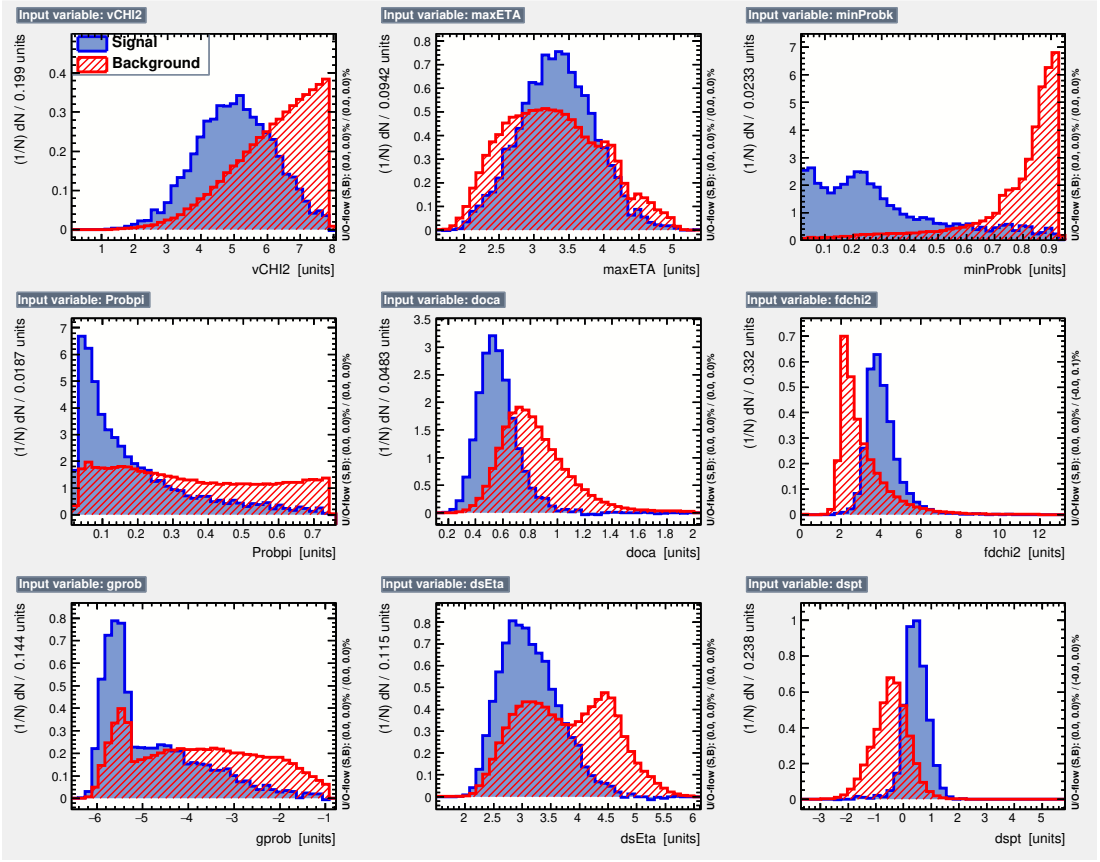

Figure D.1 *Input variable for the D_s^+ BDT classifiers, shown for the Run 2 sample.*

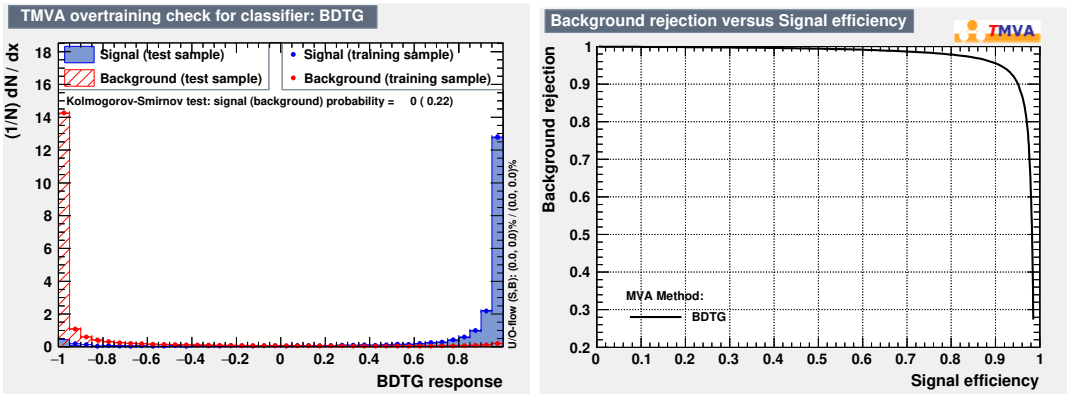

Figure D.2 *Distributions of the classifier trained to identify $D_s^+ \to \phi\pi^+$ and the ROC curve for the Run 2 dataset.*

Appendix E

Studies of $B^0_{(s)} \to \mu^+\mu^-$ in Upgrade II

In addition to the studies presented in Chapter 10, studies of the modes $B^0_s \to \mu^+\mu^-$ and $B^0 \to \mu^+\mu^-$ have also been performed. These decays provide a very clean probe of the SM [154]. The improvement in mass resolution can be seen in Figure E.1. The histograms of $B^0_s \to \mu^+\mu^-$ in Figure E.1 are normalised to unit area, and the histograms of $B^0 \to \mu^+\mu^-$ are normalised such that the relative yield of $B^0 \to \mu^+\mu^-$ to $B^0_s \to \mu^+\mu^-$ represents the ratio of the $B^0_{(s)} \to \mu^+\mu^-$ branching fractions. The widths of these distributions are calculated as the RMS and are summarised in Table E.1

	Mass resolution [MeV/c^2]	
Mode	Run 3	Upgrade II
$B^0_s \to \mu^+\mu^-$	20.46 ± 0.03	15.75 ± 0.02
$B^0 \to \mu^+\mu^-$	20.05 ± 0.03	15.55 ± 0.02

Table E.1 *Mass resolution for the $B^0_s \to \mu^+\mu^-$ and $B^0 \to \mu^+\mu^-$ decay channels in Run 3 and Upgrade II. Values are calculated as the RMS of the distributions.*

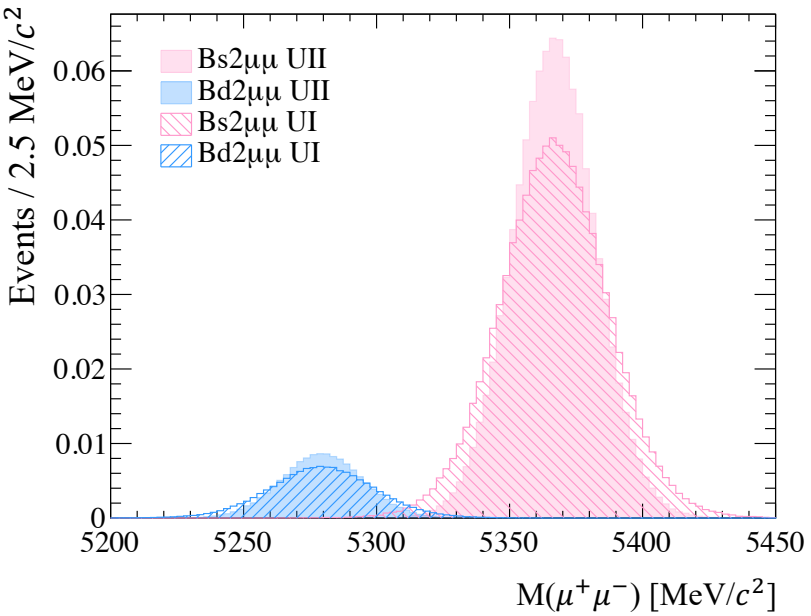

Figure E.1 *Improvement in mass resolution in* $B_s^0 \to \mu^+\mu^-$ *and* $B^0 \to \mu^+\mu^-$ *from Upgrade I to a modest Upgrade II. Upgrade I is shown in solid colour, and Upgrade II is hatched. The blue distributions represent* $B^0 \to \mu^+\mu^-$ *and the pink distributions represent* $B_s^0 \to \mu^+\mu^-$.

Bibliography

[1] R. Aaij et al. Measurement of CP violation in the $B_s^0 \to \phi\phi$ decay and search for the $B^0 \to \phi\phi$ decay. *Journal of High Energy Physics*, 2019 (12), Dec 2019. doi: 10.1007/jhep12(2019)155. URL https://doi.org/10.1007%2Fjhep12%282019%29155.

[2] Laurent Canetti, Marco Drewes, and Mikhail Shaposhnikov. Matter and antimatter in the universe. *New Journal of Physics*, 14(9): 095012, Sep 2012. URL https://iopscience.iop.org/article/10.1088/1367-2630/14/9/095012.

[3] M. Sozzi. *Discrete Symmetries and CP Violation: From Experiment to Theory*. Oxford Graduate Texts. OUP Oxford, 2008. ISBN 9780199296668. URL https://books.google.co.uk/books?id=ctoSDAAAQBAJ.

[4] A. D. Sakharov. Violation of CP Invariance, C asymmetry, and baryon asymmetry of the universe. *Pisma Zh. Eksp. Teor. Fiz.*, 5:32–35, 1967. doi: 10.1070/PU1991v034n05ABEH002497.

[5] E. S. Abers and B. W. Lee. Gauge Theories. *Phys. Rept.*, 9:1–141, 1973. doi: 10.1016/0370-1573(73)90027-6.

[6] A. Augusto Alves, Jr. et al. The LHCb Detector at the LHC. *JINST*, 3: S08005, 2008. doi: 10.1088/1748-0221/3/08/S08005. URL https://dx.doi.org/10.1088/1748-0221/3/08/S08005.

[7] Wikimedia Commons. Standard model of elementary particles. URL https://en.wikipedia.org/wiki/File:Standard_Model_of_Elementary_Particles.svg.

[8] M. Banner et al. Observation of Single Isolated Electrons of High Transverse Momentum in Events with Missing Transverse Energy at the CERN anti-p p Collider. *Phys. Lett. B*, 122:476–485, 1983. doi: 10.1016/0370-2693(83)91605-2.

[9] G. Arnison et al. Experimental Observation of Lepton Pairs of Invariant Mass Around 95 GeV/c^2 at the CERN SPS Collider. *Phys. Lett. B*, 126: 398–410, 1983. doi: 10.1016/0370-2693(83)90188-0.

[10] S. L. Glashow. Partial Symmetries of Weak Interactions. *Nucl. Phys.*, 22: 579–588, 1961. doi: 10.1016/0029-5582(61)90469-2.

[11] P. W. Higgs. Broken Symmetries and the Masses of Gauge Bosons. *Phys. Rev. Lett.*, 13:508–509, 1964. doi: 10.1103/PhysRevLett.13.508.

[12] S Weinberg. A Model of Leptons. *Phys. Rev. Lett.*, 19:1264–1266, 1967. doi: 10.1103/PhysRevLett.19.1264.

[13] A Salam. Weak and Electromagnetic Interactions. *Conf. Proc. C*, 680519: 367–377, 1968. doi: 10.1142/9789812795915_0034.

[14] C-N. Yang and R. L. Mills. Conservation of Isotopic Spin and Isotopic Gauge Invariance. *Phys. Rev.*, 96:191–195, 1954. doi: 10.1103/PhysRev.96.191.

[15] D. J. Gross and F. Wilczek. Ultraviolet Behavior of Nonabelian Gauge Theories. *Phys. Rev. Lett.*, 30:1343–1346, 1973. doi: 10.1103/PhysRevLett.30.1343.

[16] H. D. Politzer. Reliable Perturbative Results for Strong Interactions? *Phys. Rev. Lett.*, 30:1346–1349, 1973. doi: 10.1103/PhysRevLett.30.1346.

[17] M. Gell-Mann. A Schematic Model of Baryons and Mesons. *Phys. Lett.*, 8: 214–215, 1964. doi: 10.1016/S0031-9163(64)92001-3.

[18] E. D. Bloom et al. High-Energy Inelastic e p Scattering at 6-Degrees and 10-Degrees. *Phys. Rev. Lett.*, 23:930–934, 1969. doi: 10.1103/PhysRevLett.23.930.

[19] S. L. Glashow, J. Iliopoulos, and L. Maiani. Weak Interactions with Lepton-Hadron Symmetry. *Phys. Rev. D*, 2:1285–1292, 1970. doi: 10.1103/PhysRevD.2.1285.

[20] M. Kobayashi and T. Maskawa. CP Violation in the Renormalizable Theory of Weak Interaction. *Prog. Theor. Phys.*, 49:652–657, 1973. doi: 10.1143/PTP.49.652.

[21] J. E. Augustin et al. Discovery of a Narrow Resonance in e^+e^- Annihilation. *Phys. Rev. Lett.*, 33:1406–1408, 1974. doi: 10.1103/PhysRevLett.33.1406.

[22] J. J. Aubert et al. Experimental Observation of a Heavy Particle J. *Phys. Rev. Lett.*, 33:1404–1406, 1974. doi: 10.1103/PhysRevLett.33.1404.

[23] S. W. Herb et al. Observation of a Dimuon Resonance at 9.5-GeV in 400-GeV Proton-Nucleus Collisions. *Phys. Rev. Lett.*, 39:252–255, 1977. doi: 10.1103/PhysRevLett.39.252.

[24] A. Caner. Observation of top quark production in $\bar{p}p$ collisions with the Collider Detector at Fermilab. In *23rd International Meeting on Fundamental Physics: The Top Quark, Heavy Flavor Physics and Symmetry Breaking*, pages 188–197, 5 1995.

[25] N. J. Hadley. Observation of the top quark with the D0 detector. In *23rd Annual SLAC Summer Institute on Particle Physics: The Top Quark and the Electroweak Interaction (SSI 95)*, pages 309–326, 11 1995. doi: 10.2172/155663.

[26] G. Aad et al. Observation of a new particle in the search for the Standard Model Higgs boson with the ATLAS detector at the LHC. *Physics Letters B*, 716(1):1–29, September 2012. ISSN 0370-2693. doi: 10.1016/j.physletb.2012.08.020. URL http://dx.doi.org/10.1016/j.physletb.2012.08.020.

[27] S. Chatrchyan et al. Observation of a new boson at a mass of 125 GeV with the CMS experiment at the LHC. *Physics Letters B*, 716(1):30–61, September 2012. ISSN 0370-2693. doi: 10.1016/j.physletb.2012.08.021. URL http://dx.doi.org/10.1016/j.physletb.2012.08.021.

[28] E. Majorana. *A Symmetric Theory of Electrons and Positrons*, pages 113–128. Springer International Publishing, 2020. ISBN 978-3-030-23509-3. doi: 10.1007/978-3-030-23509-3_11. URL https://doi.org/10.1007/978-3-030-23509-3_11.

[29] M. Aker et al. Direct neutrino-mass measurement based on 259 days of katrin data, 2024. URL https://arxiv.org/abs/2406.13516.

[30] S. F. King. Discrete Symmetries and Models of Flavour Mixing. *J. Phys. Conf. Ser.*, 631(1):012005, 2015. doi: 10.1088/1742-6596/631/1/012005.

[31] Jure Zupan. Introduction to flavour physics. *CERN Yellow Rep. School Proc.*, 6:181–212, 2019. doi: 10.23730/CYRSP-2019-006.181. URL https://cds.cern.ch/record/2702255. 32 pages, 22 figures, the write-up is a combination of lectures given at ESHEP 2018, SSI 2018 and the US Belle II summer schools, Fig. 1 corrected, several typographical errors fixed.

[32] N. Cabibbo. Unitary Symmetry and Leptonic Decays. *Phys. Rev. Lett.*, 10:531–533, 1963. doi: 10.1103/PhysRevLett.10.531.

[33] Andreas Hocker and Zoltan Ligeti. CP violation and the CKM matrix. *Ann. Rev. Nucl. Part. Sci.*, 56:501–567, 2006. doi: 10.1146/annurev.nucl.56.080805.140456.

[34] G.C. et al. Branco. *CP Violation*. International series of monographs on physics. Clarendon Press, 1999. ISBN 9780198503996. URL https://books.google.co.uk/books?id=N-uHNjmnRoIC.

[35] Hilary Greaves and Teruji Thomas. On the CPT theorem. *Stud. Hist. Phil. Sci. B*, 45:46–65, 2014. doi: 10.1016/j.shpsb.2013.10.001.

[36] J. et al. Charles. New physics in B meson mixing: future sensitivity and limitations. *Phys. Rev. D*, 102(5):056023, 2020. doi: 10.1103/PhysRevD.102.056023.

[37] P. Vanhoefer et al. Study of $B^0 \to \rho^+\rho^-$ decays and implications for the CKM angle ϕ_2. *Phys. Rev. D*, 93(3):032010, 2016. doi: 10.1103/PhysRevD.93.032010. [Addendum: Phys.Rev.D 94, 099903 (2016)].

[38] R. Aaij et al. Measurement of polarization amplitudes and CP asymmetries in $B^0 \to \phi K^*(892)^0$. *JHEP*, 05:069, 2014. doi: 10.1007/JHEP05(2014)069.

[39] A. Gritsan. Polarization puzzle in $B \to \phi K^*$ and other $B \to$ VV at BABAR. In *32nd International Conference on High Energy Physics*, pages 1117–1120, 9 2004. doi: 10.1142/9789812702227_0225.

[40] T. Aaltonen et al. Measurement of Polarization and Search for CP-Violation in $B_s^0 \to \phi\phi$ Decays. *Phys. Rev. Lett.*, 107:261802, 2011. doi: 10.1103/PhysRevLett.107.261802.

[41] R. Aaij et al. Measurement of the polarization amplitudes and triple product asymmetries in the $B_s^0 \to \phi\phi$ decay. *Phys. Lett. B*, 713:369–377, 2012. doi: 10.1016/j.physletb.2012.06.012.

[42] R. Aaij et al. Precision Measurement of CP Violation in the Penguin-Mediated Decay $B_s^0 \to \phi\phi$. *Phys. Rev. Lett.*, 131(17):171802, 2023. doi: 10.1103/PhysRevLett.131.171802.

[43] A. L. Kagan. Polarization in $B \to VV$ decays. *Phys. Lett. B*, 601:151–163, 2004. doi: 10.1016/j.physletb.2004.09.030.

[44] H-Y. Cheng, C-K. Chua, and A. Soni. Final state interactions in hadronic B decays. *Phys. Rev. D*, 71:014030, 2005. doi: 10.1103/PhysRevD.71.014030.

[45] M. Beneke, J. Rohrer, and D. Yang. Branching fractions, polarisation and asymmetries of $B \to VV$ decays. *Nucl. Phys. B*, 774:64–101, 2007. doi: 10.1016/j.nuclphysb.2007.03.020.

[46] R. Aaij et al. First measurement of the CP-violating phase in $B_s^0 \to \phi\phi$ decays. *Phys. Rev. Lett.*, 110(24):241802, 2013. doi: 10.1103/PhysRevLett.110.241802.

[47] R. Aaij et al. Measurement of CP violation in $B_s^0 \to \phi\phi$ decays. *Phys. Rev. D*, 90(5):052011, 2014. doi: 10.1103/PhysRevD.90.052011.

[48] A. Datta and D. London. Triple-Product correlations in $B \to V_1V_2$ decays and new physics. *International Journal of Modern Physics A*, 19(15): 2505–2544, June 2004. ISSN 1793-656X. doi: 10.1142/s0217751x04018300. URL `http://dx.doi.org/10.1142/S0217751X04018300`.

[49] M. Gronau and J. L. Rosner. Triple product asymmetries in K, $D_{(s)}$ and $B_{(s)}$ decays. *Phys. Rev. D*, 84:096013, 2011. doi: 10.1103/PhysRevD.84.096013.

[50] S. Okubo. Phi meson and unitary symmetry model. *Phys. Lett.*, 5:165–168, 1963. doi: 10.1016/S0375-9601(63)92548-9.

[51] J. Iizuka. A Systematics and Phenomenology of Meson Family. *Progress of Theoretical Physics Supplement*, 37-38:21–34, 03 1966. ISSN 0375-9687. doi: 10.1143/PTPS.37.21. URL `https://doi.org/10.1143/PTPS.37.21`.

[52] Zhi-Tian Zou, Ahmed Ali, Cai-Dian Lu, Xin Liu, and Ying Li. Improved Estimates of The $B_{(s)} \to VV$ Decays in Perturbative QCD Approach. *Phys. Rev. D*, 91:054033, 2015. doi: 10.1103/PhysRevD.91.054033.

[53] J. Chai, S. Cheng, Y-H. Ju, D-C. Yan, C-D. Lü, and Z-J. Xiao. Charmless two-body B meson decays in the perturbative QCD factorization approach. *Chin. Phys. C*, 46(12):123103, 2022. doi: 10.1088/1674-1137/ac88bd.

[54] D-C. Yan, Z. Rui, Z-J Xiao, and Y Li. Study of $B_s^0 \to \phi\phi \to (K^+K^-)(K^+K^-)$ decays in the perturbative QCD approach. *Phys. Rev. D*, 105(9):093001, 2022. doi: 10.1103/PhysRevD.105.093001.

[55] R. Aleksan and L. Oliver. Remarks on the penguin decay $B_s \to \phi\phi$ with prospects for FCC-*ee*. 5 2022.

[56] Ying Li. Investigating the Effect of Family Non-universal Z' Boson in $B \to phi\phi$ Decay. *Phys. Rev. D*, 89(1):014003, 2014. doi: 10.1103/PhysRevD.89.014003.

[57] C-D. Lu, Y-L. Shen, and J. Zhu. $B^0 \to \phi\phi$ decay in perturbative QCD approach. *Eur.Phys.J.*, C41:311–317, 2005. doi: 10.1140/epjc/s2005-02199-7.

[58] S. Bar-Shalom, G. Eilam, and Y-D. Yang. $B \to \phi\pi$ and $B^0 \to \phi\phi$ in the standard model and new bounds on R parity violation. *Phys.Rev.*, D67:014007, 2003. doi: 10.1103/PhysRevD.67.014007.

[59] M. Gronau, D. London, and J. L. Rosner. Rescattering Contributions to rare B-Meson Decays. *Phys. Rev. D*, 87(3):036008, 2013. doi: 10.1103/PhysRevD.87.036008.

[60] M. Gronau and J. L. Rosner. B decays dominated by $\omega - \phi$ mixing. *Phys. Lett. B*, 666:185–188, 2008. doi: 10.1016/j.physletb.2008.07.016.

[61] P.A. Zyla et al. Review of Particle Physics. *PTEP*, 2020(8):083C01, 2020. doi: 10.1093/ptep/ptaa104. and 2021 update.

[62] S. P. Martin. A Supersymmetry primer. *Adv. Ser. Direct. High Energy Phys.*, 18:1–98, 1998. doi: 10.1142/9789812839657_0001.

[63] J. H. Kim et al. Search for $B \to \phi\pi$ decays. *Phys. Rev. D*, 86:031101, 2012. doi: 10.1103/PhysRevD.86.031101.

[64] Chuan-Hung Chen and Hisaki Hatanaka. Nonuniversal Z-prime couplings in B decays. *Phys. Rev. D*, 73:075003, 2006. doi: 10.1103/PhysRevD.73.075003.

[65] D. M. Asner et al. Search for exclusive charmless hadronic B decays. *Phys. Rev. D*, 53:1039–1050, 1996. doi: 10.1103/PhysRevD.53.1039.

[66] T. Bergfeld et al. Observation of $B^+ \to \omega K+$ and search for related B decay modes. *Phys. Rev. Lett.*, 81:272–276, 1998. doi: 10.1103/PhysRevLett.81.272.

[67] B. Aubert et al. Searches for B meson decays to $\phi\phi$, $\phi\rho$, $\phi f_0(980)$, and $f_0(980)f_0(980)$ final states. *Phys. Rev. Lett.*, 101:201801, 2008. doi: 10.1103/PhysRevLett.101.201801.

[68] R. Aaij et al. Observation of CP Violation in Charm Decays. *Physical Review Letters*, 122(21), May 2019. ISSN 1079-7114. doi: 10.1103/physrevlett.122.211803. URL `http://dx.doi.org/10.1103/PhysRevLett.122.211803`.

[69] R. Aaij et al. Precise determination of the B_s^0–$\overline{B}_s^0$ oscillation frequency. *Nature Physics*, 18(1):1–5, January 2022. ISSN 1745-2481. doi: 10.1038/s41567-021-01394-x. URL `http://dx.doi.org/10.1038/s41567-021-01394-x`.

[70] D. Johnson, I. Polyakov, T. Skwarnicki, and M. Wang. Exotic Hadrons at LHCb. March 2024. doi: 10.1146/annurev-nucl-102422-040628.

[71] P. Koppenburg. List of hadrons observed at the LHC. LHCb-FIGURE-2021-001, Mar 2021. URL `https://cds.cern.ch/record/2693187`. See 2022 update online.

[72] I. Bediaga et al. Framework TDR for the LHCb Upgrade: Technical Design Report. 4 2012.

[73] R. Aaij et al. The LHCb upgrade I, 2023.

[74] O. S. Brüning, P. Collier, P. Lebrun, S. Myers, R. Ostojic, J. Poole, and P. Proudlock. *LHC Design Report*. CERN Yellow Reports: Monographs. CERN, Geneva, 2004. doi: 10.5170/CERN-2004-003-V-1. URL `https://cds.cern.ch/record/782076`.

[75] G. Aad et al. The ATLAS Experiment at the CERN Large Hadron Collider. *JINST*, 3:S08003, 2008. doi: 10.1088/1748-0221/3/08/S08003.

[76] S. Chatrchyan et al. The CMS Experiment at the CERN LHC. *JINST*, 3: S08004, 2008. doi: 10.1088/1748-0221/3/08/S08004.

[77] K. Aamodt et al. The ALICE experiment at the CERN LHC. *JINST*, 3: S08002, 2008. doi: 10.1088/1748-0221/3/08/S08002.

[78] John C. Collins and M. J. Perry. Superdense Matter: Neutrons Or Asymptotically Free Quarks? *Phys. Rev. Lett.*, 34:1353, 1975. doi: 10.1103/PhysRevLett.34.1353.

[79] R. Aaij et al. Helium identification with LHCb. *Journal of Instrumentation*, 19(02):P02010, February 2024. ISSN 1748-0221. doi: 10.1088/1748-0221/19/02/p02010. URL http://dx.doi.org/10.1088/1748-0221/19/02/P02010.

[80] Christian Bierlich, Smita Chakraborty, Nishita Desai, Leif Gellersen, Ilkka Helenius, Philip Ilten, Leif Lönnblad, Stephen Mrenna, Stefan Prestel, Christian T. Preuss, Torbjörn Sjöstrand, Peter Skands, Marius Utheim, and Rob Verheyen. A comprehensive guide to the physics and usage of pythia 8.3, 2022. URL https://arxiv.org/abs/2203.11601.

[81] C. Elsasser. $\bar{b}b$ production angle plots. URL https://lhcb.web.cern.ch/lhcb/speakersbureau/html/bb_ProductionAngles.html.

[82] Benjamin Michael Wynne. Measurement of the underlying event in pp collisions using the ATLAS detector and development of a software suite for Bayesian unfolding, 2013. URL https://cds.cern.ch/record/1626590. Presented 04 Dec 2012.

[83] S Amato et al. *LHCb magnet: Technical Design Report*. Technical design report. LHCb. CERN, Geneva, 2000. URL https://cds.cern.ch/record/424338.

[84] P R Barbosa-Marinho et al. *LHCb inner tracker: Technical Design Report*. Technical design report. LHCb. CERN, Geneva, 2002. URL https://cds.cern.ch/record/582793. revised version number 1 submitted on 2002-11-13 14:14:34.

[85] P R Barbosa-Marinho et al. *LHCb outer tracker: Technical Design Report*. Technical design report. LHCb. CERN, Geneva, 2001. URL https://cds.cern.ch/record/519146.

[86] M. Adinolfi et al. Performance of the LHCb RICH detector at the LHC. *The European Physical Journal C*, 73(5), May 2013. ISSN 1434-6052. doi: 10.1140/epjc/s10052-013-2431-9. URL http://dx.doi.org/10.1140/epjc/s10052-013-2431-9.

[87] J V Jelley. Cerenkov radiation and its applications. *British Journal of Applied Physics*, 6(7):227, jul 1955. doi: 10.1088/0508-3443/6/7/301. URL https://dx.doi.org/10.1088/0508-3443/6/7/301.

[88] P R Barbosa-Marinho et al. *LHCb VELO (VErtex LOcator): Technical Design Report*. Technical design report. LHCb. CERN, Geneva, 2001. URL https://cds.cern.ch/record/504321.

[89] R Aaij et al. Performance of the LHCb Vertex Locator. *Journal of Instrumentation*, 9(09):P09007–P09007, September 2014. ISSN 1748-0221. doi: 10.1088/1748-0221/9/09/p09007. URL http://dx.doi.org/10.1088/1748-0221/9/09/P09007.

[90] R Antunes-Nobrega et al. *LHCb trigger system: Technical Design Report*. Technical design report. LHCb. CERN, Geneva, 2003. URL https://cds.cern.ch/record/630828. revised version number 1 submitted on 2003-09-24 12:12:22.

[91] G. A. Cowan. Performance of the LHCb silicon tracker. *Nuclear Instruments and Methods in Physics Research Section A: Accelerators, Spectrometers, Detectors and Associated Equipment*, 699:156–159, 2013. ISSN 0168-9002. doi: https://doi.org/10.1016/j.nima.2012.05.074. URL https://www.sciencedirect.com/science/article/pii/S0168900212005876. Proceedings of the 8th International "Hiroshima" Symposium on the Development and Application of Semiconductor Tracking Detectors.

[92] M. Tobin. Performance of the LHCb Tracking Detectors. 2013. URL https://cds.cern.ch/record/1532586.

[93] R. Arink et al. Performance of the LHCb Outer Tracker. *JINST*, 9:P01002, 2014. doi: 10.1088/1748-0221/9/01/P01002. URL https://cds.cern.ch/record/1629476. Comments: 30 pages, 20 figures.

[94] S Amato et al. *LHCb RICH: Technical Design Report*. Technical design report. LHCb. CERN, Geneva, 2000. URL https://cds.cern.ch/record/494263.

[95] R. Calabrese et al. Performance of the LHCb RICH detectors during LHC Run 2. *Journal of Instrumentation*, 17(07):P07013, July 2022. ISSN 1748-0221. doi: 10.1088/1748-0221/17/07/p07013. URL http://dx.doi.org/10.1088/1748-0221/17/07/P07013.

[96] S Amato et al. *LHCb calorimeters: Technical Design Report*. Technical design report. LHCb. CERN, Geneva, 2000. URL https://cds.cern.ch/record/494264.

[97] C. Abellán Beteta et al. Calibration and performance of the LHCb calorimeters in Run 1 and 2 at the LHC, 2020.

[98] P R Barbosa-Marinho et al. *LHCb muon system: Technical Design Report*. Technical design report. LHCb. CERN, Geneva, 2001. URL https://cds.cern.ch/record/504326.

[99] Jr. Alves, A.A. et al. Performance of the LHCb muon system. *JINST*, 8: P02022, 2013. doi: 10.1088/1748-0221/8/02/P02022. URL https://cds.cern.ch/record/1492807. JINST_015P_1112 2013.

[100] Roel Aaij et al. Design and performance of the LHCb trigger and full real-time reconstruction in Run 2 of the LHC. *JINST*, 14(04):P04013, 2019. doi: 10.1088/1748-0221/14/04/P04013.

[101] X Cid Vidal and J A Hernando. Inspecting LHCb Hadron Trigger. Technical report, CERN, Geneva, 2011. URL http://cds.cern.ch/record/1331495.

[102] Vladimir V Gligorov. A single track HLT1 trigger. Technical report, CERN, Geneva, 2010. URL https://cds.cern.ch/record/1323812.

[103] R. E. Kalman. A New Approach to Linear Filtering and Prediction Problems. *J. Fluids Eng.*, 82(1):35–45, 1960. doi: 10.1115/1.3662552.

[104] R Aaij et al. The LHCb Trigger and its Performance in 2011. *JINST*, 8: P04022, 2013. doi: 10.1088/1748-0221/8/04/P04022.

[105] LHCb Collaboration. LHCb VELO Upgrade Technical Design Report. Technical report, CERN, 2013. URL http://cds.cern.ch/record/1624070.

[106] K. Hennessy. LHCb VELO upgrade. *Nuclear Instruments and Methods in Physics Research Section A: Accelerators, Spectrometers, Detectors and Associated Equipment*, 845:97–100, 2017. ISSN 0168-9002. doi: https://doi.org/10.1016/j.nima.2016.04.077. URL https://www.sciencedirect.com/science/article/pii/S016890021630290X. Proceedings of the Vienna Conference on Instrumentation 2016.

[107] LHCb Collaboration. LHCb Tracker Upgrade Technical Design Report. Technical report, 2014. URL https://cds.cern.ch/record/1647400.

[108] P. Hopchev. SciFi: A large Scintillating Fibre Tracker for LHCb, 2017.

[109] LHCb Collaboration. LHCb PID Upgrade Technical Design Report. Technical report, 2013. URL https://cds.cern.ch/record/1624074.

[110] LHCb Trigger and Online Upgrade Technical Design Report. Technical report, 2014. URL https://cds.cern.ch/record/1701361.

[111] RTA and DPA dataflow diagrams for Run 1, Run 2, and the upgraded LHCb detector . 2020. URL https://cds.cern.ch/record/2730181.

[112] Marian Stahl. Machine learning and parallelism in the reconstruction of lhcb and its upgrade. *Journal of Physics: Conference Series*, 898, 10 2017. doi: 10.1088/1742-6596/898/4/042042.

[113] O Callot and S Hansmann-Menzemer. The Forward Tracking: Algorithm and Performance Studies. Technical report, CERN, Geneva, 2007. URL https://cds.cern.ch/record/1033584.

[114] R W Forty and M Needham. Standalone Track Reconstruction in the T-stations. Technical report, CERN, Geneva, 2007. URL https://cds.cern.ch/record/1024496.

[115] M. Needham. Identification of Ghost Tracks using a Likelihood Method, 5 2008.

[116] G. A. Cowan, D. C. Craik, and M. D. Needham. RapidSim: an application for the fast simulation of heavy-quark hadron decays. *Comput. Phys. Commun.*, 214:239–246, 2017. doi: 10.1016/j.cpc.2017.01.029.

[117] Christian Bierlich et al. A comprehensive guide to the physics and usage of PYTHIA 8.3. *SciPost Phys. Codeb.*, 2022:8, 2022. doi: 10.21468/SciPostPhysCodeb.8.

[118] D. J. Lange. The EvtGen particle decay simulation package. *Nucl. Instrum. Meth. A*, 462:152–155, 2001. doi: 10.1016/S0168-9002(01)00089-4.

[119] S. Agostinelli et al. GEANT4 - A Simulation Toolkit. *Nucl. Instrum. Meth. A*, 506:250–303, 2003. doi: 10.1016/S0168-9002(03)01368-8.

[120] Roel Aaij et al. Momentum scale calibration of the LHCb spectrometer. *JINST*, 19(02):P02008, 2024. doi: 10.1088/1748-0221/19/02/P02008.

[121] Matteo Cacciari, Mario Greco, and Paolo Nason. The p_T spectrum in heavy-flavour hadroproduction. *JHEP*, 05:007, 1998. doi: 10.1088/1126-6708/1998/05/007.

[122] M Needham. Performance of the LHCb Track Reconstruction Software. Technical report, CERN, Geneva, 2008. URL `https://cds.cern.ch/record/1080556`.

[123] R Aaij et al. Precision measurement of D meson mass differences. *JHEP*, 06:065, 2013. doi: 10.1007/JHEP06(2013)065.

[124] J. Wishahi. Flavour tagging plots for conference. URL `https://twiki.cern.ch/twiki/bin/view/LHCb/FlavourTaggingConferencePlots`.

[125] Thomas Junk. Confidence level computation for combining searches with small statistics. *Nucl. Instrum. Meth. A*, 434:435–443, 1999. doi: 10.1016/S0168-9002(99)00498-2.

[126] Alexander L. Read. Presentation of search results: The CL_s technique. *J. Phys. G*, 28:2693–2704, 2002. doi: 10.1088/0954-3899/28/10/313.

[127] S. Navas et al. Review of particle physics. *Phys. Rev. D*, 110(3):030001, 2024. doi: 10.1103/PhysRevD.110.030001.

[128] P. Astier et al. Kalman filter track fits and track breakpoint analysis. *Nuclear Instruments and Methods in Physics Research Section A: Accelerators, Spectrometers, Detectors and Associated Equipment*, 450 (1):138–154, August 2000. ISSN 0168-9002. doi: 10.1016/s0168-9002(00)00154-6. URL `http://dx.doi.org/10.1016/S0168-9002(00)00154-6`.

[129] D. Bodrov et al. Study of the muon decay-in-flight in the τ-$\to\mu$-$\bar{\nu}\mu\nu\tau$ decay to measure the Michel parameter ξ'. *Phys. Rev. D*, 108(1):012003, 2023. doi: 10.1103/PhysRevD.108.012003.

[130] Vladimir Chekhovsky et al. Identification of low-momentum muons in the CMS detector using multivariate techniques in proton-proton collisions at $\sqrt{s} = 13.6$ TeV. 12 2024.

[131] A. Hocker et al. TMVA - Toolkit for Multivariate Data Analysis, 3 2007.

[132] J Van Tilburg. Track simulation and reconstruction in LHCb, May 2005.

[133] H. Dembinski, M. Kenzie, C. Langenbruch, and M. Schmelling. Custom Orthogonal Weight functions (COWs) for event classification. *Nuclear Instruments and Methods in Physics Research Section A: Accelerators, Spectrometers, Detectors and Associated Equipment*, 1040:167270, October 2022. ISSN 0168-9002. doi: 10.1016/j.nima.2022.167270. URL `http://dx.doi.org/10.1016/j.nima.2022.167270`.

[134] Tomasz Skwarnicki. *A study of the radiative CASCADE transitions between the Upsilon-Prime and Upsilon resonances*. PhD thesis, Cracow, INP, 1986.

[135] I. M. Chakaravarti, R.G. Laha, and J. Roy. *Handbook of Methods of Applied Statistics*, volume 1. John Wiley and Sons, 1967.

[136] J. Albrecht. The lhcb trigger system. *Nuclear Physics B - Proceedings Supplements*, 187:237–244, 2009. ISSN 0920-5632. doi: https://doi.org/10.1016/j.nuclphysbps.2009.01.033. URL `https://www.sciencedirect.com/science/article/pii/S0920563209000395`. Proceedings of the 8th International Conference on Beauty, Charm and Hyperons in Hadronic Interactions.

[137] Wouter D. Hulsbergen. Decay chain fitting with a Kalman filter. *Nucl. Instrum. Meth. A*, 552:566–575, 2005. doi: 10.1016/j.nima.2005.06.078.

[138] Muriel Pivk and Francois R. Le Diberder. SPlot: A Statistical tool to unfold data distributions. *Nucl. Instrum. Meth. A*, 555:356–369, 2005. doi: 10.1016/j.nima.2005.08.106.

[139] Tianqi Chen and Carlos Guestrin. Xgboost: A scalable tree boosting system. In *Proceedings of the 22nd ACM SIGKDD International Conference on Knowledge Discovery and Data Mining*, KDD '16, page 785–794, New York, NY, USA, 2016. Association for Computing Machinery. ISBN 9781450342322. doi: 10.1145/2939672.2939785. URL `https://doi.org/10.1145/2939672.2939785`.

[140] Giovanni Punzi. Sensitivity of searches for new signals and its optimization. *eConf*, C030908:MODT002, 2003.

[141] Giovanni Punzi. Sensitivity optimization of multichannel searches for new signals, 2020. URL `https://arxiv.org/abs/2011.11770`.

[142] Recommendations for the Modeling of Smooth Backgrounds. Technical report, CERN, 2020. URL `https://cds.cern.ch/record/2743717`.

[143] V. V. Gligorov. Reconstruction of the channel $B_d^0 \to D^+pi^-$ and background classification at LHCb. 4 2007.

[144] Roel Aaij et al. Measurement of the $B_s^0 \to \phi\phi$ branching fraction and search for the decay $B^0 \to \phi\phi$. *JHEP*, 10:053, 2015. doi: 10.1007/JHEP10(2015)053.

[145] S. S. Wilks. The Large-Sample Distribution of the Likelihood Ratio for Testing Composite Hypotheses. *Annals Math. Statist.*, 9(1):60–62, 1938. doi: 10.1214/aoms/1177732360.

[146] Framework TDR for the LHCb Upgrade II: Opportunities in flavour physics, and beyond, in the HL-LHC era. 2021.

[147] Framework TDR for the LHCb Upgrade II: Opportunities in flavour physics, and beyond, in the HL-LHC era. Technical report, CERN, Geneva, 2021. URL `https://cds.cern.ch/record/2776420`.

[148] Roel Aaij et al. Physics case for an LHCb Upgrade II - Opportunities in flavour physics, and beyond, in the HL-LHC era. 8 2018.

[149] Pierre Billoir. Kalman filter and byproducts using the weight matrix formalism. unpublished, 2015. URL `https://indico.cern.ch/event/337568/contributions/1733018/attachments/1189146/1725559/Billoir_WeightFormalism.pdf`.

[150] Renato Quagliani. Parametric studies of u2 performance. unpublished, 2023. URL `https://indico.cern.ch/event/1338643/contributions/5687146/attachments/2761447/4808964/Upgrade2_weightmatrix_Presentation.pdf`.

[151] Ivan Peric. A novel monolithic pixelated particle detector implemented in high-voltage CMOS technology. *Nucl. Instrum. Meth. A*, 582:876–885, 2007. doi: 10.1016/j.nima.2007.07.115.

[152] Wouter Verkerke and David P. Kirkby. The RooFit toolkit for data modeling. *eConf*, C0303241:MOLT007, 2003.

[153] Kyle S. Cranmer. Kernel estimation in high-energy physics. *Comput. Phys. Commun.*, 136:198–207, 2001. doi: 10.1016/S0010-4655(00)00243-5.

[154] Roel Aaij et al. Measurement of the $B_s^0 \to \mu^+\mu^-$ decay properties and search for the $B^0 \to \mu^+\mu^-$ and $B_s^0 \to \mu^+\mu^-\gamma$ decays. *Phys. Rev. D*, 105(1):012010, 2022. doi: 10.1103/PhysRevD.105.012010.